上海交通大學

SHANGHAI JIAO TONG UNIVERSITY

学士学位论文

BACHELOR’S THESIS

论文题目： 形状记忆陶瓷纳米颗粒增强铝基复合材料的力学行为

学生姓名: 郑王树
学生学号: 516051910085
专　　业: 材料科学与工程-徐祖耀班
指导教师: 郭强、Zehui Du
学院（系): 材料科学与工程

上海交通大学
毕业设计（论文）学术诚信声明

本人郑重声明：所呈交的毕业设计（论文），是本人在导师的指导下，独立进行研究工作所取得的成果。除文中已经注明引用的内容外，本论文不包含任何其他个人或集体已经发表或撰写过的作品成果。对本文的研究做出重要贡献的个人和集体，均已在文中以明确方式标明。本人完全意识到本声明的法律结果由本人承担。

作者签名：郑玉树

日期：2020 年 06 月 09 日

上海交通大学

毕业设计（论文）版权使用授权书

本毕业设计（论文）作者同意学校保留并向国家有关部门或机构送交论文的复印件和电子版，允许论文被查阅和借阅。本人授权上海交通大学可以将本毕业设计（论文）的全部或部分内容编入有关数据库进行检索，可以采用影印、缩印或扫描等复制手段保存和汇编本毕业设计（论文）。

保密 √，在 2 年解密后适用本授权书。

本论文属于

不保密□。

（请在以上方框内打“√”）

作者签名：郑玉树　　　　　　　　指导教师签名：

日期：2020 年 06 月 09 日　　　　　　日期：2020 年 06 月 09 日

形状记忆陶瓷纳米颗粒增强铝基复合材料的力学行为

摘要

在温度场和力场作用下，氧化锆基陶瓷能够发生可逆的马氏体相变，进而引起显著的形状记忆效应。研究发现，通过元素掺杂可以调控氧化锆陶瓷的相变温度，而氧化锆基陶瓷的力学行为则决定于其显微组织特征：具有多晶结构的氧化锆基陶瓷在承载时发生晶间断裂从而显示出宏观脆性，丧失了相变能力；而单晶/寡晶氧化锆基陶瓷虽然具有形状记忆效应，但由于制备工艺的限制，仅能够以微纳尺度的粉体形态存在。因此，如何在保持形状记忆效应的前提下，制备出氧化锆基或其复合材料的块体样品是这类材料发展的瓶颈难题。

在本研究中，通过粉末冶金工艺，我们制备了 12mol％铈掺杂的单晶氧化锆纳米颗粒增强铝基复合材料（CZ-Al），其中颗粒增强体的质量分数为 30 wt%。通过对复合组织的电子显微学表征发现，机械球磨和后续高温致密化工艺使得 Al 基体形成层状超细晶组织，CZ 纳米颗粒优先分布于 Al 基体的层间界面上。阿基米德排水法测得 CZ-Al 复合材料的密度为 3.2 g/cm^3，致密度达到 100%。宏观力学性能测试显示，复合材料的维氏硬度为 85.1±0.2，比相同工艺制备的纯 Al 高约 67.2％，压缩屈服强度为 188.4±8.1 MPa，比相应纯 Al 提高约 486.0％。复合材料和纯 Al 的压缩断裂应变都在 20%左右，无明显差别，但拉伸断裂应变相比纯铝提升 150%。结合断裂截面分析，初步表明 CZ 纳米颗粒对层状结构复合材料的增强效应明显。

在常温和粉体状态下，12mol％铈掺杂的单晶氧化锆纳米颗粒的稳定结构为单斜相，而高于奥氏体结束温度 336℃，其稳定结构是四方相。X 射线衍射实验显示，在制备态的 CZ-Al 复合材料中纳米颗粒四方相占比 100%，说明从高温致密化制备的冷却过程中，Al 基体的存在约束了氧化锆纳米颗粒向单斜相的相变。由于氧化锆的马氏体相变伴随着约 4-5%的体积变化与 14-15%的剪切应变，上述结果说明在复合材料的纳米增强体颗粒周围必然存在大量几何必需位错及残余应力（应变），使得近界面微区的 Al 基体发生明显的应变硬化。因此，复合材料相比纯 Al 的强度和硬度提升可能来自纳米颗粒的承载和 Al 基体的应变硬化共同作用的结果。

对~2 μm 直径的 CZ-Al 微柱研究表明，压缩屈服强度达到约 521.2 MPa，比同一方法制备的纯 Al 微柱提升 710%。透射电子显微镜对压缩后的 2μm 直径复合微柱纵截面的结果显示，CZ 颗粒中大多数氧化锆从四方相转变为单斜相，在基体和 CZ 颗粒界面处存在大量几何必须位错，远离界面处位错密度降低，证明了 CZ 纳米颗粒对复合材料的强化机理。

本研究制备了氧化锆陶瓷颗粒增强 Al 基复合材料并初步表征了其显微组织结构和力学行为。研究结果显示，复合材料相比相同工艺制备的纯 Al 基体有明显的增强效果。进一步的工作将聚焦于制备工艺的优化，以及对复合材料界面性能和变形机理的研究和阐释。

关键词：形状记忆效应，马氏体相变，金属基复合材料，原位压缩，尺寸效应

Development and Mechanical Behavior of Aluminum Matrix Composite Reinforced by Shape Memory Ceramics

ABSTRACT

Zirconia-based ceramics can undergo a reversible martensite phase transformation under temperature or stress fields, which in turn causes a significant shape memory effect. It is reported that the phase transformation temperature of zirconia-based ceramics can be tailored by element doping, and the mechanical behavior of zirconia-based ceramics is determined by its microstructure characteristics: polycrystalline zirconia-based ceramics tend to suffer from intergranular fracture upon loading, as a result of their intrinsic brittleness at the macro-scale, which leads to their lack of capability for phase transformation. In comparison, single crystalline/oligocrystalline zirconia-based ceramics are capable of maintaining shape memory effect, while they can only be made into powder form because of the limitation in processing. Therefore, it is highly desired to fabricate bulk samples of zirconia-based ceramics or its composites while still maintain the shape memory effect.

In this study, we prepared 12mol% cerium-doped zirconia single crystalline nanoparticles reinforced aluminum matrix composite (CZ-Al) via a powder metallurgy approach, in which the mass fraction of the particle reinforcement was 30 wt%. Electron microscopy revealed that the mechanical ball milling and subsequent high temperature densification process generated a laminated ultrafine-grained microstructure in the Al matrix, and the CZ nanoparticles were preferentially distributed on the interlayer interface of the Al matrix. The density of the CZ-Al composite was 3.22 g/cm^3 using the Archimedes method, approaching a relatively density of almost 100%. The Vickers hardness of the composite was found to be 85.1±0.2, approximately 67.2% higher than that of pure Al prepared by the same process. The compressive yield strength is 188.4±8.1 MPa, 486.0% higher than that of pure Al. Compressive fracture strain of CZ-Al and pure Al were both around 20%, while the tensile fracture strain of CZ-Al was ~150% higher than that of pure Al. Therefore, these preliminary results showed considerable strengthening-toughening effect of the CZ-Al composite.

12mol% cerium-doped zirconia single crystal (CZ) is stable in monoclinic phase at room temperature and stable in tetragonal phase at the temperature higher than austenite finish temperature of 336°C. However, it was shown by X-ray diffraction that zirconia in the prepared CZ-Al composite is in 100% tetragonal phase at room temperature, suggesting that Al matrix had a constraint on the reverse martensite transformation upon cooling from the high temperature densification. Since the martensite transformation of zirconia is accompanied by a volume change of 4-5% and a shear strain of 14-15%, such an observation indicated that there must be a large number of geometrically necessary dislocations (GNDs) and residuals stress (strain) around the CZ nanoparticles, thus inducing obvious strain hardening of the Al matrix near the interface micro-region. Therefore, the enhancement in strength and hardness of the composite compared to pure Al may come from the combined effect of the load-sharing of the nanoparticles and the strain hardening of the Al matrix.

The preparation of CZ-Al micropillars with a diameter of ~ 2 μm further presented that compressive yield strength was 521.21MPa, 710% higher than that of pure Al pillar. Transmission electron microscopic (TEM) analysis on post-compression CZ-Al pillars revealed that zirconia phase in most of CZ particles were transformed from tetragonal phase into monoclinic phase. The presence of abundant GNDs near the particle/matrix interface, and the dislocation density generally decreased away from the interface, proved the strengthening mechanism of CZ nanoparticles proposed above.

In summary, zirconia ceramic particles reinforced Al-based composites were prepared and their microstructure and mechanical behavior were characterized. It is shown that the composite material had an obvious mechanical property enhancement effect compared with the pure Al matrix fabricated by the same process. Further work will focus on further optimization of the fabrication process, as well as further detailed interpretation of the interface properties and deformation mechanism of the composite.

Key words: Shape Memory Effect, Martensite Phase Transformation, Metal Matrix Composites, *in-situ* Compression, Size Effect.

Table of Contents

Table Captions

Figure Captions

Abbreviations

CZ	Cerium doped Zirconia
CZ-Al	Cerium doped Zirconia reinforced Aluminum Matrix Composites
EBSD	Electron Backscattered Diffraction
FESEM	Field Emission Scanning Electron Microscopy
FIB	Focus Ion Beam
MMC	Metal Matrix Composites
MTT	Martensitic Transformation Temperatures
SIMT	Stress-induced Martensitic Transformation
SMc	Shape Memory composites
SMC	Shape Memory Ceramics
SME	Shape Memory Effect
SMH	Shape Memory Hybrids
SMM	Shape Memory Materials
TEM	Transmission Electron Microscopy
XRD	X Ray Diffraction

Chapter 1 Introduction

Recently, shape memory materials (SMM) is highlighted owing to stimulus responsive behaviors as a sort of smart materials [1, 2]. There are mainly five groups of shape memory materials that have attracted great attention for research and application, including shape memory alloys (SMA) [3, 4], shape memory polymers (SMP) [5, 6], shape memory ceramics (SMC) [7], shape memory gel (SMG) [8], and newly involved shape memory hybrids (SMH) [9]. Among SMM, martensitic shape memory materials have been widely studied [10], which can go through reversible martensitic transformation between two different phases induced by temperature or load [11]. During the martensitic transformation, two extinctive phenomena occur, shape memory effect (SME) and superelasticity (SE) [12, 13], which play important roles in characterizing shape memory properties [14].

1.1 Hypothesis

With the overview of most case study of martensitic SMM, polycrystal serves as the major phase during reversible martensitic phase transformation and the bulk samples tend to be brittle and easily go through intergranular fracture [15, 16].

To solve the cracking problem, many works has been done from SMA to SMC. One unique idea came out that brittle SMA will enhance ductility when scaling down the size in microscale and nanoscale [17], such as Cu-Al-Ni alloy [18], NiTi-based alloy [19], Cu-based alloys [20], and single crystal Ti alloys [21]. Inspired from the case, some attempts were successfully done in SMC to suppressed fracture by constructing a micro-/nano- scale structure with less crystal grains, such as 8%CeO_2-0.5%Y_2O_3-ZrO_2 [22, 23], 2%Y_2O_3-5%TiO_2-ZrO_2 [24, 25], 16 mol% Ce-ZrO_2 [26].

Although the SME could be enhanced and fracture will be avoided by scaling down the size, the application will be limited below about 5 microns. To extend the sample size for application, Crystal *et al*. has fabricated mm-scale single crystal 1.5 and 2.0 mol% Y_2O_3-ZrO_2 [16].

In order to wisely design SMC at macroscale, it is reasonable to composite or incorporate other functional materials as a SMc, which may lead to some promising properties and behaviors as a bulk sample. Nowadays, shape memory composites (SMc) are gradually welcomed and designed, with SMA, SMG serving as the matrix or the reinforcement [9].

Whereas, there still remains large blanks on the phase transformation characteristics, interface structure, transformation hysteresis [9]. In the meantime, limited to the SMC study progress, no other SMC materials are applied in compositing metal matrix composites (MMC) up to date.

We herein propose that *single with the fabrication of Cerium doped Zirconia reinforced Aluminum Matrix Composites (CZ-Al), cerium doped zirconia (CZ) single crystal can be stabilized in tetragonal phase both at macroscale and microscale when compositing in Aluminum matrix composite.* To reasonably stimulate the stress at the grain boundaries and achieve small volume CZ-Al composites, composition modification was applied. In this case, single crystal CZ could further perform SME, whose brittle fracture can be suppressed with Al matrix, in application of self-healing [27], energy damping, actuator and sensing [13].

1.2 Objectives and Scope

This thesis aims at developing a sort of SMc with fine scale CZ-Al to achieve significantly enhanced mechanical properties and unveil the reinforcement mechanism of single crystal CZ nanoparticles. To begin with, we summarized the controlled factor for SME in terms of energy. Then, the objective can be fulfilled by proving the hypothesis that compositing in Aluminum matrix composite has constraint effect on single crystal CZ nanoparticles. Such a hypothesis lays a reasonable foundation on the CZ-Al fabrication. With suitable composition modified, small volume SMc with good mechanical properties are obtained. By studying the interface structure of CZ and Al, we dedicate to explore the reinforcement mechanism of CZ single crystal nanoparticles for composites, understand the effect of thermal residual stress (induced by CTE mismatch between Al/CZ), applied compressive stress and martensitic transformation on the dislocation development in Al and CZ and correlate the dislocation growth with the mechanical properties of the MMC.

1.3 Dissertation Overview

The thesis addresses:

Chapter 1 states the background of SMM, and challenges remaining solved. The hypothesis, objectives and scope have been proposed.

Chapter 2 reviews the literature concerned with SMM, with the main point of SMC and SMc. The basic theory of shape memory effect and its underlining mechanism of martensitic transformation are discussed. Controlling factors for SME and thermodynamic analysis of martensitic transformation are concluded.

Chapter 3 illustrates the experimental methods for the development and fabrication characterization of small volume SMc. In detail, it concerns with the systematic fabrication of CZ-Al, in accompany of the characterization on the fabrication process. A basic and promising techniques to fabricate small volume CZ-Al will also be elaborated.

Chapter 4 provides a systematic characterization method of CZ-Al based on morphology, phase composition and mechanical properties, with the purpose of studying size effect and matrix constraint. The reinforcement mechanism of CZ single crystals on the Al matrix was raised.

Chapter 5 makes conclusion on the thesis with the foundation of hypothesis to be proven. It contains the basic horizon of CZ-Al fabrication and characterization methodology. Future work and improvement of experimental design are list.

1.4 Findings and Outcomes

The research has contributed to some promising outcomes by:

1. Summarizing the controlling factors of shape memory effect in terms of system energy, including internal factors (dopant effect, matrix constraint, size effect, cofactor condition) and external factors (test temperature and load);
2. Establishing a promising methodology for the fabrication and characterization of small volume shape memory zirconia reinforced composites at micro/nanoscale;
3. Improving mechanical properties in the MMC with CZ addition;
4. Revealing the reinforcement mechanism of the shape memory ceramic nanoparticles in the composite.

Chapter 2 Literature Review

This chapter has a basic review on the shape memory materials (SMM), especially emphasizing on shape memory ceramics (SMC) and shape memory composites (SMc). The basic theory of shape memory effect (SME) and its underlining mechanism of martensitic transformation are discussed. Controlling factors for SME are concluded, including internal factors (dopant effect, matrix constraint, size effect, cofactor condition) and external factors (test temperature and load). According to the controlling factors, thermodynamic analysis of martensitic transformation is summarized.

2.1 Overview of Shape Memory Materials

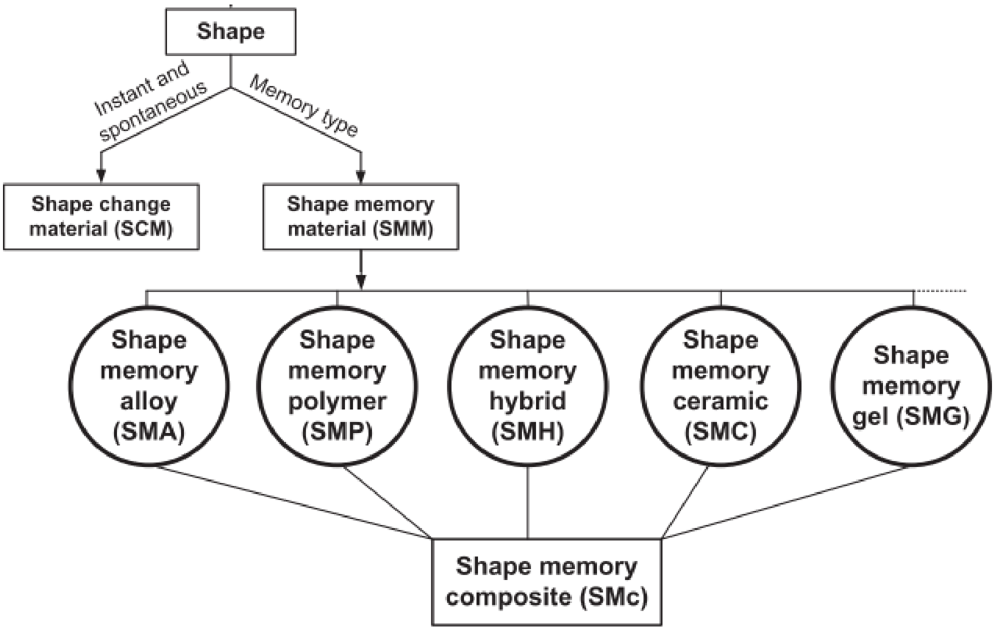

Figure 2. 1 The systematic classification of SMM [1].

SMM are featured by a kind of materials possessed with SME under the ambient stimulus (i.e. heat, stress, etc.). There are mainly five groups of shape memory materials that have attracted great attention for research and application (shown in **Figure 2. 1**), including SMA [3, 4], SMP [5, 6], SMC [7], SMG [8], and recently involved SMH [9]. SMc has been developed with one phase from SMM aforementioned [28]. That makes SMc not an independent subgroup of SMM technically [1]. SMH and SMc are easily confused, which both are made of different phase, while the phase made of SMH has to be without SME before hybridizing.

Various SMM have a common point, which lies in the SME. Concerned with SME, there are several domain mechanisms in SMM (shown in **Table 2. 1**), i.e. reversible phase transformation for SMA and SMC [29], dual-segment/domain system for SMP, SMG and SMH [30]. It is more complicated on SMc, depended on the major SMM in the composites, or the collective effect from matrix and reinforcement which has no SME individually [31].

Table 2. 1 The mechanisms for SME among different SMM and SMc [29-31].

SMM	**Domain Mechanism for SME**
SMA	Reversible phase transformation
SMC	
SMP	Dual-segment/domain system
SMG	
SMH	
SMc	Dominated by the major SMM

With multiple mechanism, an increasing demand has been developed to design a SMM in application of electro-mechanical systems [32]. Before the case, basic knowledge about the pros and cons of SMM should be clarified (**Table 2. 2**). Although the new materials have come out frequently, making the boundaries among different

SMM unpredictable, a general trend could still provide enough information before material design.

Table 2. 2 The pros and cons of different SMM.

SMM	Advantages	Disadvantages	Ref.
SMA	Multi-SME, lightweight, high reliability, thermal cycling ability	Low elastic deformation, high cost, narrow operated temperature window	[12]
SMC	High strength, wide operating temperature, chemical inertness	Low shape recovery, easily cracking, large unrecoverable deformation	[22]
SMP	High elastic deformation, low density, low cost, potential bio-function	Low mechanical behaviors, long response time, only one-way SME	[5, 6]
SMG	Soft material, ambient stimuli	Hard to design and reshape	[8]
SMH	Easily to design the structure	Low performance	[1, 31]

Several stimuli could trigger the reversible phase transformation in SMA and SMC, i.e. martensitic, viscoelastic, ferroelectric or ferromagnetic [9], where martensitic phase transformation is widely applied with solid background and arouses our interests. In the following discussion, structure-property relationship of martensitic phase transformation is mainly concluded.

2.2 Martensite Transformation induced Shape Memory Effect

Martensite transformation is diffusionless, which could be originated from Homer's Odyssey (Homer, 900BC) with the first application of transformation induced plasticity (TRIP) steel [33]. To widely broaden the case, martensite transformation has been applied in steel-like structure, where SME is considered as a novel mechanism in the martensite transformation [2].

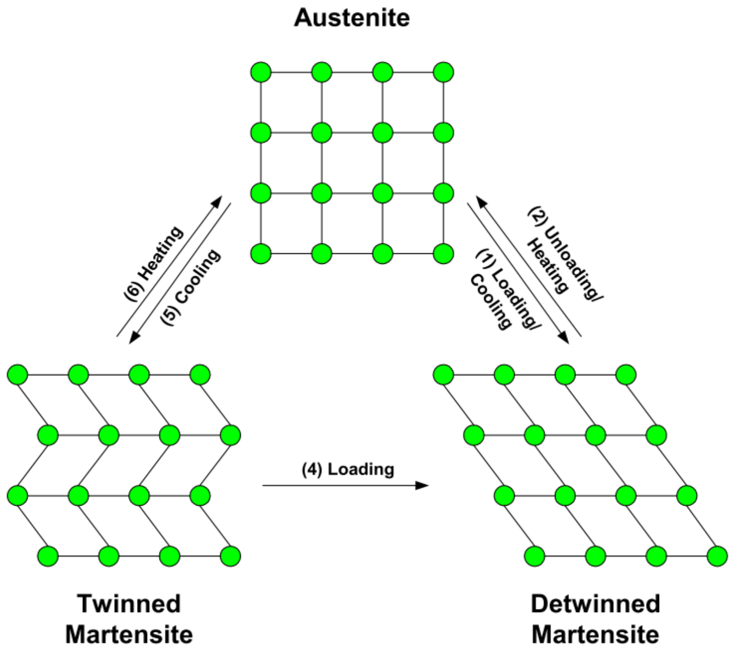

Figure 2. 2 The schematic illustration of crystal structural change during martensite transformation [1].

Four martensite transformation temperatures (MTT) are widely used to identify the state of process, M_s, M_f, A_s and A_f, which represented martensite/austenite and start/finish temperature, respectively [1]. During the martensite transformation (cooling process), it goes through M_s to M_f ; during reverse martensite transformation (heating process), it goes through A_s and A_f, which are usually measured by Thermomechanical analyzer (TMA).

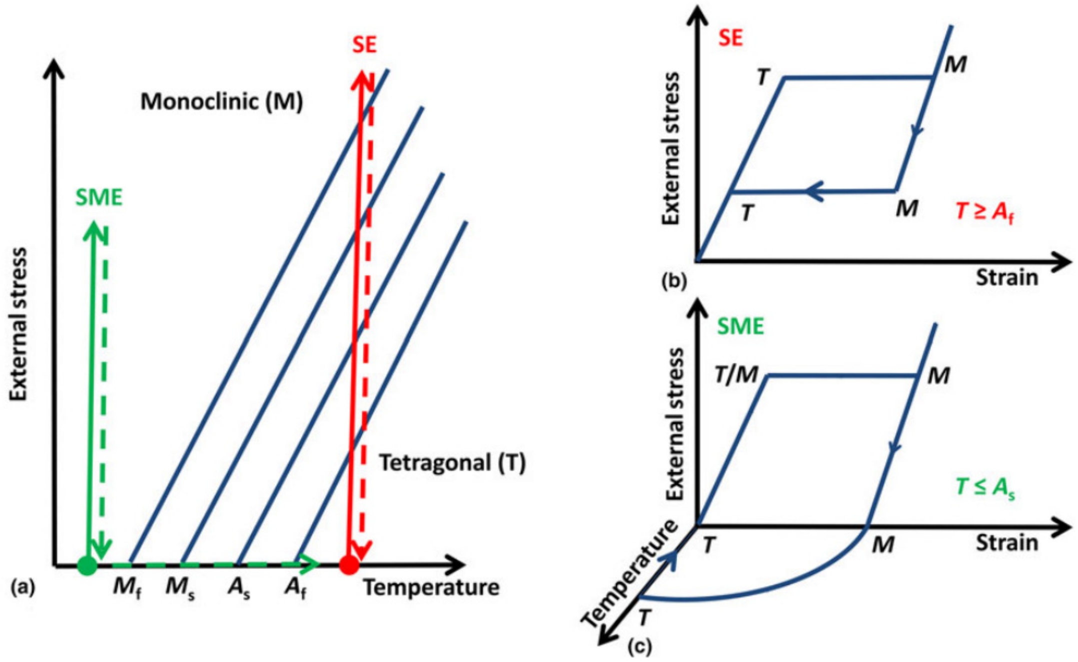

Figure 2. 3 SME and SE related to monoclinic phase and tetragonal phase transition under factors of stress and temperature [13].

Normally, at the temperature higher than A_f, the Gibbs free energy of austenite phase is lower than martensite phase, thus making austenite phase more stable, whilst, martensite phase at low temperature. Meanwhile, both the stress and temperature could induce the transformation. When ambient temperature is higher than A_f where tetragonal phase is stable, superelasticity (SE) takes place when external stress triggers tetragonal phase to monoclinic phase, forming a clear plateau, and fully recover to tetragonal phase when unloading (**Figure 2. 3** (b)). However, under the condition that ambient temperature is lower than A_s, SME takes place. Similar to SE, martensite phase transformation occurs during loading, but cannot recover whole strain during unloading, which can fully recover at the elevated temperature.

2.3 Thermo-responsive Shape Memory Materials

2.3.1 Zirconia based Shape Memory Ceramics

Basically, SMC have the advantages of higher operating temperature, higher strength, chemical inertness and tunable operation temperatures (c.f. with metallic SMA) [22]. Among all of the ceramics, zirconia (ZrO_2)-based ceramics is found to be the representative SMC, which manifest notably enhanced SME and SE in small volumes with less crystal grain, i.e. oligocrystalline and single [13]. The former (SME) needs to be deformed and subsequently heated to prompt shape recovery. As to the latter (SE), it requires automatically recover shape after the martensite-induced stress is released. In particular, there are a series of promising properties for engineering applications, such as critical martensite transformation stresses at high level, large amount of ductility, accompanied with recoverable strains and adjustable operation temperatures window [22].

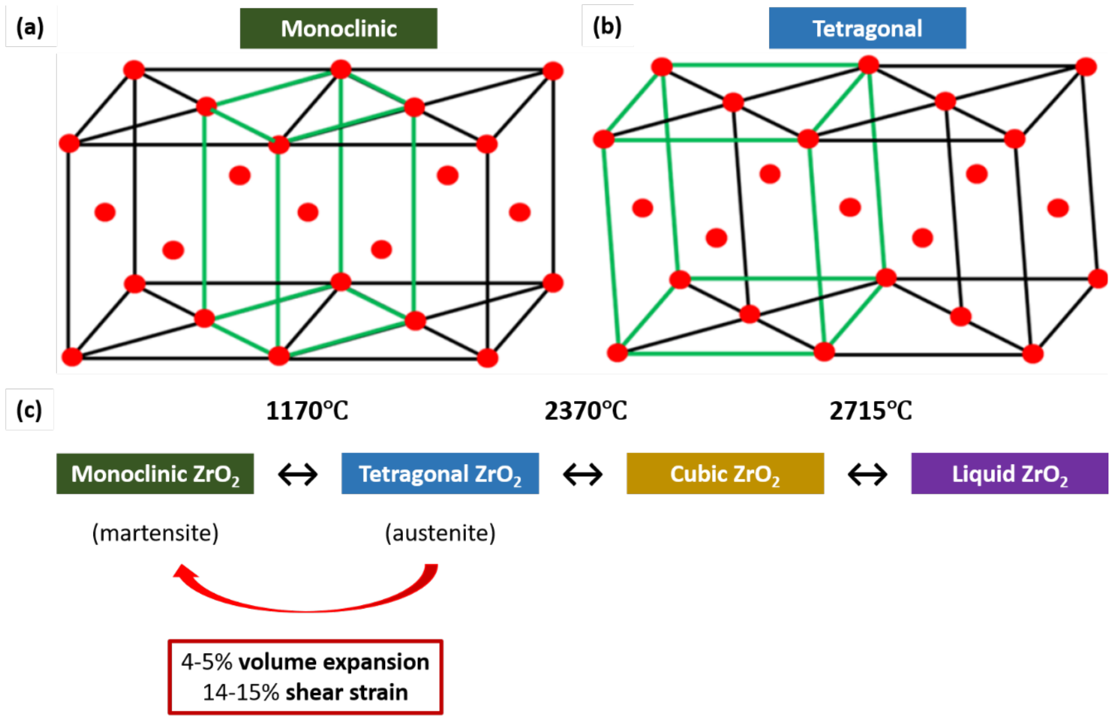

Figure 2. 4 Phase transformation in pure ZrO_2 between (a) monoclinic phase and (b) tetragonal phase [13]. (c) state in different temperature.

Normally, ZrO_2 has three common states, based on the Gibbs free energy, from high temperature to room temperature, monoclinic (m), tetragonal (t) and cubic (c) phases (**Figure 2. 4**), whose cracking problem associates with the reversible martensitic transformation. There are several stimuli which can trigger the transformation, i.e. applied stress, test temperature [34-37]. During the phase transformation, the crystal lattice change will cause a 4-5% volume expansion, which in the meantime, ~14-15% shear strain [38-40].

Swain *et al.* [7] was the first to discover SMCs and reported that a 9.4mol% Mg-TZP ceramic was capable of recovering 0.5% strain under 800 °C. Reyes-Morel *et al.* [41] subsequently reported the Ce-TZP could fulfill a relatively higher strain of ~1.5-2% under uniaxial compression, subsequently almost fully recovered by elevating the temperature to ~450 °C. Xu *et al.* [42] invented a new ternary system CeO_2-Y_2O_3-ZrO_2, with tunable dopant composition (Ce of 7.5~8.5mol% and Y of 0.45~0.55mol%) possessed with 95-100% recovery rate of strain 1.2%. Whilst, these systems will cause intergranular cracking and lead to low recoverable strain. Recently, Lai *et al.* [22] reported a 8mol%CeO_2–0.5mol%Y_2O_3–ZrO_2 system, which suppressed the failure by constructing a microscale structure with few crystal grains and the sample could withstand over 7% strains after 50 times cycles of loading and unloading (**Figure 2. 5**).

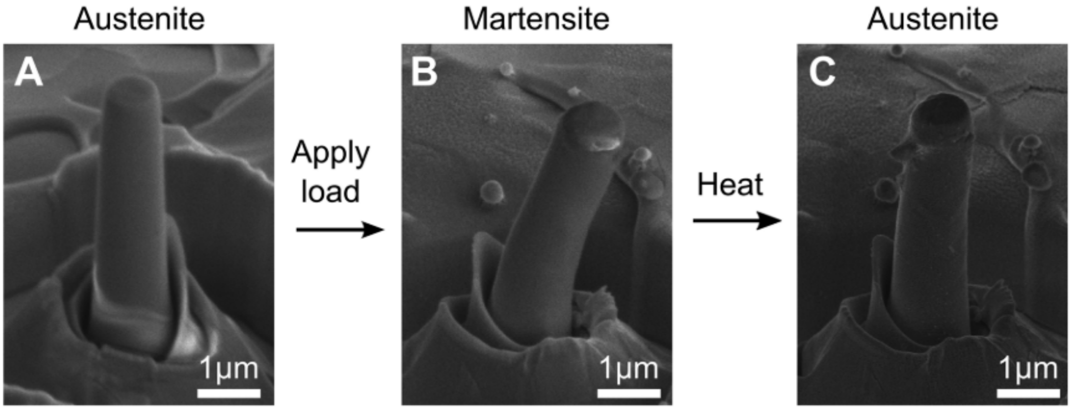

Figure 2. 5 Schematic illustration of the SME in 8mol%CeO_2–0.5mol% Y_2O_3–ZrO_2

pillars from (A) austenite, applying load to (B) martensite and (C) austenite after heating [22].

In spite that lots of efforts have made to avoid fracture in the brittle ceramics, there still remains a large improvement for structure condition, among which size effect is a significant effect to be considered. Michler *et al.* [43-45] proved that the fracture could be inhibited and plasticity can be enhanced with diameters decreasing to a threshold for dislocation shielding and twinning to occur, as well as eliminating interfaces and pores. Inspired from the case, Du *et al.* [23] explored the same system based on their previous work 8%CeO_2–0.5%Y_2O_3-ZrO_2, which can fully recover strain ~7% at 600 °C in a 0.7 μm-diameter pillar. Furthermore, Zeng et al. [25] refined the system and developed 2%Y_2O_3-5%TiO_2-ZrO_2, with ~7% recoverable strain in micron-sized zirconia at 400 °C. Superelasticity (SE) was obtained two years after Du *et al.* reported the system aforementioned. With oligocrystal or single crystal particles formation, fine and small grain size exhibit highly consistent SE, which could withstand over 100 cycles at 3.8% strain, and high dissipation energy [26].

After groundbreaking results in zirconia-based SMC, more works have stepped forwards, especially about the mechanism to improve the SME in SMC.

2.3.2 Shape Memory Composites

Shape memory composites (SMc) show numerous potentials in application, which are made of matrix and inclusions. It is welcomed owing to the flexibility in design and fabrication, with lots of promising properties or functions based on the controllable functional matrix and inclusions, most importantly, taken the advantage of SMH, in a do-it-yourself (DIY) manner [1]. The possible components of SMc could be modeled after SMH and presented in **Figure 2. 6**. There are multiple choices for matrix and inclusions, and the form of inclusions could be randomly designed.

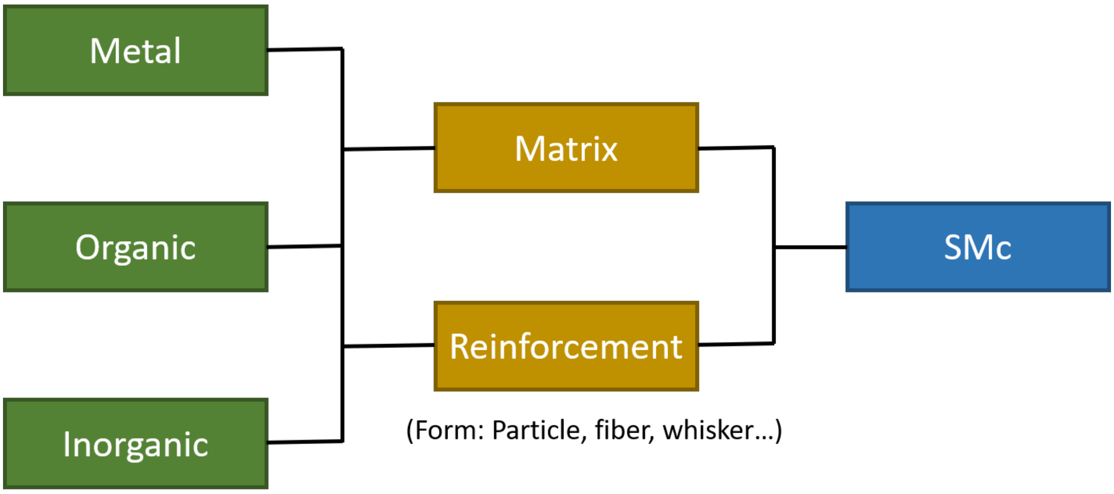

Figure 2. 6 Map of possible component for matrix and reinforcement in SMc.

Owing to the great progress on SMC during the five years [13, 16, 23-27, 46-49], the key point to expand the application area lies on diminishing fracture during martensite transformation in a reasonable manner.

Metal matrix composites (MMC) are consequently taken into consideration. Among MMC, aluminum matrix composites stand out by virtue of low density coupled with high stiffness, specific strength, specific modulus, especially for dispersion-reinforced aluminum matrix composites [50-52]. Furthermore, Al is natural for being an elastic matrix, which could absorb energy during SMC transformation.

Out of the trial to apply SME in SMc, Furuya *et al.* [53] have first designed Ti-Ni fibres reinforced aluminums matrix composites system to strengthen the MMC with residual stress caused by SME. In the same group, Yamada *et al.* [54] proposed that with Ti-Ni SMA particles added into Al matrix, the composites could be strengthened, owing to the SME during the fabrication, where the cooling procedure will induce residual thermal stress. Since the strengthening mechanism raised by Yamada' group is remarkable and could be further applied in other SMc system, the whole illustration is shown in **Figure 2. 7**.

(a) Sinter to disperse Ti-Ni particles into the matrix.

(b) Heat up the sample and then quenching to obtain shape memory effect.

(c) Preset a strain at martensite state to change the shape of Ti-Ni particle.

(d) Heat up above austenite starting temperature (As).

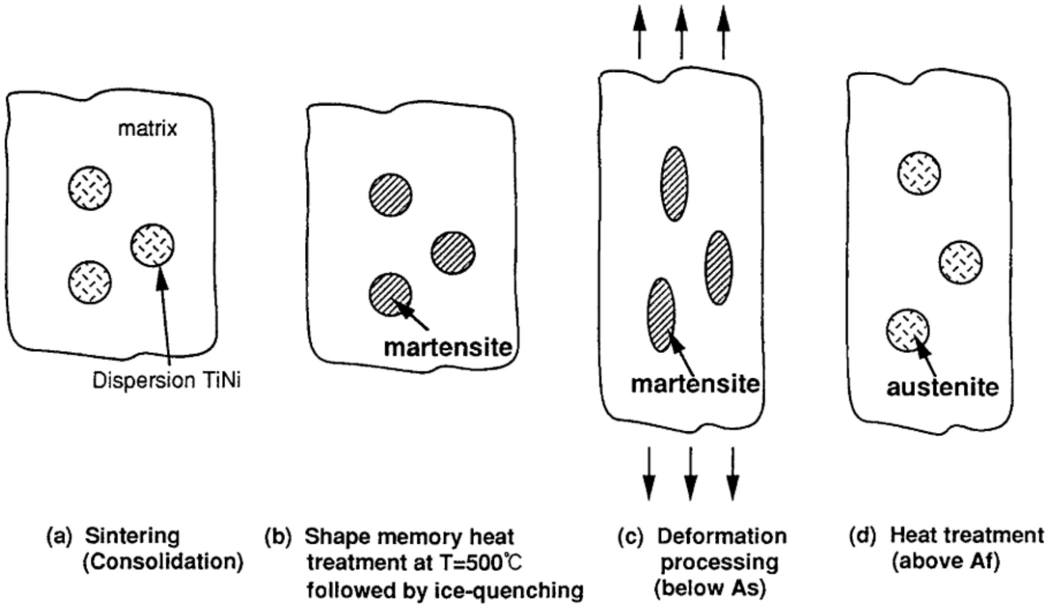

Figure 2. 7 Schematic illustration of strengthening mechanism in Ni-Ti SMA particle reinforced composites by SME [54].

In the meantime, a strengthening mechanism has been further conducted. Yang *et al.* [55] concluded from several cases since 2000, including SMA particulate/fiber/thin film-reinforced composites, and emphasized that higher CTE caused by the reinforcement and matrix during the fabrication will induce the residual thermal stress, thus contributing to the strength and toughness.

To systematically explore the SMc fabrication methodology, Mizuuchi *et al.* [56] prepared Ti-Pd-Ni-W SMA fibre titanium matrix composites via sheath-rolling. Wei *et al.* [9] reviewed a Ni-Ti SMA-Al sheet system via squeeze casting or powder metallurgical (P/M) route. Moreover, the advantages of P/M (i.e. low processing temperature and low cost [51]) have aroused great interest in academy and industry.

Porter *et al.* reported that Nitinol SMA reinforced Al composites were strengthened due to residual stresses [57].

With the purpose of fulfilling the SME in the SMc, based on previous work, Lai et al. [1] has raised an system with elastic matrix (i.e. silicone) and the transition inclusion (i.e. wax). The mechanism behind is similar to SMP, with elastic-transition segment/domain system (**Figure 2. 8**).

(a) The reinforcement is dispersed in the matrix in advance with proper fabrication methodology according to the materials (normally at high temperature).

(b) Composites are deformed with elastic energy stored in the matrix. Then decrease the temperature (or any stimulus which could induce state transformation), transition of reinforcement could in effect guard against the elastic energy of matrix relaxation.

(c) The composite will retain the deformed shape after the constraint is removed.

(d) Heat up and composite turns to be pristine state.

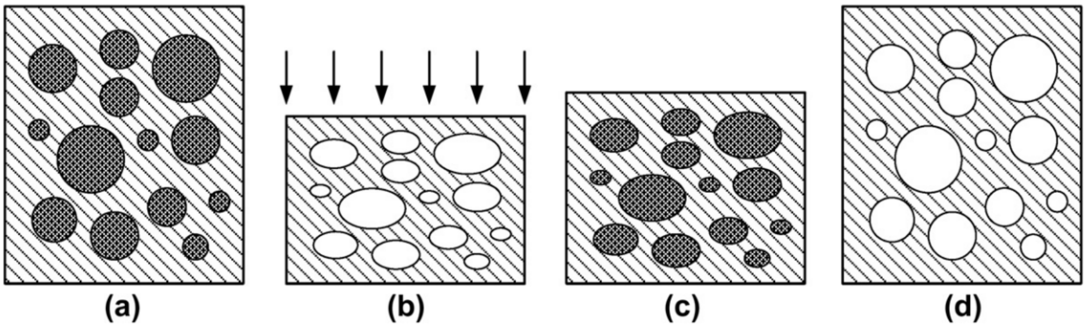

Figure 2. 8 Schematic illustration of one approach for SMc obtaining SME (black dot- reinforcement state one, white dot- reinforcement state two) [1].

Recently, Rauch *et al.* [49] created an interesting system to scale SMC for bulk-level energy dissipation, named after granular packing with ZrO_2-12 mol%CeO_2 and ZrO_2-15 mol%CeO_2 filling (shown in **Figure 2. 9**), found that the reversible stress-induced martensitic transformation (SIMT) happened. It offers us a good platform to reduce the particle size of SMC in a suitable matrix and explore the SIMT mechanism.

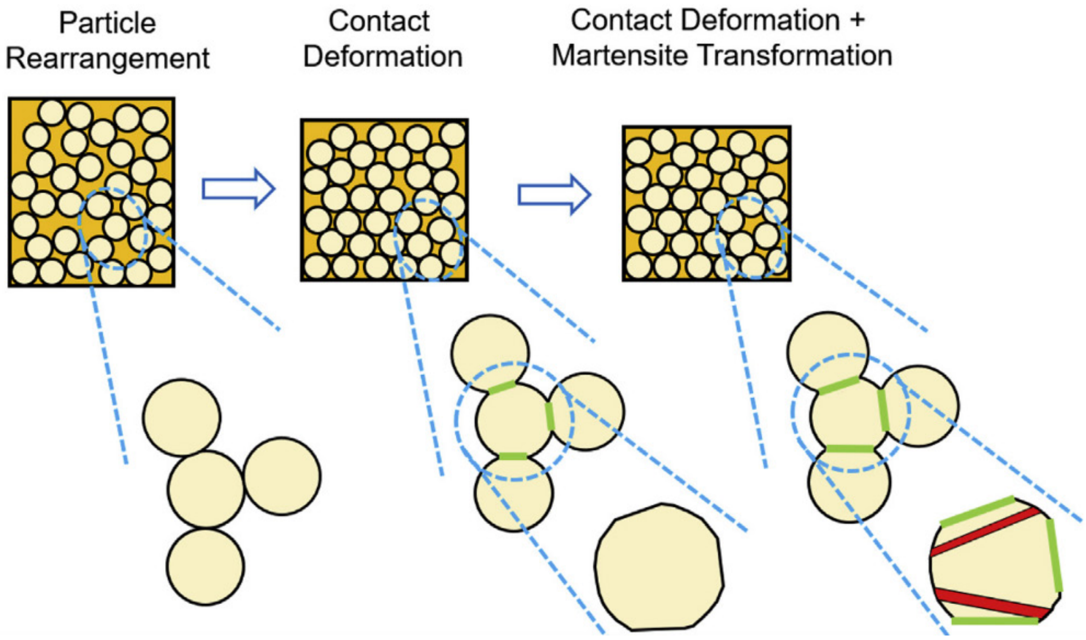

Figure 2. 9 Schematic image of co-evolution of granular packing with 12 mol% and 15 mol%CeO_2-ZrO_2 filling [49].

In spite that a SMA-MMC system has been widely studied, there still remains large open space in the research on revealing great potentials to exhibit unprecedented SME as well as superior mechanical properties. A promising system started from SMC single crystal [26], which possessed with highly reproducible superelasticity to over 100 cycles, will be slightly refined and combined with Al matrix. Size effect of the SMC particles in MMC is unclear. The function of metal matrix composites constraint on martensitic transformation of SMC particles and the resultant mechanical properties of the MMC remains questioned.

In application, it might have potentials to improve the strength and toughness of MMCs, be applied on stimulus-induced (temperature based on SME, stress based on SE or CTE mismatch) sensors, and energy damping equipment.

2.4 Controlling Factors for Martensitic Shape Memory Effect

Martensitic shape memory effect has various potentials, which could be featured during martensite transformation. Although SMc opens a DIY manner for research, it is a must for the researchers to better understand how to design a suitable system, which could have ability to obtain good SME as well as other functional structure.

As to SMA and SMC widely reported in the papers, basic approach to control the SME is to manipulate martensite transformation (and reverse one). Material dimension has strong effect on SME [17, 18, 58], while for a specific area, it is rare to change it. Apart from that, controlling factors could be divided into internal factors and external factors, which directly affect martensitic transformation and then have influence on martensitic SME (shown in **Table 2. 3**).

Table 2. 3 Controlling factors for Martensitic Shape Memory Effect.

Controlling Factors		**Demonstration**	**Ref.**
Internal	Dopant Effect	Some elements (i.e. Ca, Mg, Ce, Y etc.) change MTT	[7, 13, 35, 41, 47-49, 59-66]
	Matrix Constraint	Particles/Grain surrounded inhibit the strain stress	[13, 67]
	Size Effect	Surface to volume ratio	[13, 16, 22, 23, 25-27, 47, 66, 68]
	Cofactor Condition	Difference in crystal symmetry	[24, 47, 48, 69]
External	Temperature	Clausius-Clapeyron relationship	[70]
	Applied Stress		

Dopant effect has been studied since 1970s [59]. TZP and PSZ, and Zirconia-toughened alumina (ZTA) are three representative application of dopant to fully stabilize or partially stabilize high temperature phase zirconia (tetragonal or cubic) [15, 34, 62, 71]. The effect that dopant could decrease the MTT relies on the lattice distortion [72].

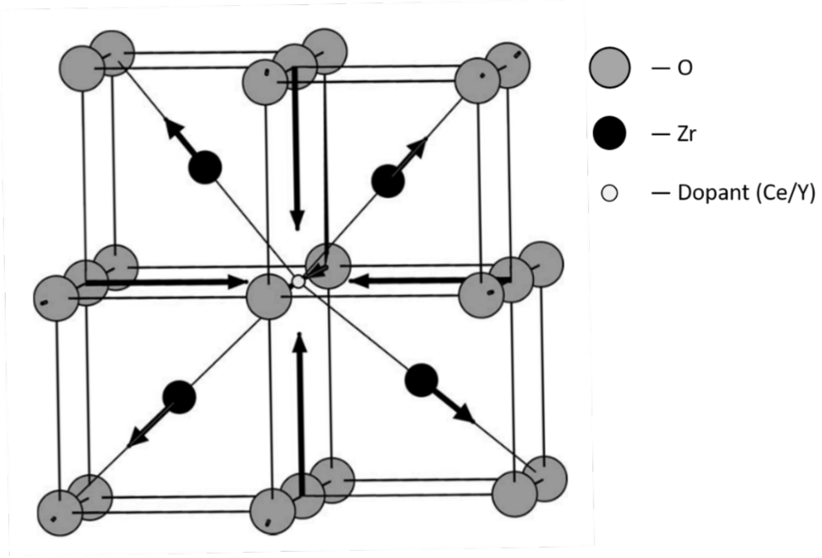

Figure 2. 10 Schematic illustration of dopant effect in a fluorite lattice, where dopant stays in the substitutional place [72].

Take zirconia for a case, yttria and cerium are popular for doping, and the lattice structure is shown in **Figure 2. 10**. Dopant element (Ce or Y) will replace one zirconia atom, resulting the distortion and relaxation of lattice. While yttria is found to be more effective than cerium to reduce MTT, mainly because the difference between ion radius of Y^{3+} (0.1019 nm) and Zr^{4+} (0.084 nm) is larger than Ce^{4+} (0.097 nm) with Zr^{4+}, and oxygen vacancy caused by yttria [73]. A series of dopant in different system has been tested (shown in **Figure 2. 11**), with DSC to document the MTT. The empirical equation could estimate the trend,

$$A_f = T_{undoped} - \alpha C_{dopant1} - \beta C_{dopant2} \qquad \text{Equation 1}$$

where $T_{undoped} = 1280.52℃$ is the martensite transformation temperature of pure zirconia, α, β, $C_{dopant1}$, $C_{dopant2}$ are the coefficient of dopant 1 and 2, mole ratio of dopant 1 and 2 respectively.

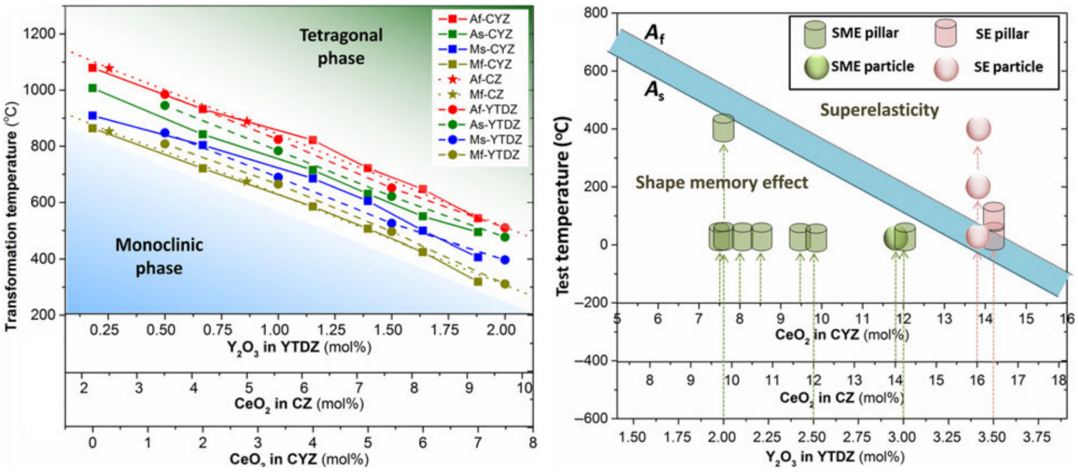

Figure 2. 11 Schematic illustration of dopant effect with cerium, yttria in CZ (cerium stabilized zirconia), CYZ (CeO_2-Y_2O_3-ZrO_2), and YTDZ (Y_2O_3-TiO_2-ZrO_2) [13].

In summary of previous work, matrix constraint is treated that the particles or grains surrounded induce a reverse stress or strain. Chawla *et al.* [67] reviewed that with metal matrix composites, both direct and indirect strengthening mechanism occur with stress passing through interface of two phase, as well as thermal mismatch induced by CTE. Tsoi *et al.* [74] reported that only the martensite with preferential orientation was affected by matrix constraint in NiTi-wire epoxy composites, while self-accommodate one can't. Whereas, there is still no systematic theory on matrix constraint, especially about the effect on SME. With energy term raised later, matrix constraint could possibly act the way same as dopant effect. In this project and in future, we will explore the matrix content with MTT relationship.

Size effect has been widely studied and mentioned in Section 2.3.1. The key point is to decrease the size, followed by improving the surface to volume ratio, and in case energy will change. In fact, Du *et al.* [23] applied the size effect on preparing single crystal or oligocrystal, with the purpose of releasing residual stress originated from grain boundary to obtain a higher ductility. The trick is shown in **Figure 2. 12**, which is worthy for further learning.

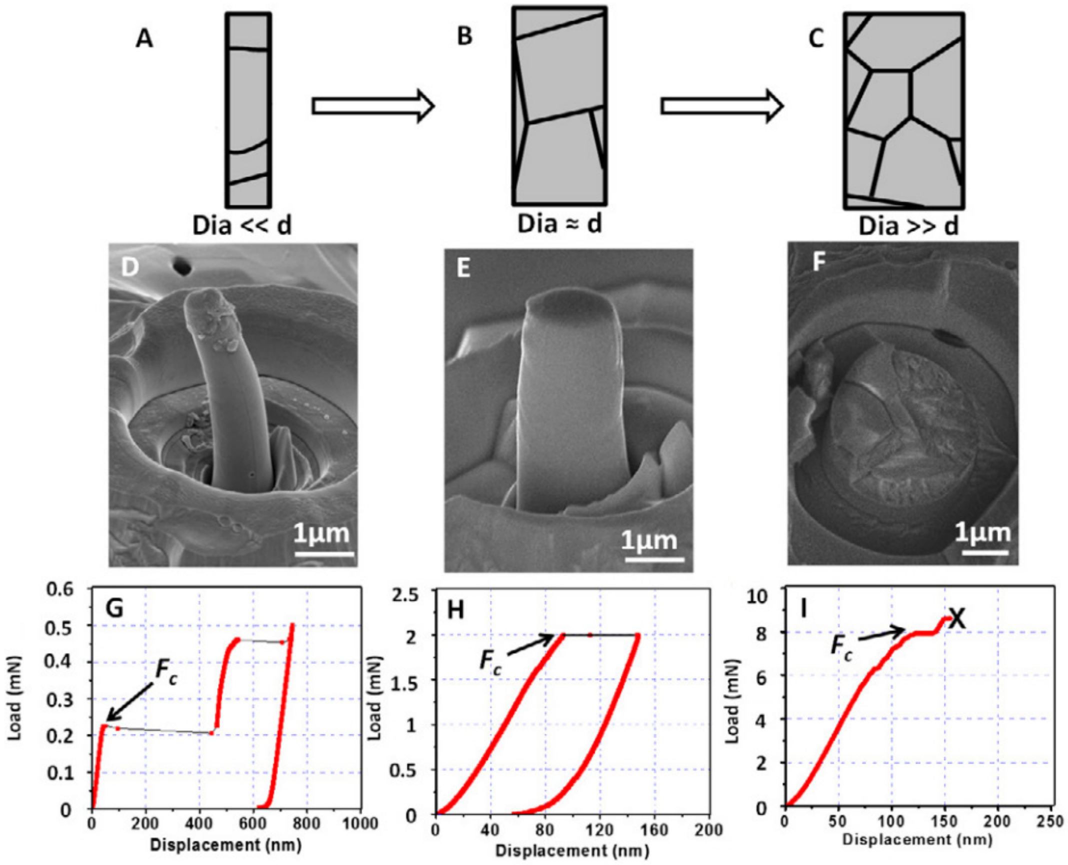

Figure 2. 12 Schematic illustration of size effect, taken 8mol%CeO_2–0.5mol%Y_2O_3-ZrO_2 as an example [23].

Essentially, cofactor condition means the strongest known conditions of compatibility [75], which indicated the possibility for existence of unstressed interfaces. Jetter *et al.* [47] reported a system $(Y_{0.5}Ta_{0.5}O_2)_{1-x}$-$(Zr_{0.5}Hf_{0.5}O_2)_x$ $(0.6 < x < 0.85)$, with tuning crystallographic compatibility in thermal hysteresis by a factor of 2.5, a high strain recovery was obtained. Pang *et al.* [48] found that cracking in polycrystalline CeO_2-ZrO_2 SMC could be inhibited in 13.5 mol% CeO_2-ZrO_2 system when meeting the cofactor conditions. When extending the meaning of cofactor condition, crystal orientation could be contained, with the common of crystalline orientation relationship. Crystal orientation has strong effect on the SME. where the competition between phase transformation and plastic deformation has been found to be orientation dependent [66], indicating the orientation dependence of activation energy of dislocation and nucleation. Therefore, optimization of the crystal orientation is of significance for utmost SME and suppressing cracking.

As to external factors (test temperature and applied stress), a well-known Clausius-Clapeyron equation is introduced, combining test temperature (T) and applied stress (σ) together [70]:

$$\frac{d\sigma}{dT} = -\frac{\Delta S}{\varepsilon} = -\frac{\Delta H}{T \cdot \varepsilon} \qquad \text{Equation 2}$$

where ΔS and ΔH are the entropy and enthalpy, ε is the strain during the transformation. Both are the key parameters to scale the SIMT behaviors, which will be frequently discussed in the following chapter.

Among all the controlling factors mentioned above, there is a Gibbs Free Energy equation, by which all the factor could be integrated together in energy term. Becher *et al.* [68] established a thermodynamic equation demonstrating the free energy change during martensite phase transformation $\Delta G_{t\to m}$:

$$\Delta G_{t\to m} = -\Delta G_c + \Delta U_e + \Delta U_s - \Delta U_{ex} \qquad \text{Equation 3}$$

where ΔG_c, ΔU_e, ΔU_s, ΔU_{ex} represent chemical free energy, strain energy, surface energy and applied energy from external term, respectively. In order to better calculate and estimate how one factor changed affects the transformation, a more concrete equation will be shown for different energy term in **Table 2. 4**, where $\Delta S^{t\to m}$ is entropy change per unit volume, T is the test temperature and T_0 is the equilibrium temperature of tetragonal phase, r is the effective diameter of zirconia grain, while γ_t and γ_m are surface tension of tetragonal phase and monoclinic phase, respectively. τ_{trans} is the stress required to occur transformation shear stress, and $\Delta\varepsilon$ is the transformation strain.

Table 2. 4 Energy term in thermodynamic analysis of martensitic SME [13, 68, 76, 77].

Energy Term	**Demonstration**	**Possible Factor**
ΔG_c	$\Delta G_c = \Delta S^{t\to m}(T_0 - T)$	Temperature
ΔU_e	Originates from the matrix constraint	Matrix constraint, Dopant effect, Cofactor condition
ΔU_s	$\Delta U_s = 4\pi r^2 \cdot (\gamma_t - \gamma_m)$	Size effect
ΔU_{ex}	$\Delta U_{ex} = \tau_{trans} \cdot \Delta\varepsilon$	Applied Stress Cofactor condition

Providing that martensite transformation occurs ($\Delta G_{t\to m} \leq 0$), it could be inferred that for each controlling factor, there is a critical stress. Only when the applied stress (or real stress on the zirconia for SMc) is higher than critical stress, can martensite phase transformation happen.

$$\tau_{trans} \geq \frac{-\Delta S^{t\to m}(T_0 - T) + 4\pi r^2 \cdot (\gamma_t - \gamma_m) + \Delta U_e}{\Delta\varepsilon} \qquad \text{Equation 4}$$

It has to be mentioned that for ΔU_{ex} term, it is highly dependent on cofactor condition, which in detail the crystal orientation has strong effect on stress distribution. Zeng *et al.* [24] reported martensitic transformation stress τ_{trans} is highly dependent on the crystallographic orientation, with a basic foundation of tensor properties (shown in **Figure 2. 13**). In the case, Schmid factor (SF) is adopted for better calculation (**Figure 2. 14**) [69]. **Equation 4** could be refined as:

$$\tau_{trans} \geq \frac{-\Delta S^{t\to m}(T_0 - T) + 4\pi r^2 \cdot (\gamma_t - \gamma_m) + \Delta U_e}{\Delta\varepsilon \cdot SF} \qquad \text{Equation 5}$$

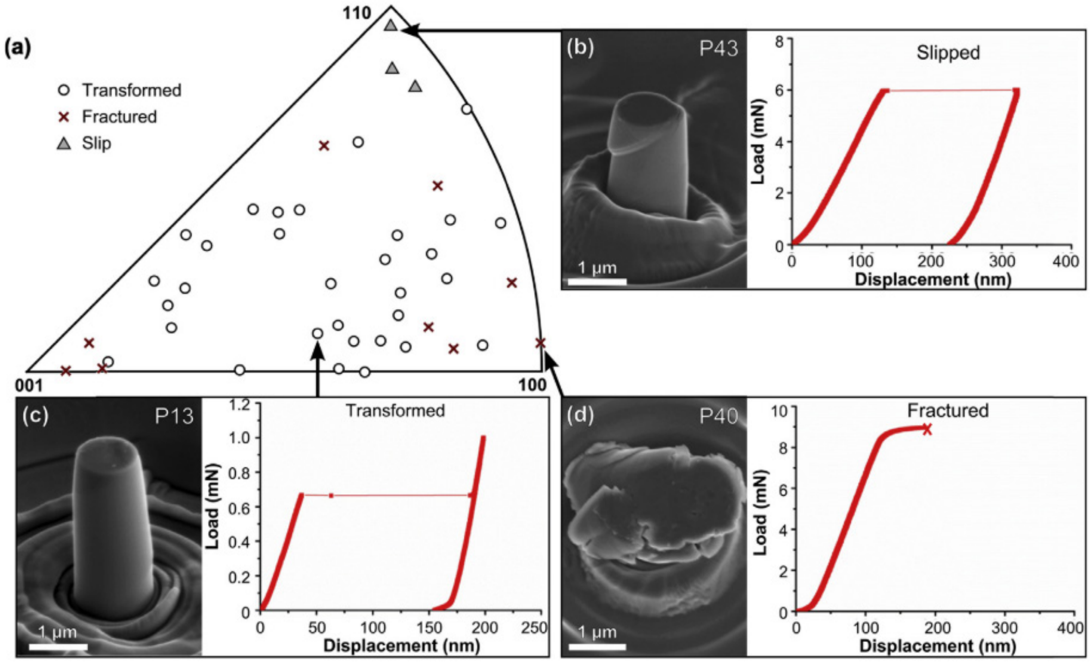

Figure 2. 13 Schematic illustration of (a) crystal orientation on stress-induced martensite transformation with different mechanical behaviors (b) slipped, (c) transformed and (d) fractured [24].

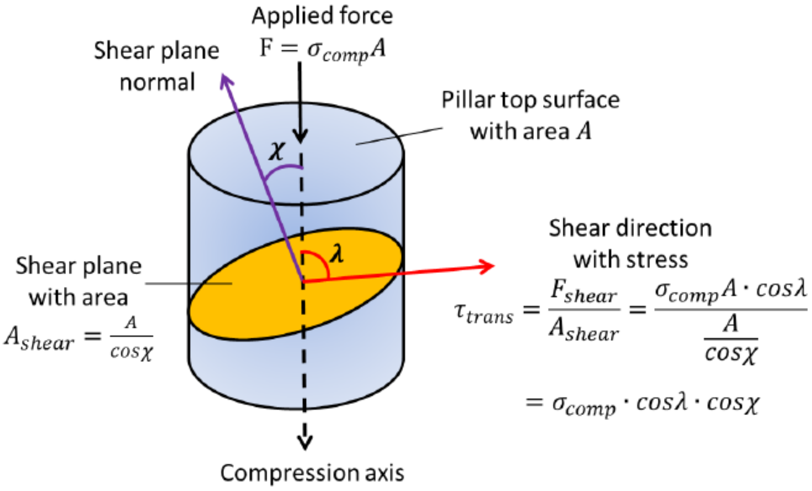

Figure 2. 14 Schematic illustration of Schmid factor (SF) [24].

2.5 Conclusive Remarks

This chapter reviews the literature related to SMM with different dimension, especially emphasizing on SMC and SMc. Previous work on design of SMc system has been widely summarized. The basic theory of shape memory effect (SME) and its underlining mechanism of martensitic transformation are discussed. Controlling factors for SME are concluded, including internal factors (dopant effect, matrix constraint, size effect, cofactor condition) and external factors (test temperature and load). According to the controlling factors, thermodynamic analysis of martensitic transformation is summarized. This chapter offers a long-term meaning for guiding the experimental design, and the result analysis based on theoretical calculation.

Chapter 3 Experimental Methodology

This chapter illustrates the experimental methods for the development and fabrication characterization of small volume shape memory composites (SMc). In detail, it concerns with the systematic fabrication of bulk cerium doped Zirconia reinforced Aluminum Matrix Composites (CZ-Al), in accompany of the characterization on the fabrication process. A basic and promising techniques to fabricate small volume CZ-Al will also be elaborated.

3.1 Rationale for Experimental Design

The experimental design is to fabricate shape memory composites (SMc), with the attempts in mechanical behaviors at small volume. Based on previous shape memory ceramics (SMC) procedure raised by Zeng *et al.* [25], a new experimental flow for SMc was provided in **Figure 3. 1**.

The steps are shown as follows:

1. Adopting single crystal cerium doped zirconia (CZ) as SMC particles reinforcements, pure Aluminum (Al) as metal matrix composites (MMC) with the evaluation and selection of materials;
2. Fabricating bulk CZ-Al with conventional composites processing techniques, followed by basic structural and mechanical characterization (will be discussed in Chapter 4).
3. Preparing small volume CZ-Al at microscale.
4. Conducting mechanical test at microscale and comparing with bulk sample based on shape memory effect (SME).
5. Optimizing the properties by materials and process modification.

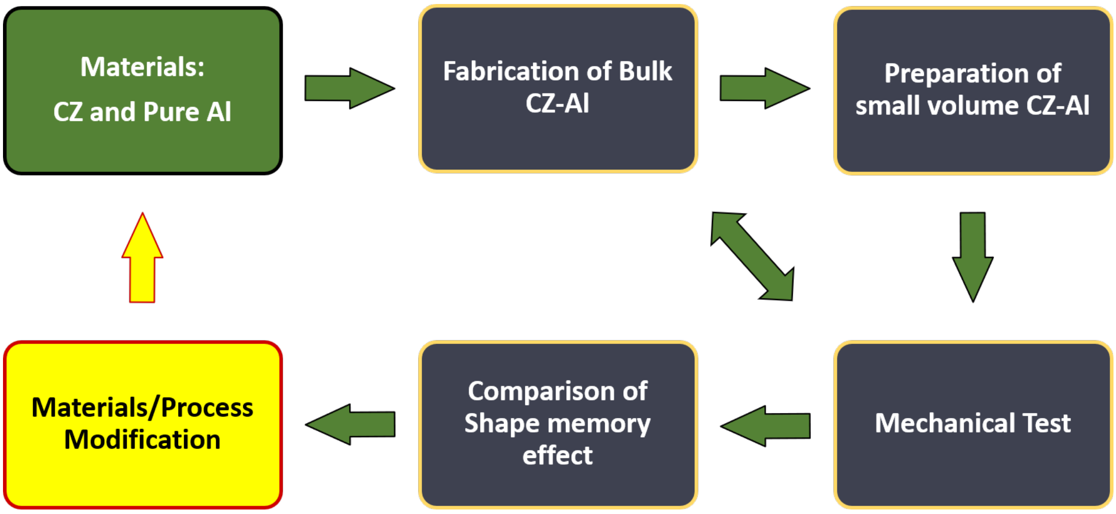

Figure 3. 1 The experimental work flow charts of studying fabrication method and properties of SMc.

From Chapter 2, dopant effect is a key factor to stimulate martensite transformation temperature (MTT) of zirconia, thus the type and content of dopant have tremendous effect on shape memory effect (SME). Apart from dopant effect, matrix constraint matters. To simplify the system and reveal the reinforcement mechanism, pure Al is selected in place of Al alloys, such as 6061 Aluminum alloy [52]. In future, Al alloys will be targeted and will be discussed in detail in Chapter 5.

3.2 Fabrication of Bulk CZ-Al

The bulk CZ-Al were fabricated with classic powder metallurgy (P/M) processing procedure [51] and co-sintering methods [78]. The pure aluminum powders (average size=10μm, as is shown in **Figure 3. 2** (a)) were purchased from Henan Yuanyang Powder Technology Co., Ltd., who is known for good quality of Al and Al-based powders. The stearic acid (SA) was purchased from Henan Tianfu Chemical Co.,Ltd., with function of inhibiting exorbitant welding as process control agent (PCA) [79, 80].

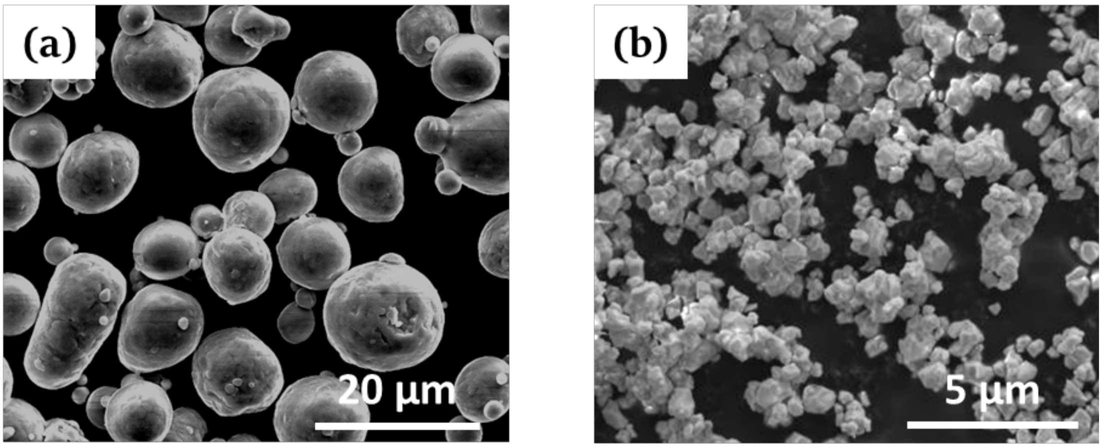

Figure 3. 2 FESEM images of (a) raw Al powders, (b) CZ single crystal.

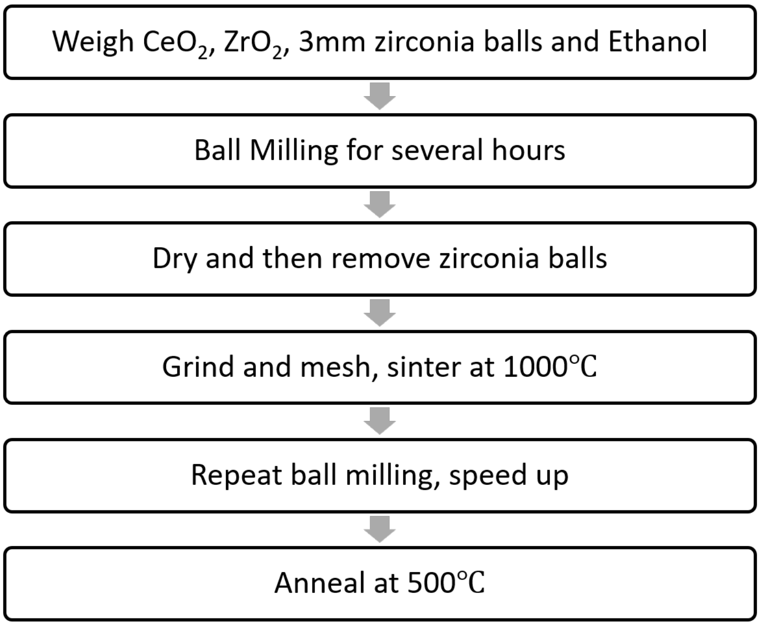

Figure 3. 3 Flow charts of the synthesis procedure for CZ single crystal (with permission of Dr. Zehui Du from NTU).

The synthesis of CZ single crystal particles (average size ~500nm, 5.85g/cm^3, as is shown in **Figure 3. 2** (b)) was provided by our collaborator Dr. Zehui Du from Nanyang Technological University (NTU). According to the dopant effect [22], cerium is superior to yttrium for the aspect of precise stimulation of MTT, the formula in molar ratio is established, x CeO_2 - (1-x) ZrO_2. From previous work, 12mol% of cerium is enough to fully stabilize zirconia tetragonal phase [13]. The fabrication methodology is concluded and shown in **Figure 3. 3** with permission. Based on co-sintering method, single crystal CZ powders are fabricated via ball milling and annealing several times. Annealing process contributes to the formation of single crystal, when martensite phase transformation takes place and induces the crystal mismatch among each single crystal. With the strain mismatch, bulk CZ tends to fall apart from one another, and single crystal forms. The image is presented in **Figure 3. 5** (d).

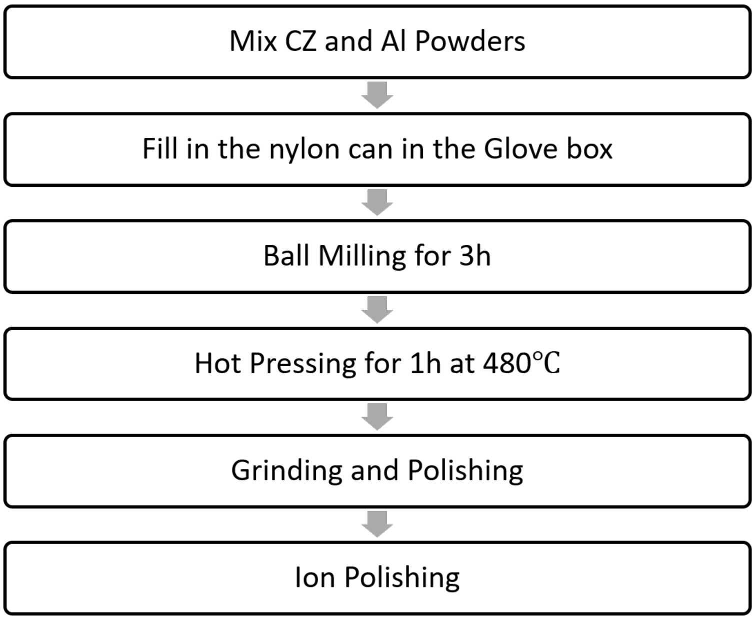

Figure 3. 4 Flow charts of the synthesis procedure for Bulk CZ-Al.

To prepare bulk CZ-Al, the precursors were weighted and mixed according to the weight ratio of x SA - y CZ - (1-x-y) Al. As a first attempt, 1wt% SA and 30wt% CZ were adopted. The complete procedure of bulk CZ-Al is shown in **Figure 3. 4**. Then, the precursors were mixed with zirconia milling balls (with three diameters of 6mm, 10mm and 20mm). The ball to powder weight ratio was set as 20:1, followed by filling in the nylon can (500ml, purchased from Nanjing NanDa Instrument Plant, **Figure 3. 5** (b)) and ball milling for 3h under argon gas atmosphere with 200 rpm speed in the Planetary ball mill (QM-3SP4, purchased from Nanjing NanDa Instrument Plant,

Figure 3. 5 (a)). After sieving out the zirconia balls, the mixture was transferred into the glove box and hot pressing for 1h at 480℃ via Electric tablet press (SDY-30, Keqi, Tianjin, **Figure 3. 5** (c)).

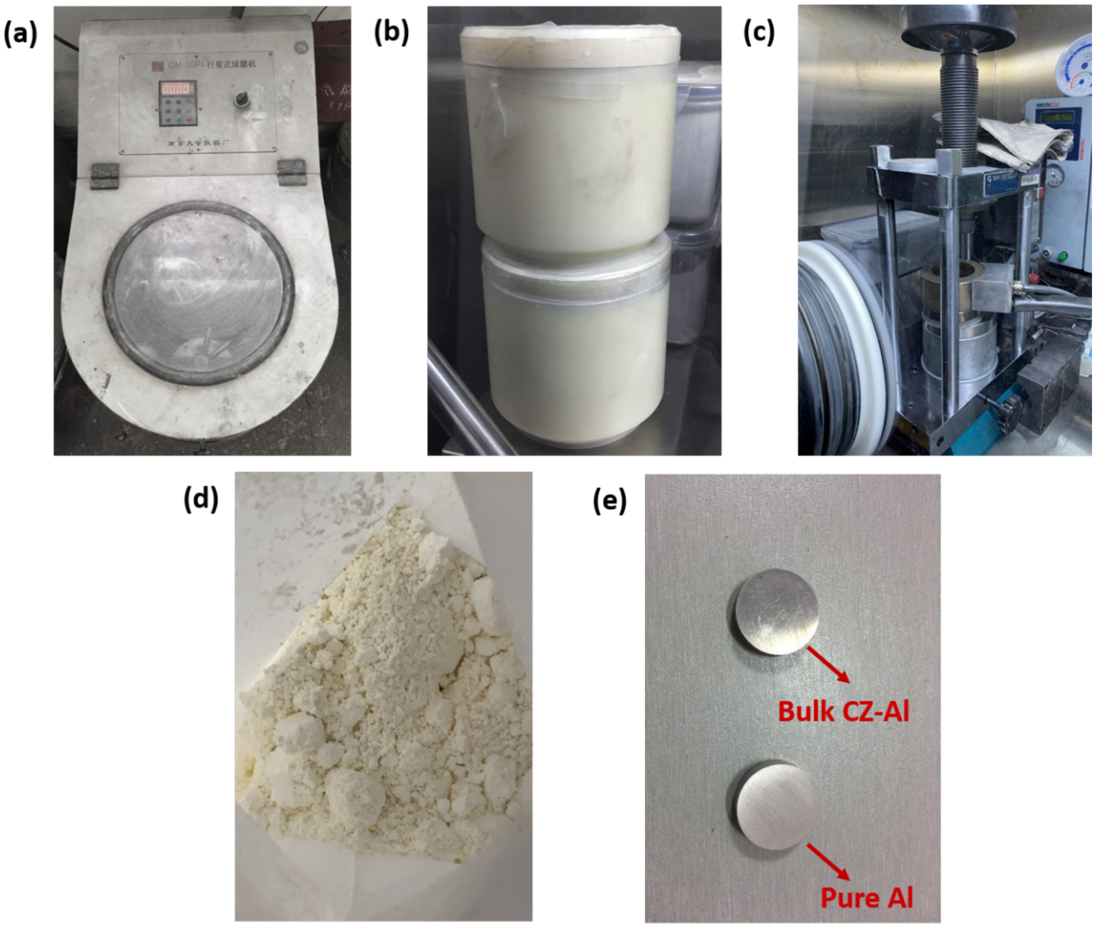

Figure 3. 5 Schematic diagrams of (a) Planetary ball mill, (b) Nylon tank (with zirconia ball), (c) Electric tablet press in the glove box. (d) 12mol% CZ powders, (e) CZ-Al (up) and pure Al (down).

Before characterization, grinding and polishing removed impurities, scratches and provided a good result. Controlling group was set to explore the effect of CZ single crystals, only in difference of the precursors, which consisted of stearic acid and Al at the weight ratio of 1:99. To better discriminate two sample, the precursors with ratio are shown in **Table 3. 1**.

Bulk CZ-Al and pure Al are shown in **Figure 3. 5** (e). The structural and thermo-mechanical characterization will be carried out in Chapter 4.

Table 3. 1 The precursors ratio of bulk sample, CZ, CZ-Al and Pure Al.

Bulk Sample	**Precursor** (Note: SA - stearic acid)
CZ	Ceria: Zirconia = 12: 88 (molar ratio)
CZ-Al	SA: CZ: Al = 1: 30: 69 (weight ratio)
Pure Al	SA: Al = 1:99 (weight ratio)

3.3 Characterization of Fabrication Process

Considering the significance of fabrication process, it is necessary to observe the whole procedure to confirm how the CZ and Al mix with each other. Ball milling and hot pressing are involved. Field emission scanning electron microscopy (FESEM, Scios DualBeam) test was applied. With the various detectors of second electrons (SE)，backscattered electrons (BSE), etc. morphology and component will be manifested via different contrast under high vacuum and electrical field. Different parameters were set to have a better vison on the sample, voltage, emission current, work distance and magnification.

3.3.1 Ball Milling Process

The morphology of CZ-Al or pure Al mixture was characterized each hour during ball milling process, and the results are shown in **Figure 3. 6**. As to pure Al, more Al were reshaped from spheres to flakes; surface remained smooth with ball milling processing, especially there was no obvious sphere in the field at 3h. As to CZ-Al, more CZ were embedded on Al flakes and unembedded CZ were reduced with ball milling processing, and over 90% CZ were on the Al flakes at 3h.

Combined with the parallel process, Al flakes remained approximately same size with or without CZ single crystal added. Meanwhile, CZ single crystal retained good shape during the process. To have a better structure during hot pressing, ball milling time for 3h is enough to disperse the powders.

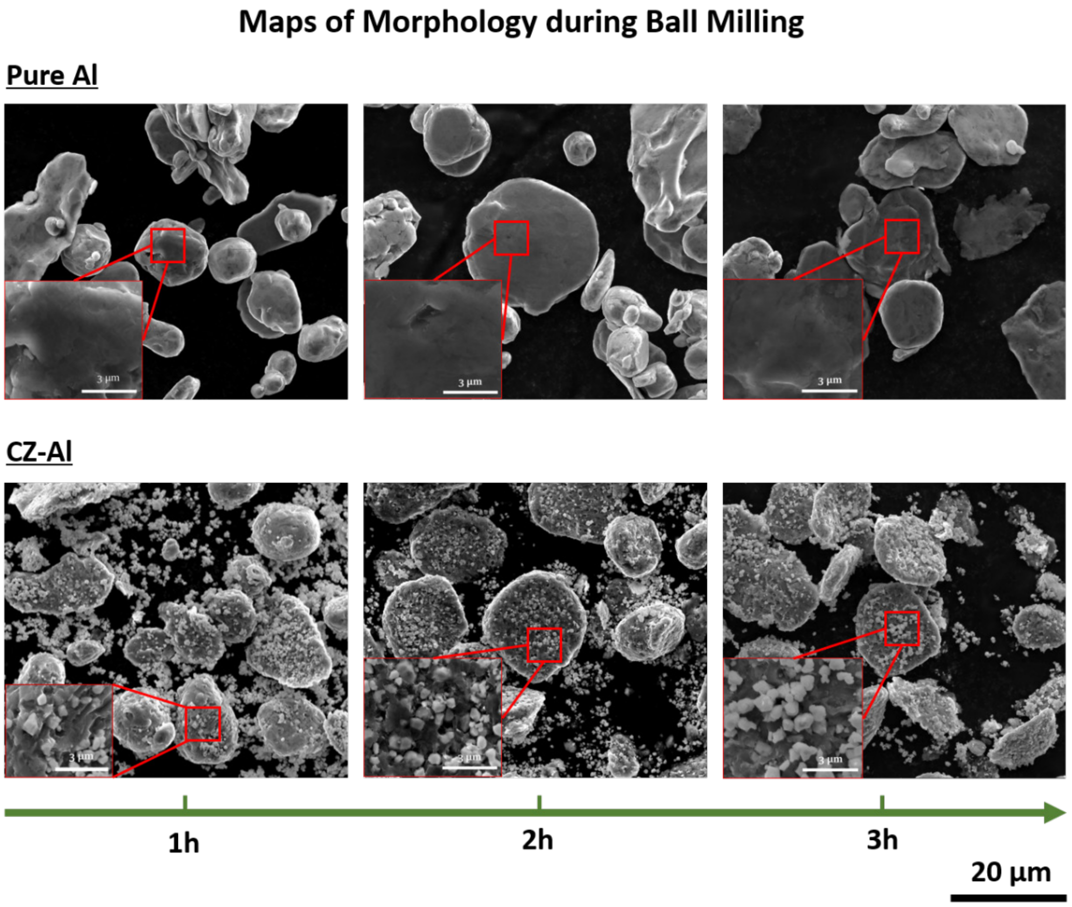

Figure 3. 6 Maps of Pure Al and CZ-Al via FESEM during Ball Milling Process from 1h to 3h. Scale bar with 20μm for basic image, while 3 μm for image zooming in with red border. All in the SE mode.

3.3.2 Hot Pressing Process

From Chapter 2, cofactor condition (crystal orientation) has a strong effect on the SME [24, 47, 48]. Before the characterization, it is important to establish the Coordinate

System for hot pressing direction and sample dimension. As is shown in **Figure 3. 7** (a), the bulk sample formed with hot pressing, in particular, bulk CZ-Al with transverse crack on the lateral surface (more microstructure analysis later). Based on the cylinder shape of sample, *xyz* Coordinate System is set. Two different planes are defined with the angles of hot-pressing direction. Therefore, hot pressing direction could be named after z axis.

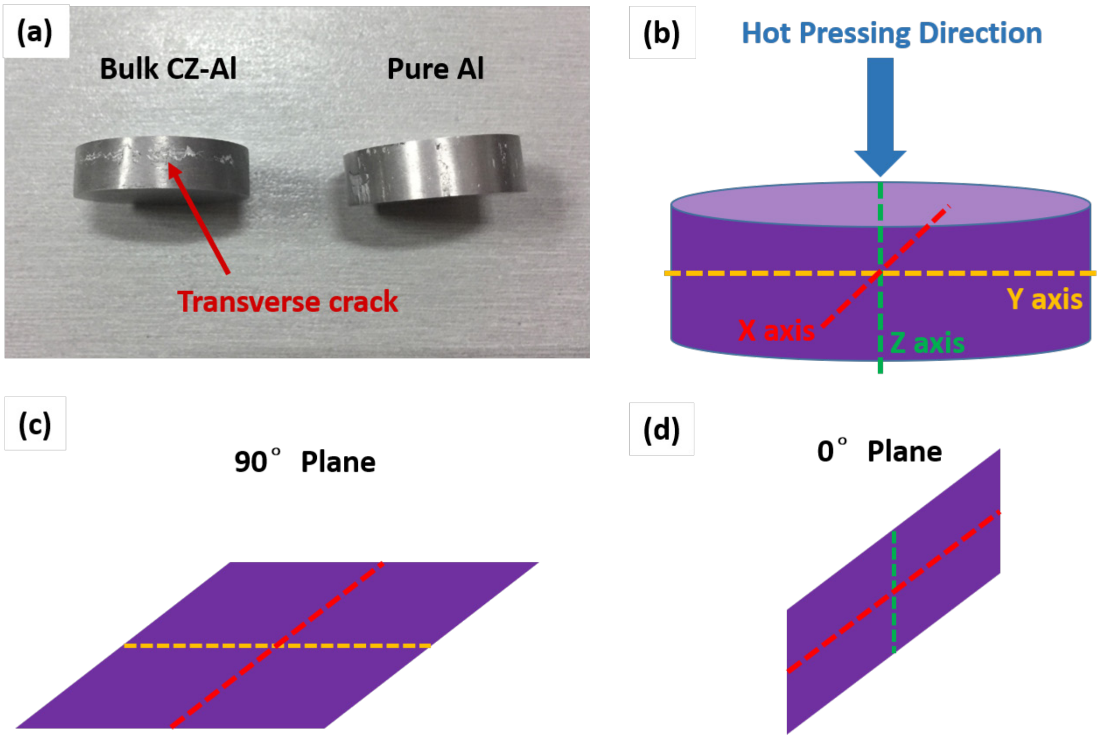

Figure 3. 7 Schematic diagrams of (a) Bulk CZ-Al (with transverse crack) and Pure Al, (b) modeling of bulk sample with the *xyz* Coordinate System, and definition of (c) 90° plane, (d) 0° plane.

Same procedures of FESEM were applied in hot pressing test. Bulk CZ-Al surface (90° plane) grinded with 2000# sandpaper grinding was detected (**Figure 3. 8**). There exists small amount of scratches, with CZ single crystals decorated. In fact, the properties are more concerned with the microstructure inside and surface could be polished or coated, how to characterize inside the sample came to a necessity.

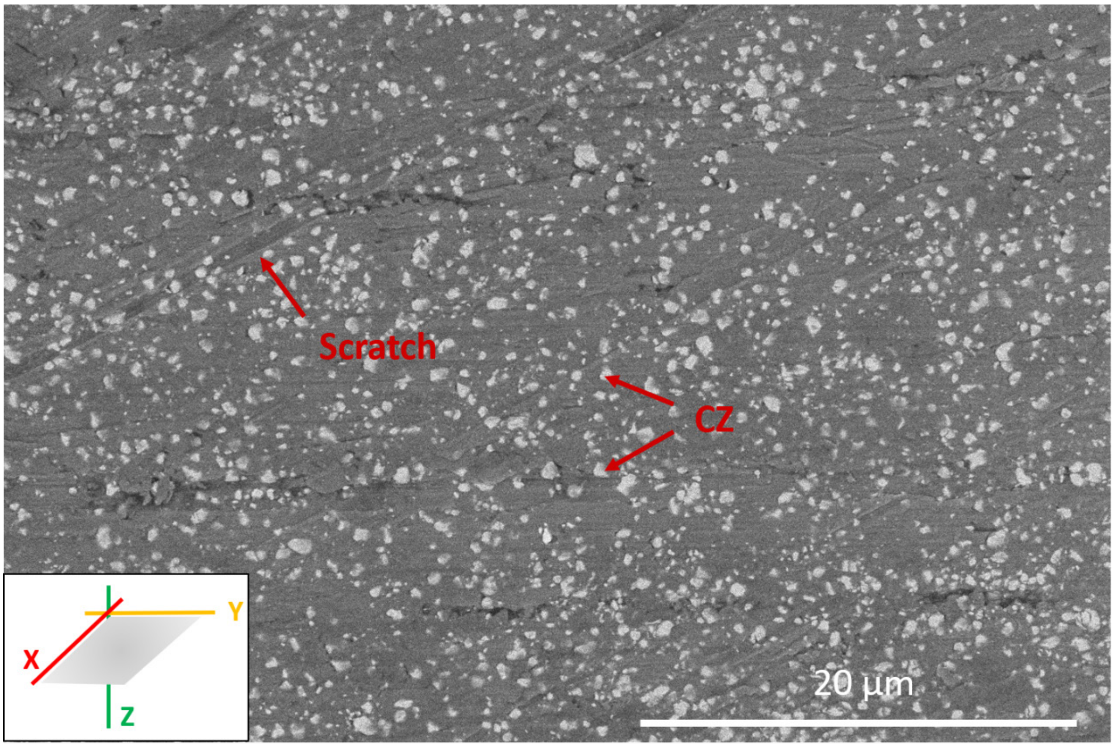

Figure 3. 8 FESEM BSE image of bulk CZ-Al surface (90° plane) with 2000# sandpaper grinding and without polishing.

In order to have a clear field inside the bulk sample, focus ion beam milling system (FIB, FEI Scios DualBeam) was applied to mill cross the section. In order to manipulate area in real-time, FIB-SEM system is used, with versatile ultra-high-resolution analytical ability (**Figure 3. 9** (a)).

It offers excellent sample preparation and 3D characterization performance for a wide and various sample, including magnetic and non-conductive specimen. The FIB system is equipped with both electron beam and ion beam, thus able to *in-situ* milling and imaging (**Figure 3. 9** (a)). The stage was tilted 52° in advance to make the surface of the samples perpendicular to the ion gun (**Figure 3. 9** (b)). With certain milling pre-set shape, such as rectangular slot marked red on the sample base, the microstructure inside the bulk sample could be characterized. Other functions (i.e. fabricating small volume pillar) will be discussed later.

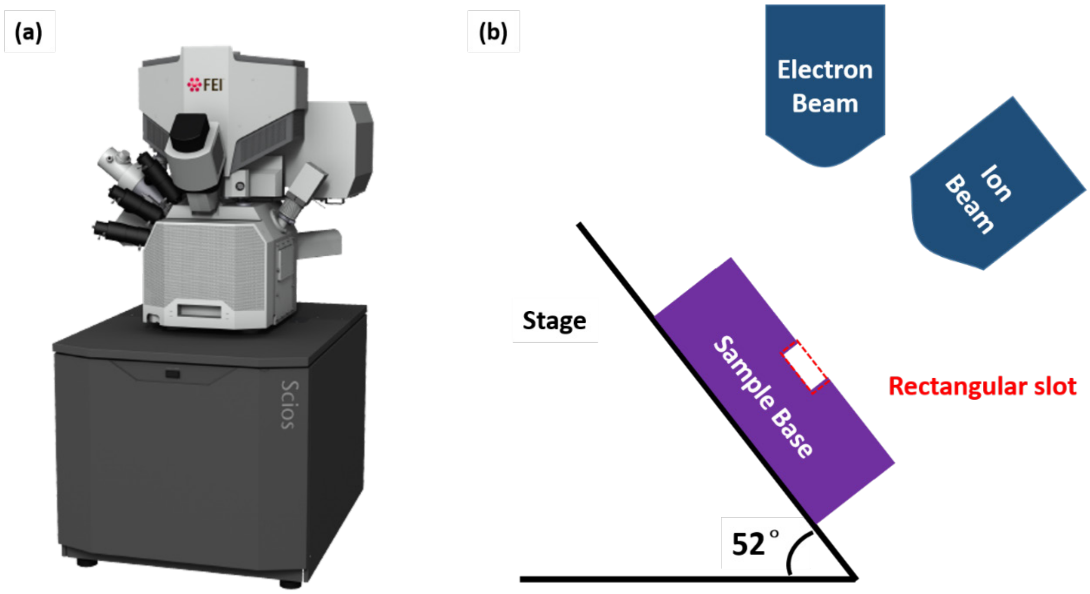

Figure 3. 9 (a) FEI Scios DualBeam FIB-SEM system, (b) Schematic illustration of relative positions of sample, stage, ion beam and electron beam in FEI Scios DualBeam FIB system.

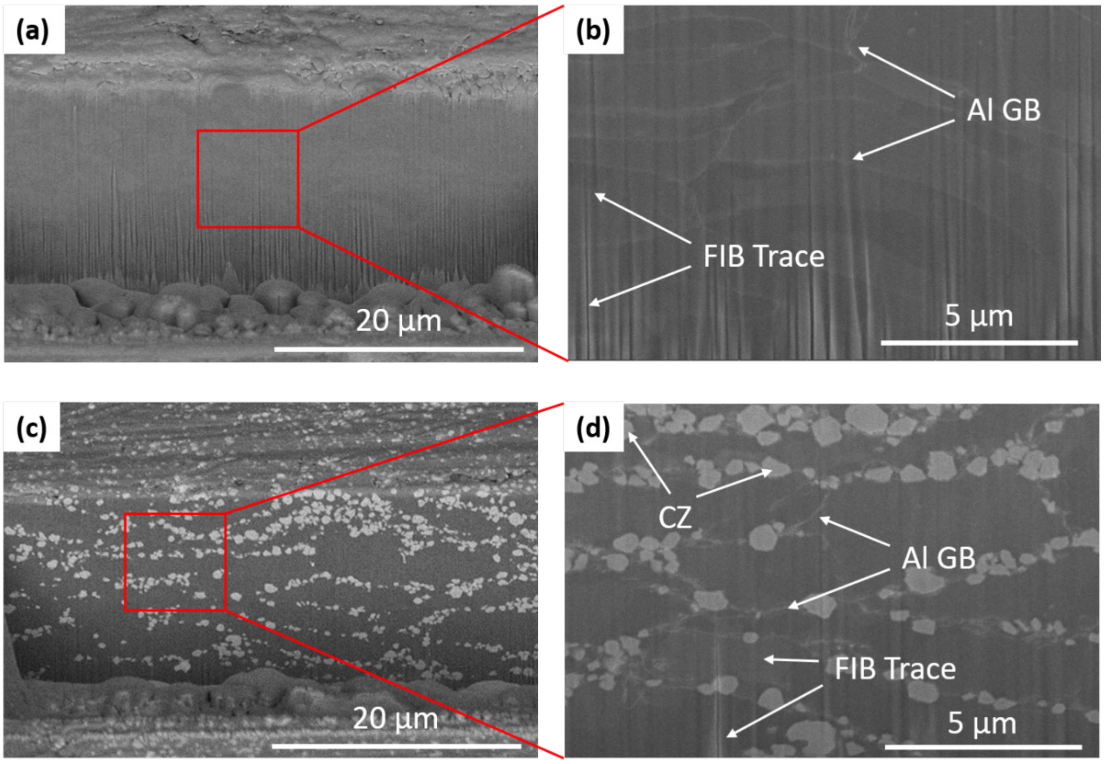

Figure 3. 10 FESEM BSE image of 0-degree plane (a) Pure Al, (c) CZ-Al with scale

bar 20 μm, and SE image of (b) Pure Al, (d) CZ-Al with scale bar 5 μm after hot pressing.

Such a FIB-SEM system was applied in hot pressing process. With FIB milling at ion beam current of 21 nA, rectangular slots were created separately and the cross sections of pure Al and CZ-Al are shown in **Figure 3. 10**. Under magnification of 8000×, it is difficult to distinguish the grain boundaries (GB) (**Figure 3. 10** (a), (c)), while it is obvious that both pure Al and CZ-Al are of high dense, with laminated structure along hot-pressing direction (z axis). As is shown in **Figure 3. 10** (b) after zooming in, clear Al GB and FIB trace were marked. The CZ single crystals are randomly distributed along the Al GB for Bulk CZ-Al (**Figure 3. 10** (d)).

To obtain more accurate density of sample, Archimedes Drainage Test (AD) was carried out and compared with the theoretical density. Density via AD was obtained by the **Equation 6** as follows:

$$\rho_{s-AD} = \frac{m_s \rho_l}{m_s - m_s'} \qquad \text{Equation 6}$$

where ρ_{s-AD} is the density of the sample via AD; ρ_l is the density of the test liquid; m_s is the mass of the sample and m_s' is the mass of the sample inside the test liquid. Owing to the small amount of PCA, we omit this term when calculating the theoretical density. Therefore, pure Al was approximated to 2.7 g/cm^3. For bulk CZ-Al, the density of the CZ single crystal is 5.85 g/cm^3, and weight ratio are shown in **Equation 7**:

$$m_{Al}: m_{CZ} = 7:3 \qquad \text{Equation 7}$$

Then with law of mixture [81], the theoretical density of CZ-Al composites was obtained as follows (**Equation 8**):

$$\rho_{CZ-Al-TH} = \frac{m_{Al} + m_{CZ}}{V_{Al} + V_{CZ}} = \frac{m_{Al} + m_{CZ}}{\frac{m_{Al}}{\rho_{Al}} + \frac{m_{CZ}}{\rho_{CZ}}} \qquad \text{Equation 8}$$

where $\rho_{CZ-Al-TH}$ is the theoretical density of CZ-Al composites; m_{Al}, V_{Al}, ρ_{Al} are respectively the mass, volume, density of the Al in CZ-Al; m_{CZ}, V_{CZ}, ρ_{CZ} are respectively the mass, volume, density of the CZ in CZ-Al. No considering the cracking or scratches and other mass loss. With simultaneous equations of **Equation 7** and **Equation 8**, $\rho_{CZ-Al-TH} = 3.22\ \mathrm{g/cm^3}$. The results are shown in **Table 3. 2**. Owing to the density measured via Archimedes Drainage extremely close to the theoretical one, the densification of each sample is good, which proves the hot-pressing process contributing to the basic formation and high density of bulk sample. It should be noted that since the stage was tilted 52°, the previous 0° plane shown in the image was also changed, thus to correct errors for measurement of grain size (in Chapter 4) if need be.

Table 3. 2 The density bulk sample Pure Al and CZ-Al via Archimedes Drainage Test (Unit: g/cm^3).

Bulk Sample	**Density via AD**	**Theoretical Density**
Pure Al	2.7	2.7
Bulk CZ-Al	3.22	3.22

3.4 Preparation of Small Volume CZ-Al

Concerned with the large grain size of Al, and CZ distributed along the Al GB, it pays that the prior step is to select the suitable area before the preparation of CZ-Al sample into small volume micro/nano-scale pillars. In this case, the ideal zirconia phase (tetragonal phase) of grain, and suitable pillar size to contain enough CZ single crystals will be obtained. Electron backscattered diffraction (EBSD, Aztec, Oxford Instrument) and the volume fraction of CZ in the CZ-Al composites was applied.

As a matter of EBSD (with be presented in Chapter 4), the aim is to index the suitable composition, phase and orientation. There is a procedure presented by Zeng, *et al.* in fabricating a ceramic pillar (**Figure 3. 11**) [25]. Different from the case in **Figure 3. 11**, CZ single crystals should retain the tetragonal phase during hybridization and

EBSD is done for assuming the phase existence. Meanwhile, volume fraction of CZ single crystals is taken into consideration in CZ-Al composites. Apart from 30 wt% weight of precursor ratio, the method can be applied in further regulation of system.

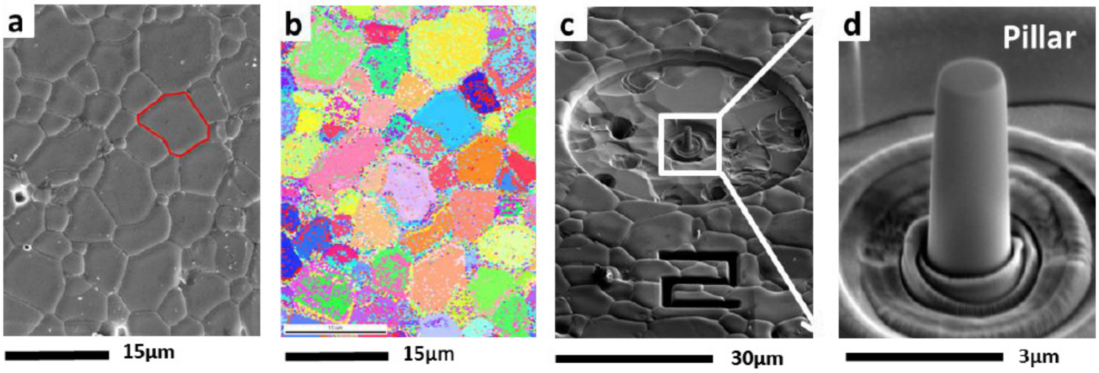

Figure 3. 11 The preparation procedure for a SMC pillar, including (a) select the grain with zirconia tetragonal phase, (b) obtain EBSD mapping of crystal orientation, (c) and (d) mill the pillar via FIB [25].

As a matter of volume fraction, the aim is to estimate the number of CZ single crystals inside the pillar. From histogram, average diameter is 559.86±147.8nm (More detail will be provided in Chapter 4). The result is close to the initial information that CZ has an average diameter around 500 nm. According to the estimation, the number of CZ in pillars with different diameters could be deducted. From **Table 3. 3**, there are 23 CZ single crystals even in the 2 μm pillars, which are suitable for further analysis.

Table 3. 3 The weight ratio, volume ratio and side ratio of CZ: Al, the number of CZ in different representative pillar diameter with statistic.

Ratio	Pillar Diameter	#CZ in Pillar
Weight - 30:69	2 μm	23
Volume - 0.165	3 μm	76
Side - 0.549	4 μm	181

From CZ-Al composites to CZ-Al micro-/nano- pillars, mechanical test has great influence on the pillar milling process. There are sufficient works about the micro-/nano- mechanical test and design of accurate micro-compression experiments. Concerned with aspect ratio (defined as height/diameter of pillar) of pillar, the numerical simulations carried out that the effect of the aspect ratio of the pillar on the mechanical behavior is relatively small, especially if the aspect ratio of the pillar is higher than 2 [82, 83], therefore, in the following experiment, the aspect ratio of pillar is kept at 3.

Since the geometry of pillar is eventful in the following mechanical test, the procedure of pillar with desired size and small tapping angle is provided with pre-trial as follows, combined with the flow chart of the small volume pillar preparation procedure via FIB (**Figure 3. 12**).

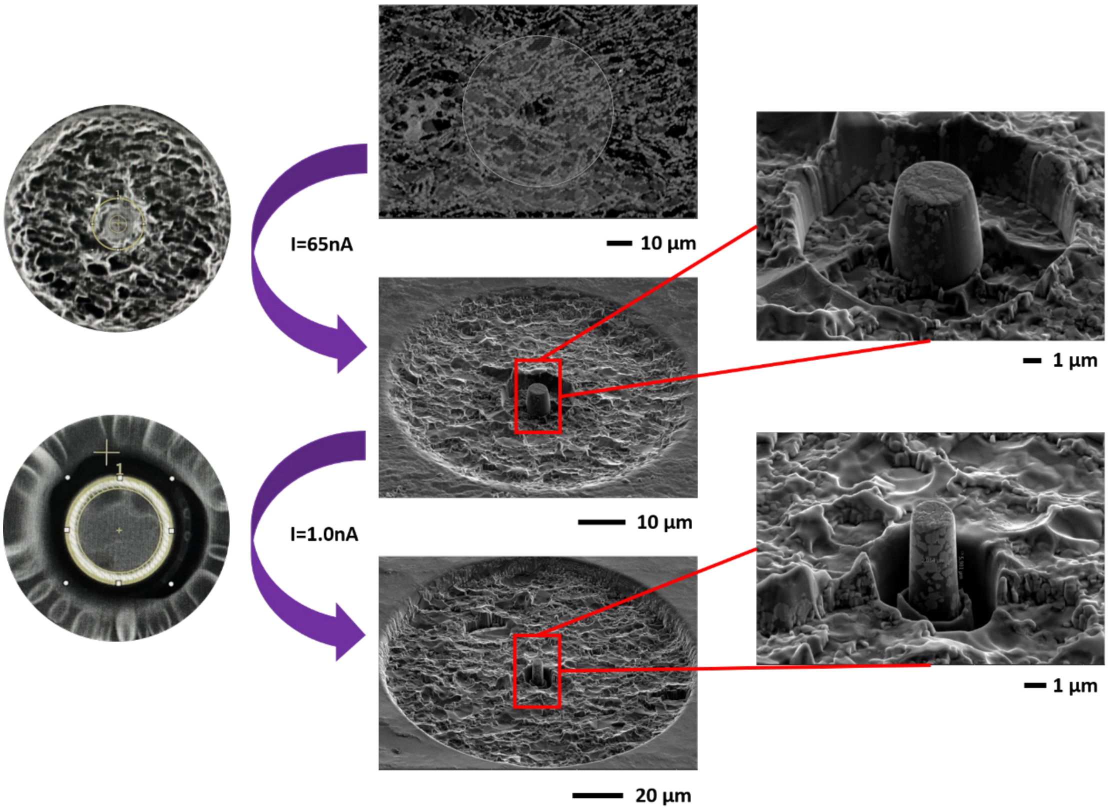

Figure 3. 12 Flow chart of the small volume pillar preparation procedure via FIB, take CZ-Al with diameter 2 µm as an example.

1. Deciding the equivalent diameter (d_{eff}) of pillar, such as 2 μm, 3 μm, 4 μm.
2. Calculating the first crater diameter according to the geometric relationship to be able to observe the pillar during *in-situ* compression when the stage is tilted to 75° (will be discussed in Chapter 4 in detail).
3. Milling with three steps. The first large crater at 65 nA, a designed size at 1.0 nA and final reducing tapering at 13 pA.

It has to be mentioned that the parameter will be changed slightly with different sample, and equivalent diameter is defined as:

$$d_{eff} = \sqrt{1/3(d_{top}^2 + d_{top}d_{bot} + d_{bot}^2)} \qquad \text{Equation 9}$$

where d_{top} and d_{bot} are the pillar diameters at the top and bottom, respectively. Moreover, the ideal modeling for CZ-Al micropillar was illustrated according to the 0-degree plane, size of Al flakes and CZ single crystals (**Figure 3. 13**).

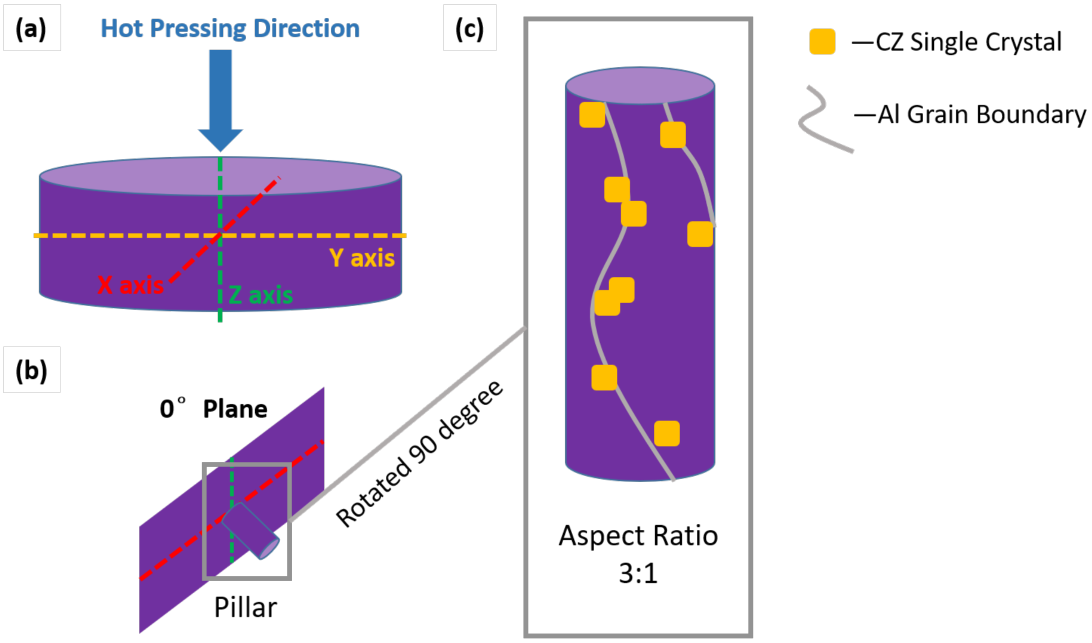

Figure 3. 13 Schematic illustration of modeling the CZ-Al micropillar based on the crystal orientation.

Then, 2 μm-size diameter CZ-Al and pure Al pillar were milled (**Figure 3. 14**). It has to be confirmed that more pillars will be prepared in future due to the random distribution of CZ single crystal in Al matrix. The thermo-mechanical test will be conducted in Chapter 4.

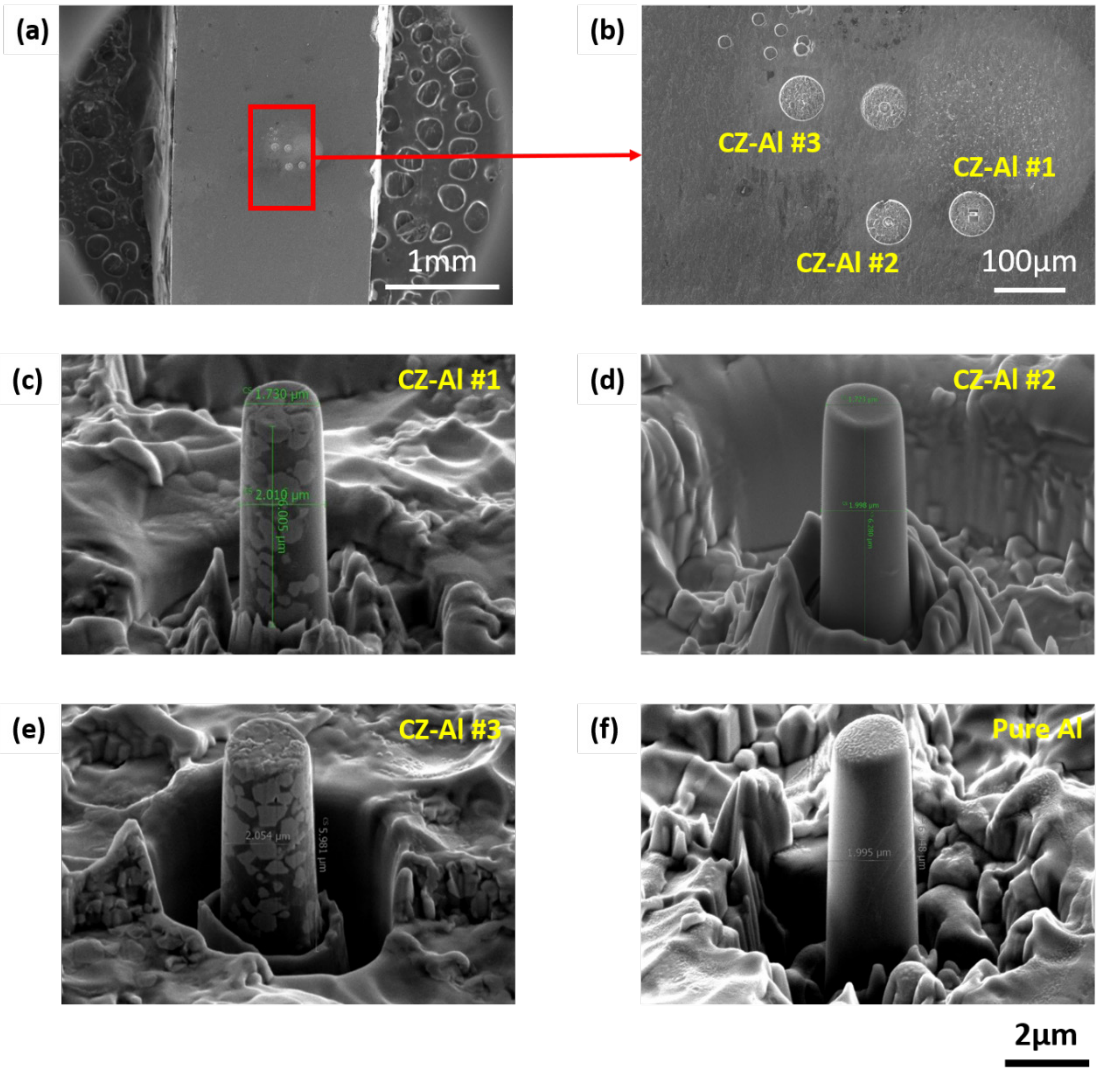

Figure 3. 14 FESEM image of micro-pillar after FIB milling ($d_{eff} = 2\mu m$, aspect ratio=3:1) with (a) relative position in bulk sample, (b) after zoom in, and (c) CZ-Al #1 (d) CZ-Al #2, (e) CZ-Al #3, (f) Pure Al.

3.5 Conclusive Remarks

The experimental methodology in chapter includes:

1. Developing a systematic experimental work procedure of studying fabrication method and properties of SMc.
2. Proving the rationality of ball milling and hot-pressing procedure and experimental parameters.
3. Fabricating the bulk CZ-Al and Pure Al sample with good dense, as well as a reasonable flow chart preparation via FIB in small volume pillar.
4. Presenting an overview structure and system composition of the CZ-Al sample, which lays a foundation for further characterization.

Chapter 4 Composites Characterization

This chapter discusses the characterization method of Cerium doped Zirconia reinforced Aluminum Matrix Composites (CZ-Al) on the structural aspects, such as morphology, phase composition and crystal orientation. Bulk and small volume CZ-Al were under thermo-mechanical test to systematically explore the size effect and matrix constraint on the composites, with the purpose of obtaining composites that have the suitable grain size and phase to develop shape memory composites (SMc) at small volume. Meanwhile, the reinforcement mechanism of the Cerium doped Zirconia (CZ) single crystal in Al matrix was raised.

4.1 Structural Characterization

The structural characterization involves the microstructure, grain size, phase composition, chemical composition distribution and crystal orientation. With various systematic procedures and equipment, it helps further analysis and understanding on functional characterization.

4.1.1 Microstructure and Grain Size

Microstructure and grain size are the foundations of structural characterization. Results can be carried out with measurement via FESEM (introduced in Chapter 3), analysis via ImageJ software (National Institutes of Health).

Surface morphology characterization of CZ-Al composites at various magnifications were tested, from ×1000 to ×30000 (**Figure 4. 1**). Good field to analyze micro-cracks, grain boundaries, grain size, shape and porosity is recommended under the magnification high than ×5000, especially for ×10000 CZ single crystals. All the images were captured at a voltage of 5 kV and an emission current of 50 pA.

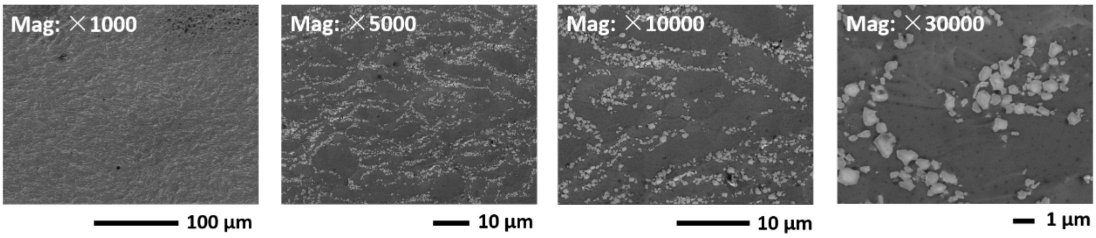

Figure 4. 1 FESEM images for the morphology characterization of CZ-Al composites on the suface at various magnifications.

For CZ-Al composites, Al and CZ hybridized together and hard to identify simply with FESEM image, then electron backscattered diffraction (EBSD, discussed in Section 4.1.4) was combined.

In sum, 114 CZ single crystals were selected, analyzed with OriginPro 2020 (OriginLab software professional for data analysis and graph fitting) and fitted with Lorentz Curve Type. As far as Al grains, it is hard to define the size since the hot-pressing process has reshaped the morphology. In this case, maximum and minimum diameters of grain are used for evaluation (shown in **Figure 4. 2**).

In fact, both EBSD and FESEM results shared almost the same diameter. In this way, combined with all the data shown above, CZ diameter could be estimated as 559.86±147.8nm. The result is close to the initial information that CZ has an average diameter around 500 nm. Meanwhile, there is no need for precise diameter data of Al grains, actually, 7 μm in maximum direction and 2 μm in minimum direction are enough for small volume pillar size selection and provident of hot-pressing effect (raw Al powders has a diameter around 10 μm).

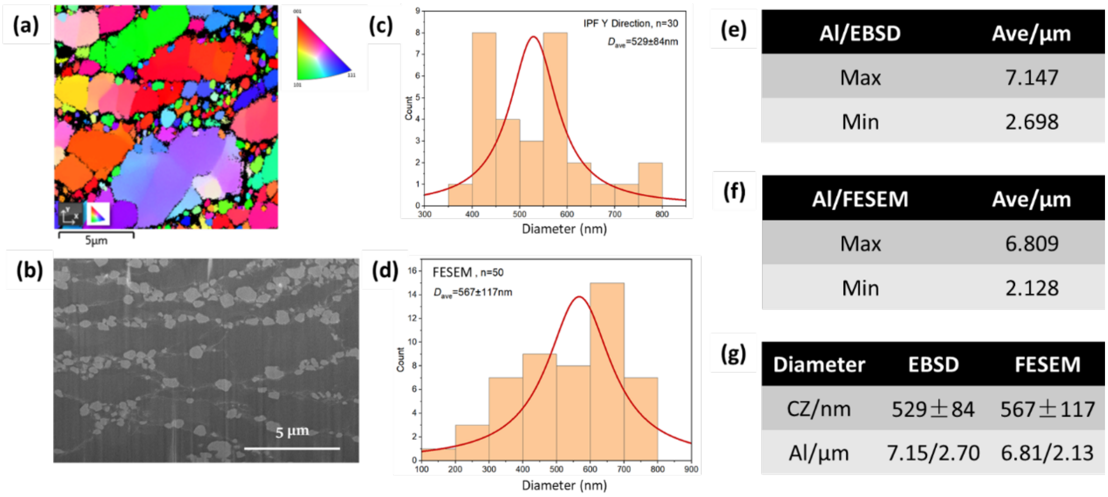

Al/EBSD	Ave/μm
Max	7.147
Min	2.698

Al/FESEM	Ave/μm
Max	6.809
Min	2.128

Diameter	EBSD	FESEM
CZ/nm	529±84	567±117
Al/μm	7.15/2.70	6.81/2.13

Figure 4. 2 Microstructure of CZ-Al with (a) EBSD image, (b) FESEM image, CZ diameter histogram via (c) EBSD, (d) FESEM, and Al diameter via (e) EBSD, (f) FESEM. (g) Summary of CZ and Al diameter.

4.1.2 Phase Composition

To characterize different phase and ratio in CZ-Al composites, X-ray diffraction (XRD, Rigaku D/Max 2550 PC) was applied for bulk sample. Phase transition in Micro-/nano pillars during mechanical test will be carried out in the Section 4.3 via Transmission Electron Microscopy (TEM). XRD test obeys the Bragg's Law [84] (Simplified version of Laue's Law),

$$n\lambda = 2dsin\theta \qquad \text{Equation 10}$$

where n is an integer, λ is the wavelength of X-rays and d is the distance between two close planes. Diffraction peaks present that the high interference happens at certain 2θ. With the analysis of MDI Jade 6.0 (Materials Data, Inc.) and characteristic diffraction peaks of zirconia in standard PDF2-2004 card indexation and comparison (**Figure 4. 3**), the results were presented in **Figure 4. 4**.

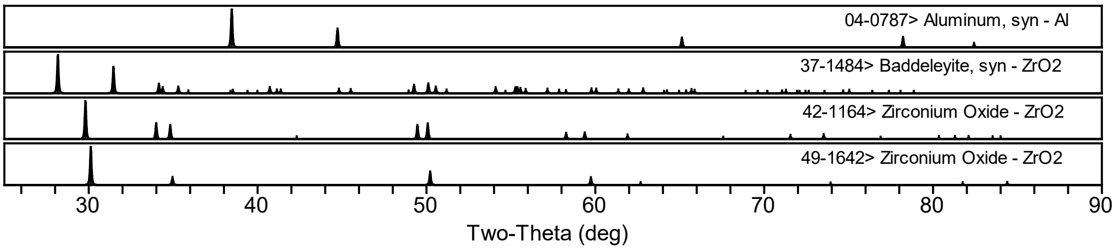

Figure 4. 3 Typical XRD spectra of Aluminum phase (Al, 04-0787), monoclinic zirconia (m, 37-1484), tetragonal zirconia (t, 42-1164) and cubic zirconia (c, 49-1642) from standard PDF card with their characteristic peaks.

As the XRD results indicated (**Figure 4. 4**), the characteristic peaks monoclinic zirconia is the major phase in CZ single crystal, while tetragonal zirconia becomes the major in CZ-Al bulk sample. It can be inferred that tetragonal zirconia has been stabilized with Al matrix constraint during the fabrication.

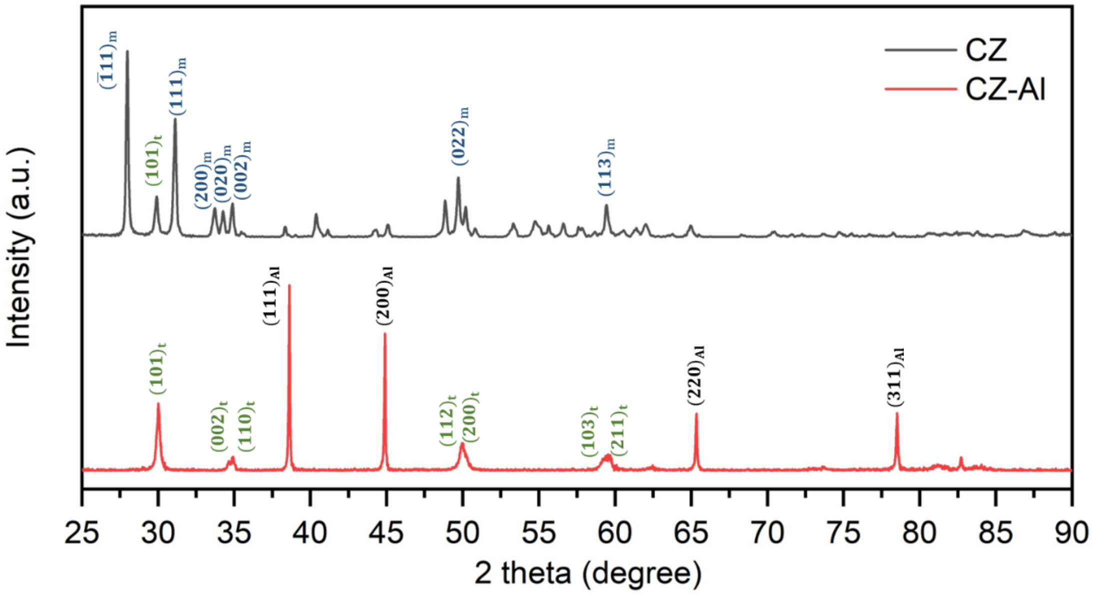

Figure 4. 4 XRD spectra of CZ powders (in the form of single crystal) and CZ-Al bulk sample with their characteristic peaks.

Compared with the Aluminum standard PDF card (PDF#04-0787, Aluminum, syn),

(111), (200), (220) and (311) planes were almost fitted, while at relatively large angle, there is a sight error, mainly accounting from the testing process. It should be mentioned that the pre-set stress during hot-pressing procedure should have induced lattice shrinkage, while no obvious shifting happened. It may be Al grain relaxation. Specific calculation of reduced stress will be carried out in future.

In a real case, XRD can not only be done for phase probing, but also calculating the weight ratio of different phases according to the relative intensities of the diffraction peaks before and after the thermo-mechanical test (the latter will be shown in Section 4.3) [85].

The weight fraction of the three phase, monoclinic phase X_m, tetragonal/cubic phase $X_{t/c}$ could be expressed by **Equation 11**, **12**, respectively [86]:

$$X_m = \frac{I(11\bar{1})_m + I(111)_m}{I(11\bar{1})_m + I(111)_m + I(101)_{t/c}} \qquad \text{Equation 11}$$

$$X_{t/c} = 1 - X_m \qquad \text{Equation 12}$$

where $I(111)_m$, $I(11\bar{1})_m$, $I(101)_{t/c}$ are the integrated intensity from the monoclinic (111), $(11\bar{1})$ peaks, the tetragonal/cubic (101) peak, respectively. With basic calculation, $X_m = 88.246\ wt\%$ in CZ single crystals, while $X_m = 0\ wt\%$ in CZ-Al composites. It proves that with the matrix constraint, all the CZ with monoclinic phase zirconia were transferred into the tetragonal phase.

4.1.3 Chemical Composition Distribution at grain-scale

Since XRD gives an overall chemical composition in the bulk CZ-Al composites, it is of great importance to develop a method for resolution at grain-scale, especially when composition has strong effect on the SME and small volume pillar has been under compression in the Section 4. 3.

In order to have a clear view on the grain, SEM with EDX (Energy-dispersive X-ray spectroscopy) detector is applied.

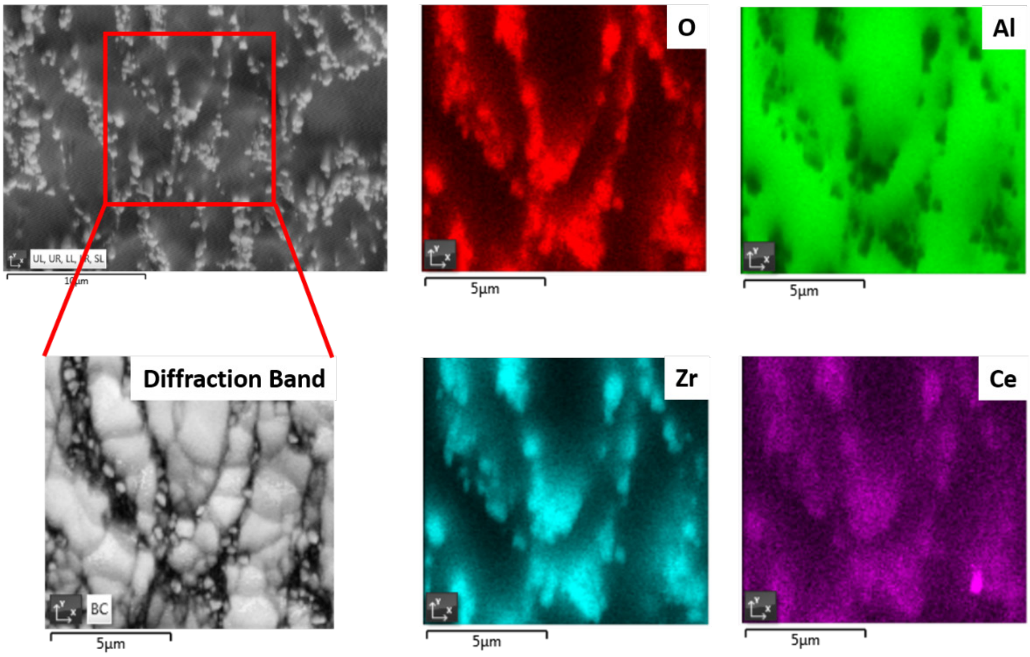

Figure 4. 5 EDX elemental maps of bulk CZ-Al composites, including the FESEM, BSE image, diffraction band, and the oxygen, aluminum, zirconia and cerium mapping.

It is apparent that most of Al on the matrix have not been oxidized, while Zr, Ce, and O distributed along the Al GB and stayed the same area, which indicated no atom diffusion happened during the fabrication (**Figure 4. 5**).

FESEM-EDX system is of great convenience on microscale observation, especially at grain boundaries. Whereas, the phase transition always happens at nanoscale, and under the situation, TEM-EDX is much more helpful and will be discussed later.

4.1.4 Crystal Orientation

Crystal orientation serves as one of the controlling factors of martensitic transformation behavior. The distribution of crystal orientation at grain-scale was mapped with EBSD. Before EBSD, a proper sample surface is required to obtain better results. With 2000# sandpaper grinding, as well as mounting (Simplimet 3000, Buehler, US, **Figure 4. 6** (a)), automatic grinding and polishing (AutoMet 300, Buehler, US, **Figure 4. 6** (b)), and final ion polishing (Fischione 1060, Funa, Shanghai, **Figure 4. 6** (c)), samples could be detected via EBSD. To simplify the system and emphasize more on the inner factor, 0-degree plane was prepared in advance from two samples, pure Al and bulk CZ-Al, since 0-degree place reflected on the hot-pressing section morphology. Different planes will be discussed in future as a part of cofactor condition [48].

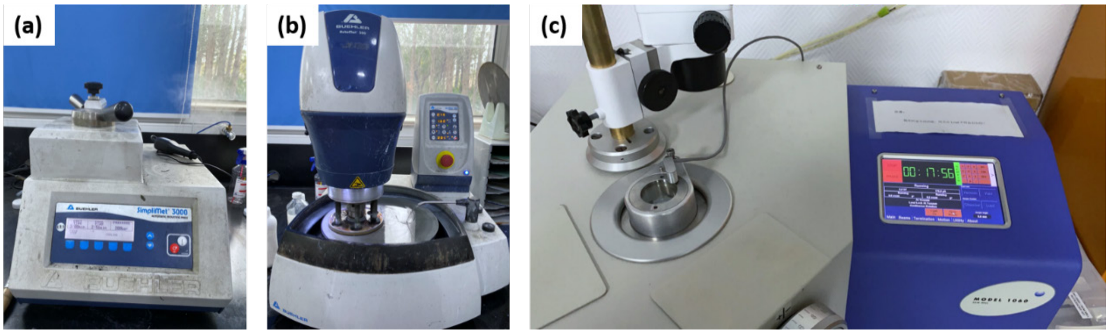

Figure 4. 6 Schematic diagram of EBSD specimen preparation via (a) mounting, (b) grinding and polishing, (c) ion polishing.

With a tilted angle of 70° and high voltage of 20 kV, backscattered electrons (BSE) can detect the crystal orientation based on the Kikuchi bands. In practice, a color mapping image will be obtained by the reflection of BSE from the surface. As far as zirconia ceramics, there are three phases, m, t, c phase (mentioned in Chapter 2). Inverse pole figure of t-phase zirconia and Al indicated phases are randomly distributed and no texture formed during the fabrication (**Figure 4. 7** (b), (d)). Herein, CZ single crystal keeps a single orientation without subcrystalline. There is clear orientation difference between Al matrix and CZ dopant. The interface relationship will be explored later via TEM. With specific spot indexation, Kikuchi line pattern proved the existence of t-phase ZrO_2 (**Figure 4. 7** (e)).

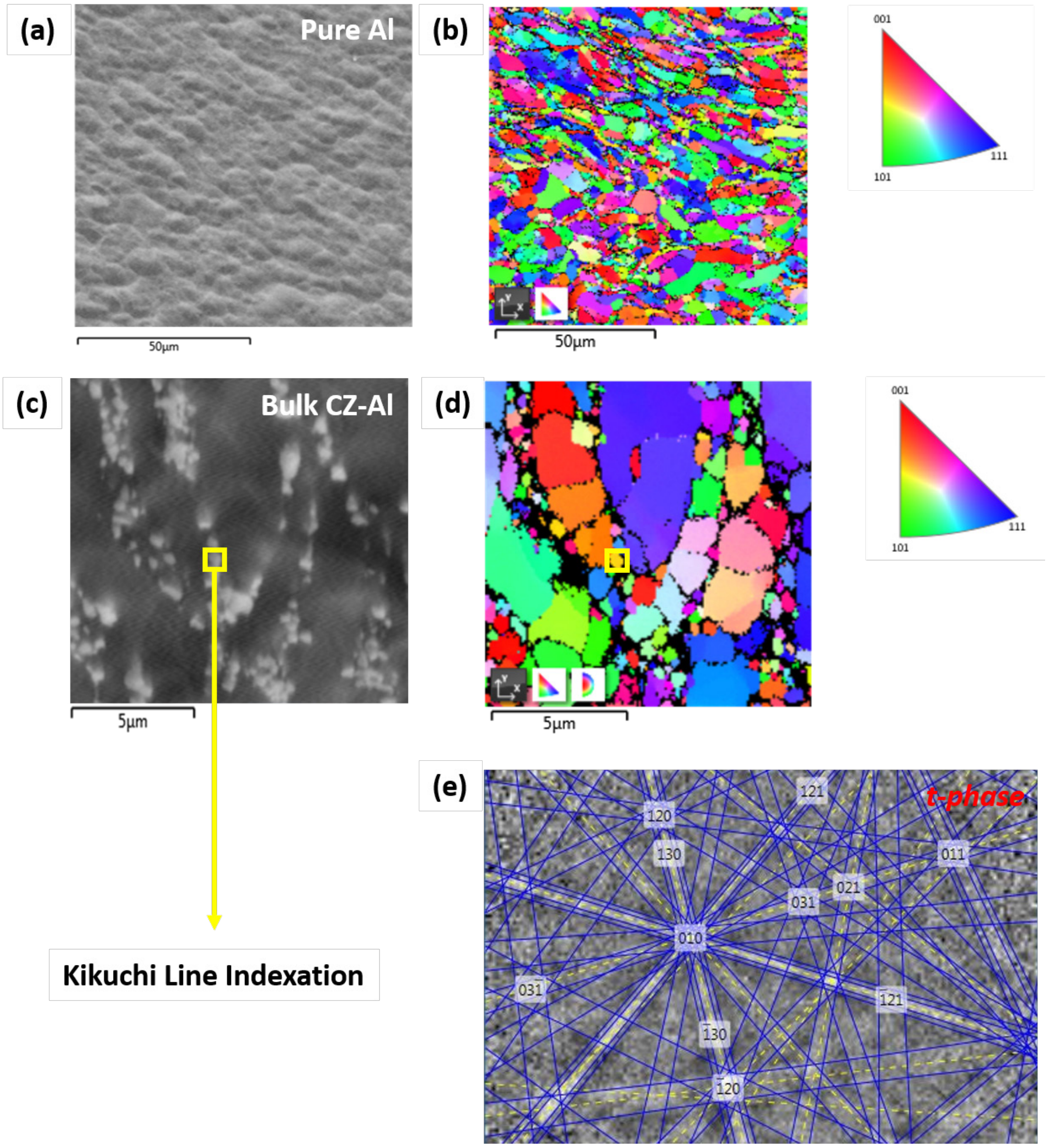

Figure 4. 7 EBSD map of pure Al with (a) FESEM-BSE image, (b) IPY direction pattern in inverse pole figure of Al, and bulk CZ-Al with (c) FESEM-BSE image, (d) IPY direction pattern in inverse pole figure of t-phase ZrO_2. (e) Kikuchi line pattern for t-phase ZrO_2 in (c) highlighted with yellow frame.

4.2 Motivation for Small Volume

Previous work has done to know the structure of CZ-Al composites from composition to the distribution. Combined with the zirconia phase mentioned in Chapter 2, zirconia phase in different samples can be concluded in **Table 4. 1**.

1. For pure ZrO_2 without any doping, it stays the monoclinic phase according to the phase diagram. (presented by #1)
2. The major phase transfers to tetragonal phase with 12 mol% ceria doped in bulk CZ. (presented by #2)
3. When CZ single crystals (diameter = 559.86±147.8nm, presented before) are formed, there is no particles constraints surroundings as well as the diameter is not small enough to form tetragonal phase, the monoclinic phase is the major. (presented by #3)
4. With matrix constraint, tetragonal phase is the major in bulk CZ-Al. More precise analysis on major phase will be conducted by **Equation 3** in future. (presented by #4)

Table 4. 1 Major phase of zirconia and domain factor in different samples.

Number	Bulk Sample	Major Phase	Domain Factor
#1	Pure ZrO_2	*m*	/
#2	Bulk CZ	*t*	Dopant Effect
#3	CZ Single Crystal	*m*	Surface Energy
#4	Bulk CZ-Al	*t*	Matrix Constraint

As the SMC research indicated, polycrystal ceramics are fragile and sensitive to the external stimuli and cracks. With the small volume, the internal stress at the grain boundaries will be released in time. In the meantime, bulk sample could only offer the properties in a statistical meaning, blocking the way to test the enhancement of CZ single crystals under different conditions (i.e. surface-to-volume ratio, numbers of CZ in the pillar). In this case, it pays that micro-/nano- pillar at small volume with the following thermo-mechanical test is an attempt for composites enhancement mechanism.

4.3 Thermo-Mechanical Characterization

Thermo-mechanical test was conducted based on structural condition. Both bulk sample and small volume pillars were tested to reveal the enhancement mechanism.

4.3.1 Bulk CZ-Al

Vickers Hardness Testing (TMHV-1000 (Z), Shanghai Tuming Optical Instrument Co., Ltd.) is a fundamental test with the advantage of great convenience and high efficiency, which is always adopted as the first step for mechanical test.

Basically, CZ-Al has an average hardness 67.2% higher than Pure Al (**Table 4. 2**), which offers a preliminary result for CZ single crystal enhancement at macroscale.

Table 4. 2 Hardness of Pure Al and bulk CZ-Al via Vickers hardness test.

Bulk Sample	**HV**	**Enhancement**
Pure Al	50.9±0.8	67.19%
Bulk CZ-Al	85.1±0.2	

To obtain more accurate results, mechanical test was conducted further on the pure Al and bulk CZ-Al, i.e. uniaxial tensile test and compression test via Universal Material Test System (3340, Instron Co.) and analyzed on Bluehill Universal (Illinois Tool Works Inc.), as is shown in **Figure 4. 8** (a). The area marked with red frame can be changed in a compression mode (**Figure 4. 8** (b)) or tensile mode (**Figure 4. 8** (c)), and each test used three specimens prepared in a pre-set size shown in **Figure 4. 8** (e)-(g), marked as #1, #2, #3 with Comp. or Tens. and CZ-Al or Al.

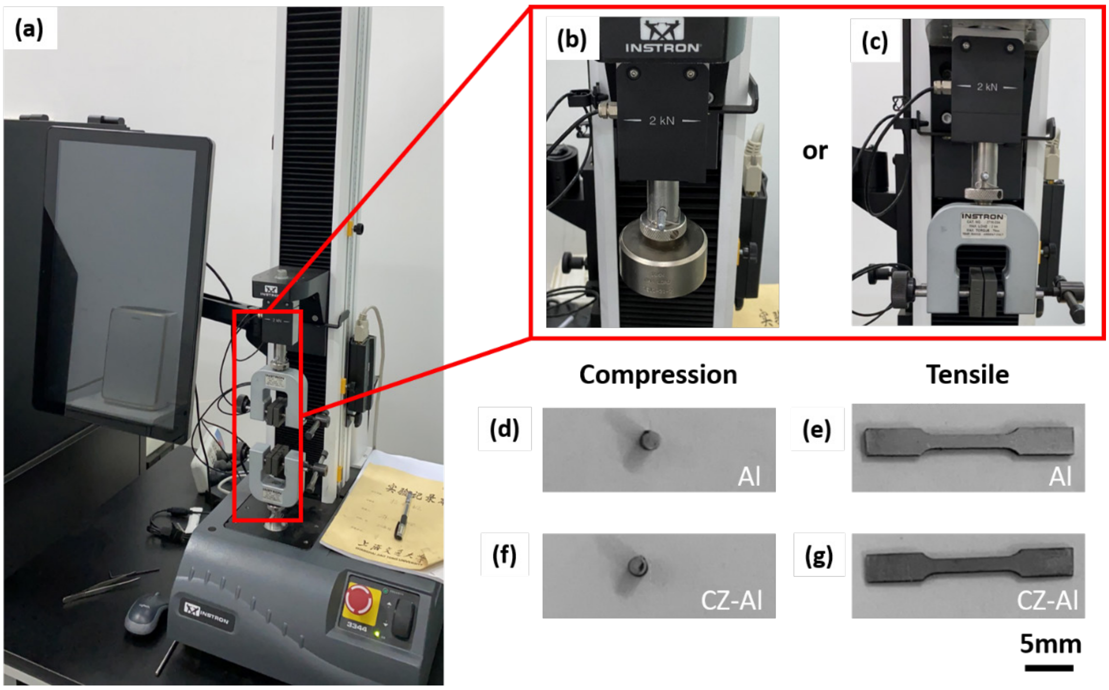

Figure 4. 8 Schematic diagrams of (a) Universal Material Test System, setup for (b) compression mode and (c) tensile mode, pure Al specimens for (d) compression test, (e) tensile test, and bulk CZ-Al specimens for (f) compression test, (g) tensile test.

The stress-strain curve is plotted in **Figure 4. 9**. the test was done every time the fracture happened, which corresponds to the cross with different color. In detail, ductile fracture happened in compression test, while brittle fracture happened in tensile test. From the curve, Young's Modulus E shares similar results (CZ-Al relatively lower) while all of them are far too low than the real case, which may be induced by testing without extensometer limited to the bulk sample size and the space between the indenter. More accurate data on tensile test will be explored in future. Whilst, the data can still be used in extra evidence for CZ single crystal enhancement of strength as well as toughness.

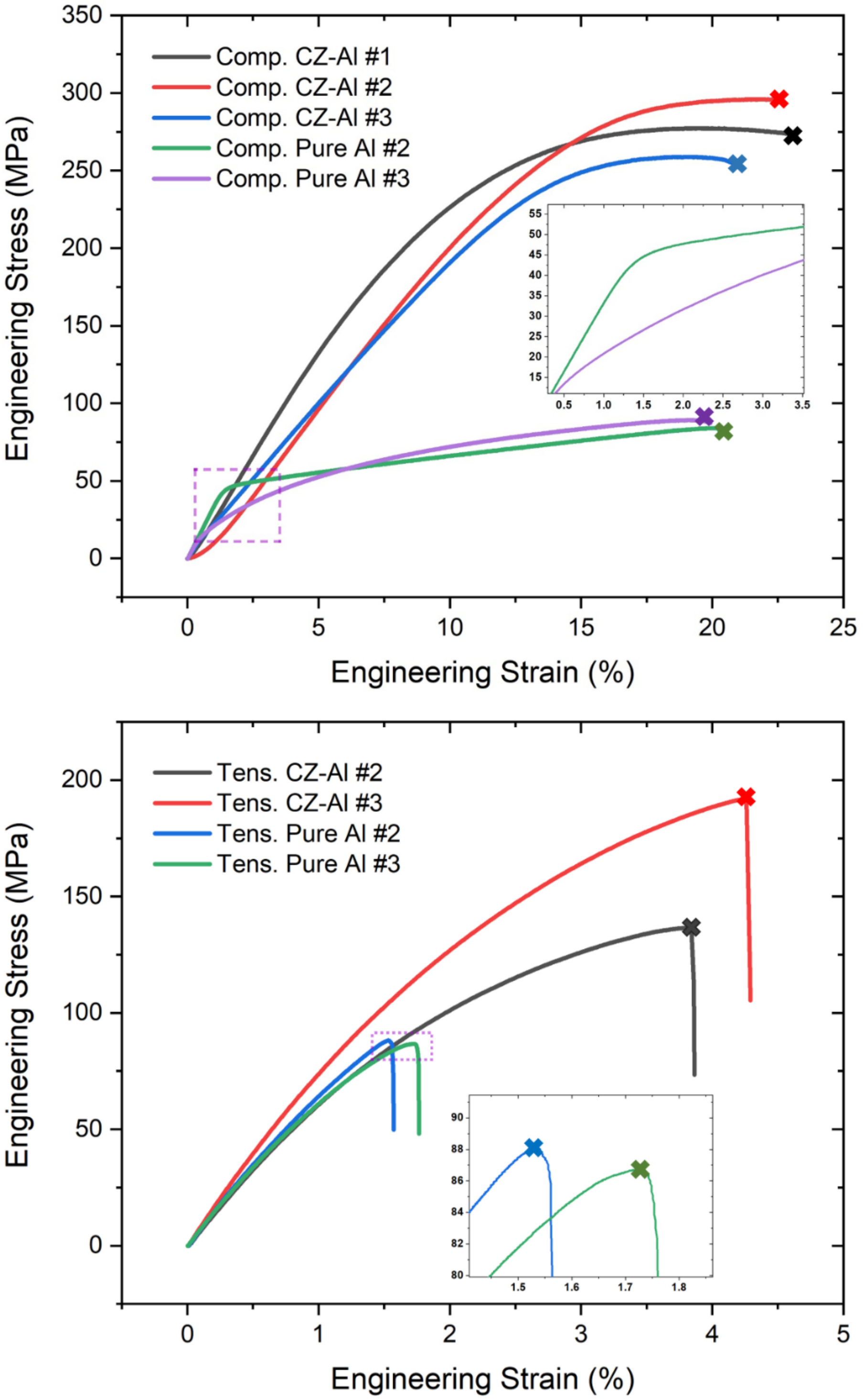

Figure 4. 9 Engineering stress- Engineering strain curve of CZ-Al, pure Al bulk sample tensile and compression test.

From the engineering stress- engineering strain curve, the precise data of parameters for mechanical test, i.e. yield strength σ_s, tensile strength σ_b (for Tens. #sample), compressive strength σ_{bc} (for Comp. #sample) are concluded in **Table 4. 3**.

Table 4. 3 CZ-Al and Pure Al Parameters for Mechanical Test (Unit: MPa).

Sample	Number	σ_s	σ_b/σ_{bc}	Fracture Strain %
Al	Comp. #1	---	---	---
	Comp. #2	45.7	83.8	21.6
	Comp. #3	18.6	89.1	19.1
	Ave.	**32.2±13.6**	**86.5±2.7**	**20.3±1.3**
CZ-Al	Comp. #1	169.2	277.1	22.5
	Comp. #2	189.1	295.9	21.8
	Comp. #3	178.3	258.7	20.9
	Ave.	**188.4±8.1**	**277.2±15.2**	**21.7±0.8**
Al	Tens. #1	---	---	---
	Tens. #2	56.3	88.2	1.5
	Tens. #3	52.7	86.7	1.7
	Ave.	**54.5±1.8**	**87.4±0.7**	**1.6±0.1**
CZ-Al	Tens. #1	---	---	---
	Tens. #2	89.0	135.9	3.8
	Tens. #3	71.7	191.3	4.2
	Ave.	**79.8±9.2**	**163.6±27.7**	**4.0±0.2**

(Note: --- represents the failure from the mechanical test.)

The compressive yield strength of CZ-Al is 188.4±8.1 MPa, 486.0% higher than that of pure Al. The tensile yield strength of CZ-Al is 79.8±9.2 MPa, 46.5% higher than that of pure Al. Meanwhile, compressive strength of CZ-Al is 277.2±15.2 MPa, 220.6% higher than that of Al, and tensile strength of CZ-Al is 163.6±27.7 MPa, 87.1% higher than Al. The compressive fracture strain of CZ-Al is 21.7%±0.8%, 6.9% higher than pure Al, which is relatively close and indicated that Al matrix domains the ductility of composites, CZ nanoparticles has limited effect on ductility. The tensile fracture strain of CZ-Al is 4.0%±0.2%, 150.0% higher than that of pure Al, indicating CZ nanoparticles could inhibit laminated structure from shear fracture to some extent. More mechanism interpretation will be conducted in FESEM results.

The XRD spectra for CZ-Al #1 after uniaxial compression at 277MPa stress is shown in **Figure 4. 10**. There exist mainly three phases, Al, tetragonal zirconia (t), monoclinic zirconia (m). According to **Equation 11, 12**, phase weight ratio could be calculated.

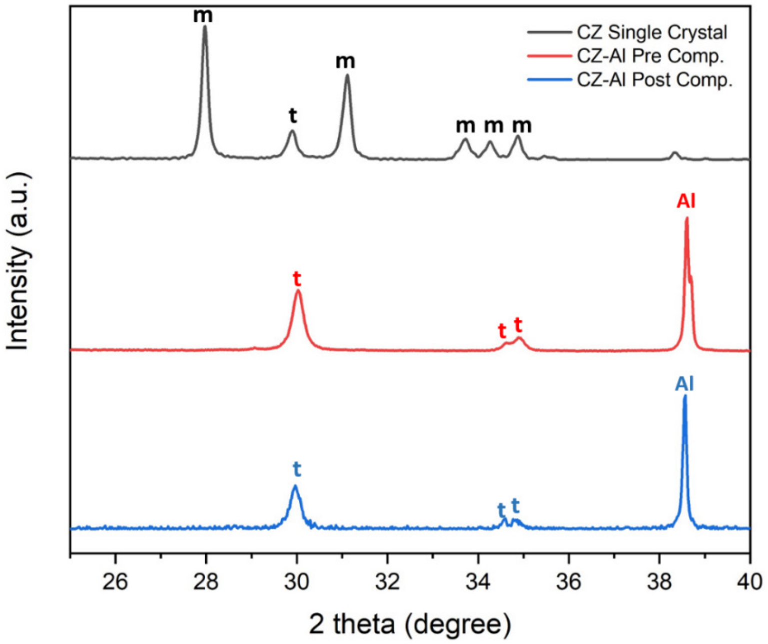

Figure 4. 10 XRD spectra in 25-40 degree for CZ and CZ-Al #1 bulk sample before and after uniaxial compression, where the characteristic peaks and corresponding crystal plane index (hkl) of Al, t-phase of zirconia, m-phase of zirconia are marked.

In sum, there is $X_m = 0\,wt\%$ in post compressed CZ-Al bulk sample, which indicated that no monoclinic zirconia was found in the post compression. There are three reasons accounting for absence of m-ZrO_2.

1. Only the phase of zirconia on the shear plane transformed;
2. Recovery to tetragonal phase when unloading;
3. 277MPa is the uniaxial compression force. The real stress passing on the CZ in Al matrix may be smaller and cannot reach the critical stress.

Combined with the XRD data in **Figure 4. 4**, different phase weight ratios in CZ single crystal, CZ-Al bulk sample and compressed CZ-Al bulk sample are summarized in **Figure 4. 11**. According to the stress-induced martensite transformation, the phase ratio results offer a good base for further analysis.

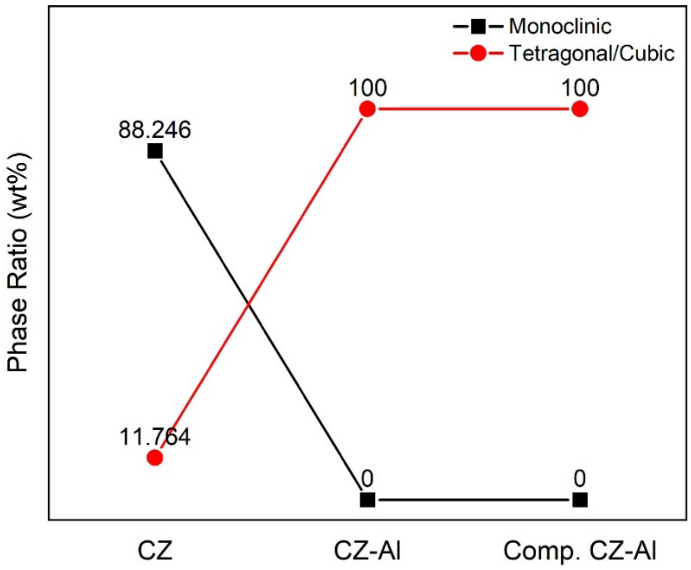

Figure 4. 11 Different phase weight ratio in CZ single crystal, CZ-Al bulk sample and compressed CZ-Al bulk sample.

Due to the low stress level of tensile test compared with compression test, and the laminated structure induced by hot pressing, XRD is not the prior choice for tensile test characterization. FESEM image of fracture section was presented in **Figure 4. 12** combined with the engineering stress- engineering strain curve. As to pure Al #2, #3, the laminated structure of Al flakes acts like a tide wave, which could account from the tensile stress applied to induce the habitat plane slipping. As to CZ-Al #2, #3, the section turns to be like a honeycomb made of Al, and CZ single crystals are decorated into the hole.

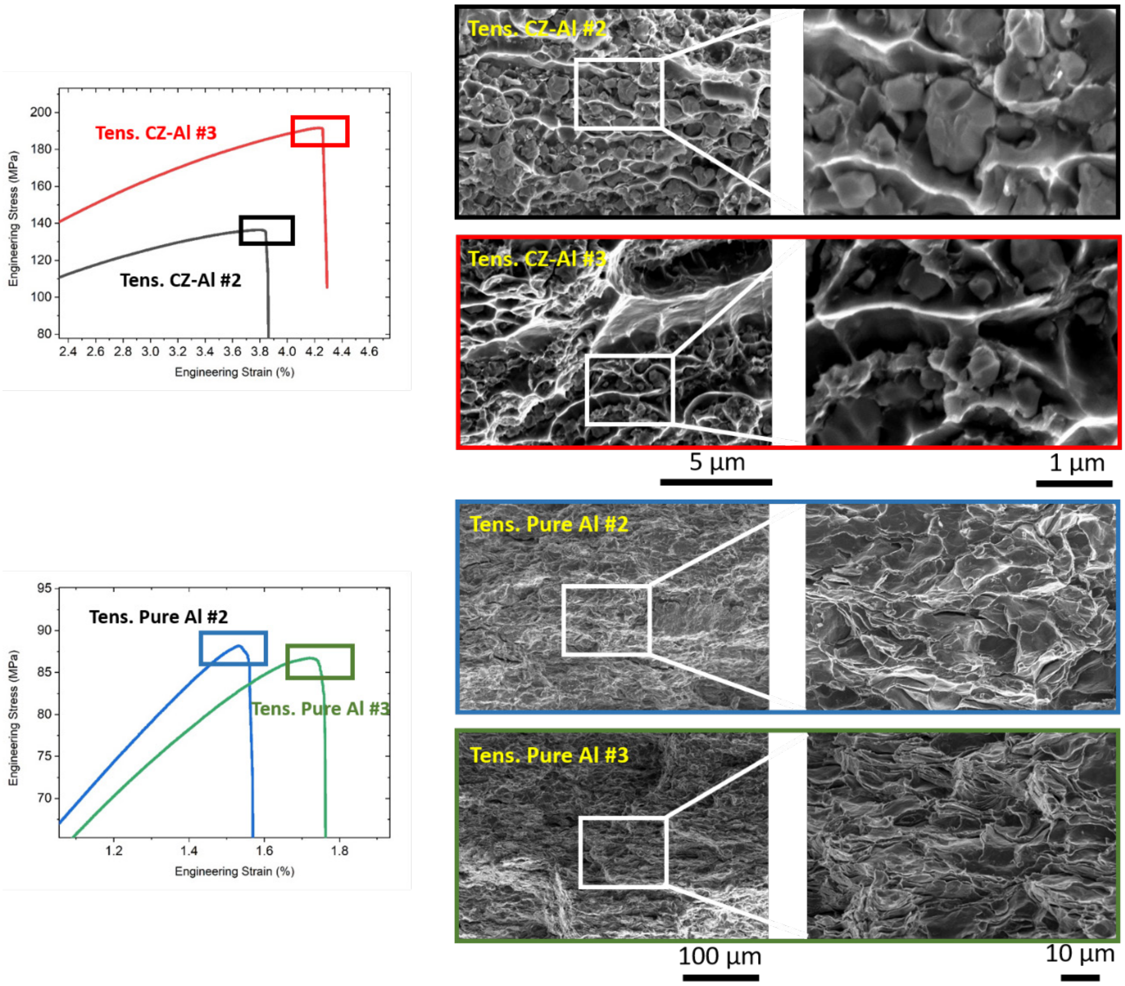

Figure 4. 12 FESEM of fracture section after uniaxial tensile test combined with engineering stress- engineering strain corresponded with different sample.

Compared with the image of pure Al and pristine FIB section of FESEM image in **Figure 4. 1**, the Al matrix in CZ-Al is more condensed with higher deformation and CZ were detached from the hole possibly due to the absence of matrix and occurring martensite transformation, which triggered the volume expansion and shear strain.

Herein, we suppose that *when the stress on the CZ single crystals conducted from Al matrix deformation is retracted, the martensite transformation will occur with which the volume is expanded and shear strain is induced to enhance the matrix and have the*

CZ detached.

4.3.2 Small Volume CZ-Al Pillars

Based on the bulk sample test, small volume pillars prepared via FIB (presented in Chapter 3) were under nanomechanical test, which was performed with Nano indenter (G200, Agilent Technologies, Inc. and NanoFlip, Nanomechanics Inc.).

As far as G200 (**Figure 4. 13** (a)), it is an *ex-situ* Nano indenter equipped with a Berkovich-geometry diamond indenter with a maximum load around 500mN.

As far as NanoFlip (**Figure 4. 13** (b)), different from G200, it is an in-situ Nano indenter, which allows to operate in the SEM chamber with the real-time focus ion beam and electron beam to record. The sample has a position perpendicular to the stage. It provides a maximum load around 50mN and *in-situ* simultaneously SEM control.

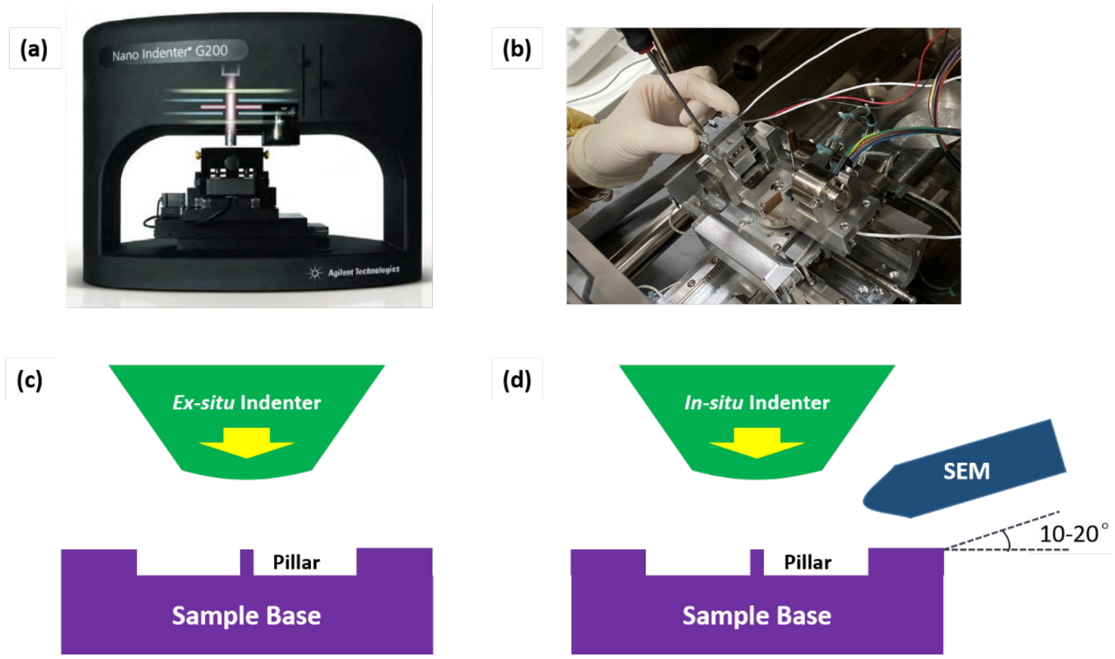

Figure 4. 13 Schematic diagrams of Nano indenter with (a) ex-situ G200, (b) in-situ NanoFlip, and relative positions of pillar and indenter tips (c) in G200 without SEM, and (d) in NanoFlip with SEM.

Before the uniaxial compression, the pillars (with a one-degree taper) were aligned according to the position of indenter, and strain rate was set to $5 \times 10^{-4}\ s^{-1}$. The stage was tilted to 15 degree. In-situ compression was applied for real-time recording during compression, and the results are presented in **Figure 4. 14**.

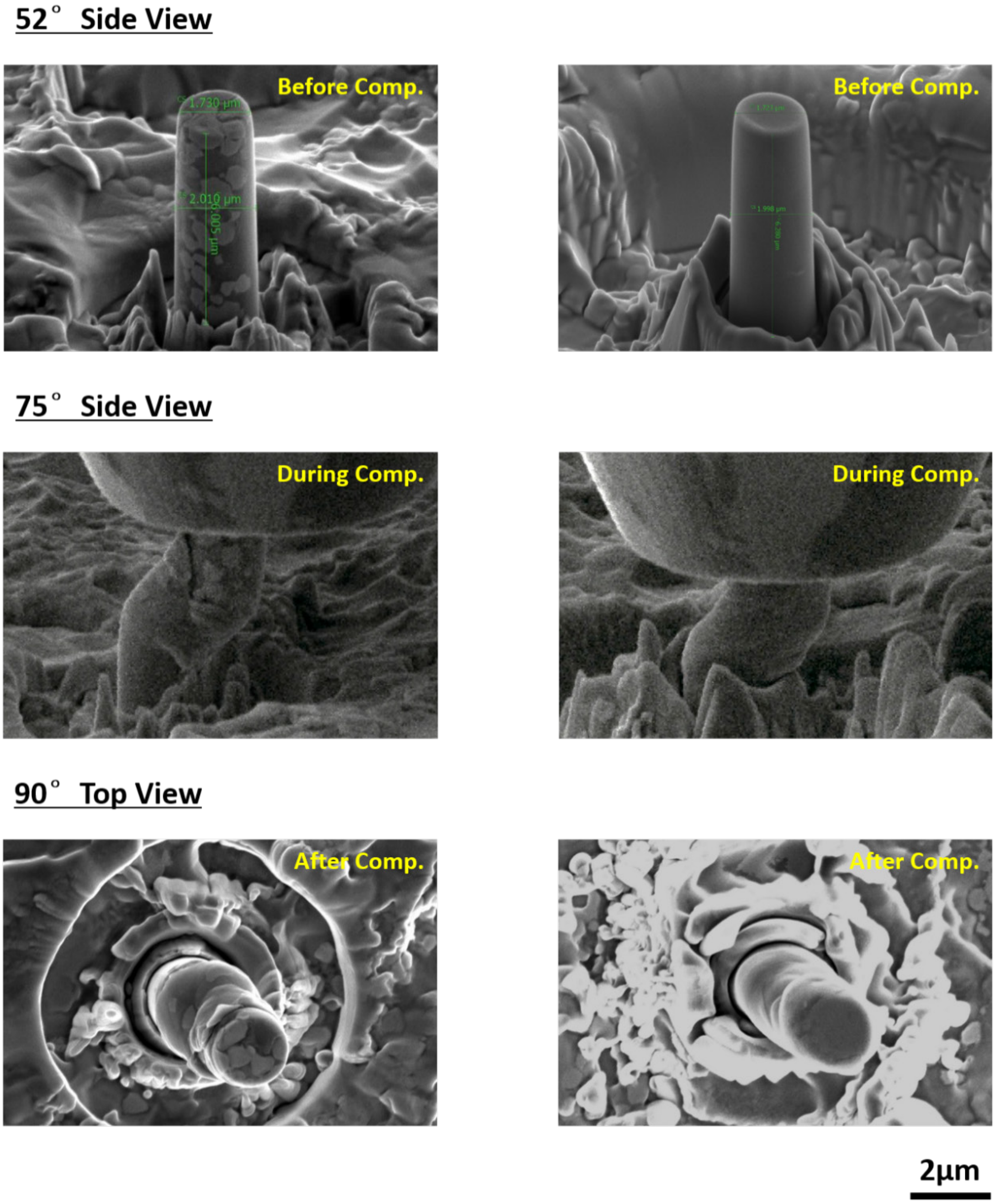

Figure 4. 14 FESEM image of in-situ compression for CZ-Al #1 (left) and CZ-Al #2 (right) in different period of time, before, during and after compression (abbr. Comp.)

with related to 52° side view, 75° side view and 90° top view, respectively.

Two pillars, marked as CZ-Al #1 (left, with rich amount of CZ inside the pillar) and CZ-Al #2 (right, with poor amount of CZ inside the pillar). From the process, CZ-Al #1 underwent the fracture, mainly because of the crack initiated from the surface where CZ single crystals covered. The mismatch between CZ single crystals and Al matrix is normally easy to cause the fracture. An interesting phenomenon happened when the slipping plane was along 30-degree plane instead of 45-degree plane as normally the maximum shear stress lays in CZ-Al #1. While CZ-Al #2 underwent the ductile fracture with obvious twinning bands.

The deformation could be combined with the stress-strain curve according to the factor of time. The pseudocode for combining real-time deformation video with stress-strain curve according to the factor of time is shown in **Table 4. 4**. The image demonstrated the pillar shape during compression was obtained in this method (**Figure 4. 14** and the whole in-situ characterization will be shown in **Appendix I.** In spite that the image is blurry due to real-time recording, it is enough for observing the fracture behavior. More accurate characterization for dislocation movement, phase transition will be detected via TEM.

Table 4. 4 Pseudocode for combining real-time deformation video with stress-strain curve according to the factor of time.

Main Program	**Function Program**
1). Read the video; 2). Combine video and curve; 3). Then, show the image.	1). Set the input parameter; 2). Synchronize the time; 3). Initialize the image from raw video; 4). Output the frame and object.

From the whole compression video and shortcut shown in **Figure 4. 15**, cracking was initiated at the place where CZ single crystals located and marked with white frame. CZ-Al #1 with rich CZ has higher yield strength (181.5MPa) than CZ-Al #2 with poor CZ (136.6MPa), while CZ-Al #2 shows large ductility to 35%, higher than CZ-Al #1 with 15%. There are lots of small burst (or stages) during the flow stress, mainly because of the movement of different slip planes, dislocation in the Al matrix as well as mismatch by different crystal orientation at the interface of CZ/Al, which will be proved via TEM.

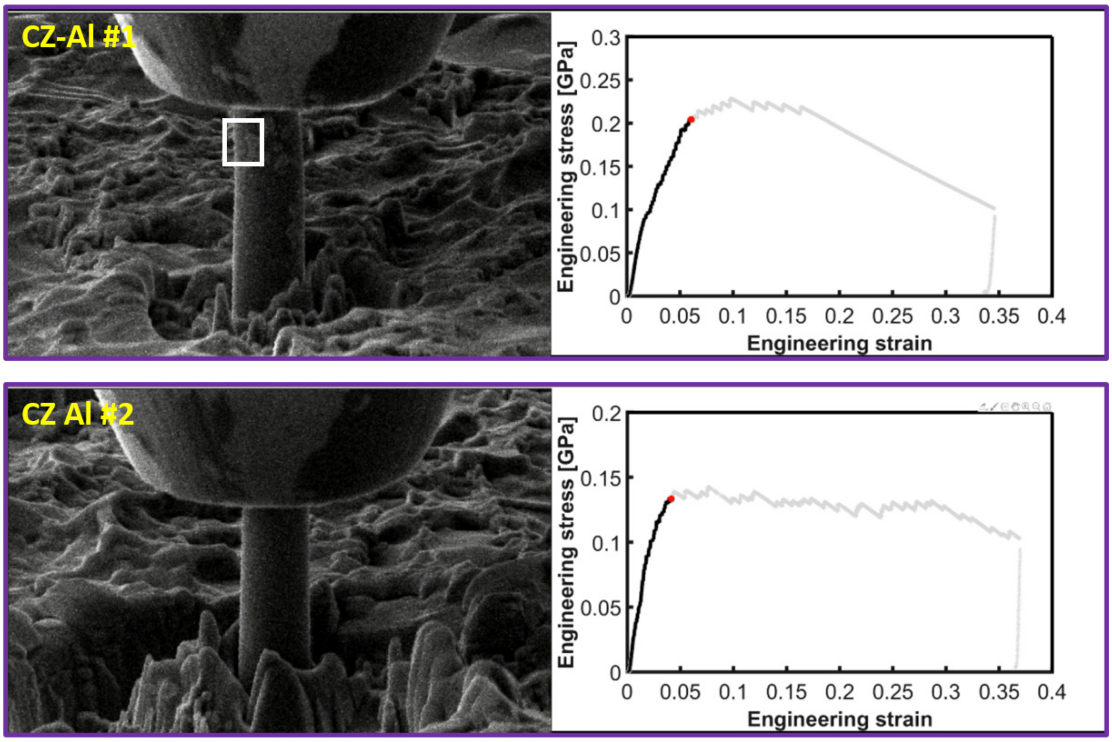

Figure 4. 15 Stress-Strain Curve of *in-situ* compression test combined with the real-time image at the time of the red spot standing by, presenting the point of yield strength of CZ Al #1, #2, respectively.

Based on the *in-situ* compression test, an ex-situ compression test via G200 was done for better analyzing. CZ-Al pillar #3 and pure Al pillar with 2 μm were compressed under the condition same as *in-situ* test (**Figure 4. 16**). Series of "burst" phenomena occurred during flow stress stage in both CZ-Al and pure Al, which could be attributed to Al slipping and the dislocation sink in Al/CZ interface [87]. CZ-Al pillar possessed with extremely higher yield strength (521.3 MPa) compared to Al pillar with only 62.6 MPa.

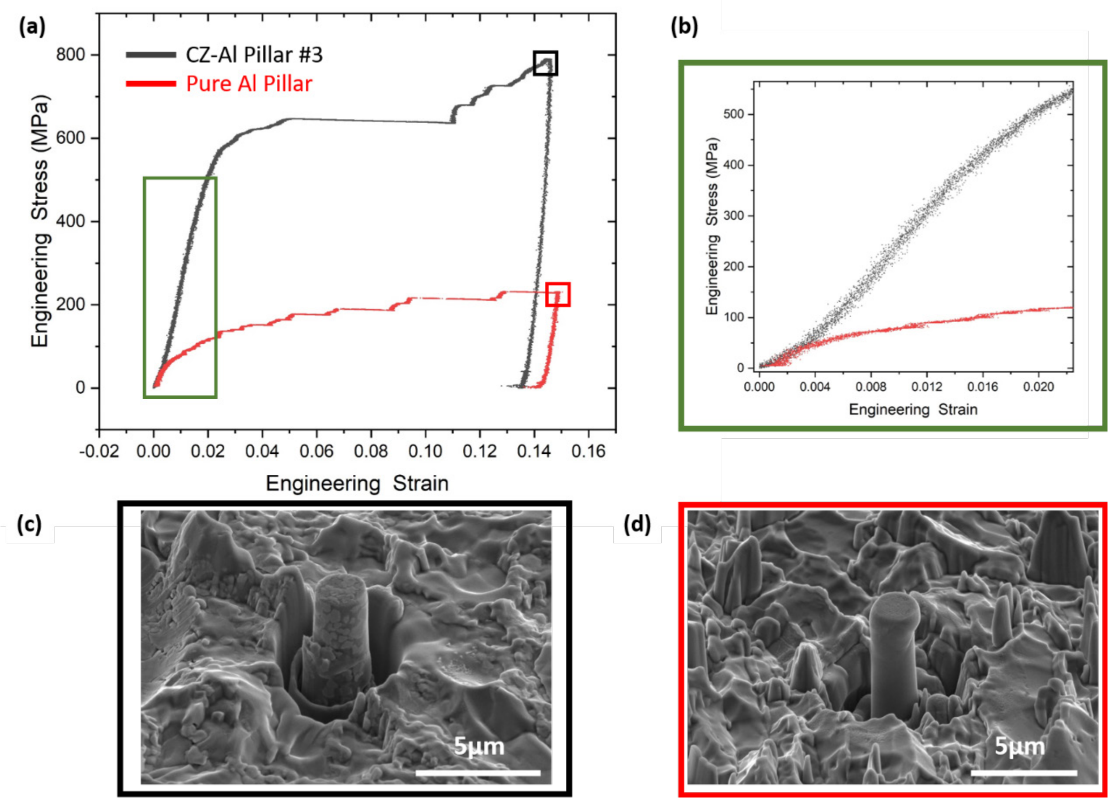

Figure 4. 16 (a) Stress-Strain Curve of *ex-situ* compression test for CZ-Al pillar #3 and pure Al pillar, and (b) the detail in green area zooming in, with FESEM image of post-compressed pillar morphology of (c) CZ-Al #3 and (d) pure Al.

Compared with the bulk sample test and *in-situ* test, the yield strength and compressive strength were differed a lot (**Table 4. 5**). Simply concerned with CZ-Al pillar #1 and #2, it shares nearly close result to bulk sample. Whilst, CZ-Al pillar #3 offers a totally different fact that size effect did affect the strengthening process. 2 μm diameter is enough for revealing the size effect. The reason for CZ-Al #1 and #2 in low strength may account from:

1. Friction induced horizontal shear stress by stage shifting;
2. CZ particles decorated on the surface initiating cracks;

3. Low CZ particles containing.

Table 4. 5 Parameters for Mechanical Test of CZ-Al bulk sample and micropillar at small volume (Unit: MPa)

Sample		σ_s	σ_{bc}
CZ	Bulk Ave	188.4	277.2
	Pillar #1	181.5	220.3
	Pillar #2	136.6	138.5
	Pillar #3	**521.3**	/
Al	Bulk Ave	32.2	86.5
	Pillar	**62.6**	/

To further explore the strengthening mechanism, Transmission Electron Microscopy (TEM, JEOL JEM-2100F) is utilized to observe the zirconia phase transformation one spot by one spot, and dislocation movement in Al matrix. A suitable TEM specimen size is required. Owing to the properties of CZ-Al composites, focus ion beam (FIB) is considered for thinning. The section thickness of bulk CZ-Al or CZ-Al pillar can be milled to several hundred nanometers via FIB (**Figure 4. 17**). CZ-Al #1 sample after compression was taken.

With the help of TEM sample, a clear microstructure can be obtained. Coated with platinum (Pt) as a protection layer, the morphology of bending pillar is shown due to the difference in contrast and marked with yellow curve in **Figure 4. 17** (b). It has to be mentioned that Pt was coated in two steps, firstly with electron beam at high beam current, secondly with ion beam at low beam current. That is how the two different Pt layers formed.

There still remains CZ in the pillar, which almost distributed along the surface of pillar. Combined with the CZ-Al structure, for CZ-Al #1, it can be inferred that there is only one or limited Al grain with the CZ single crystals decorated on the surface (**Figure 4. 17** (a)).

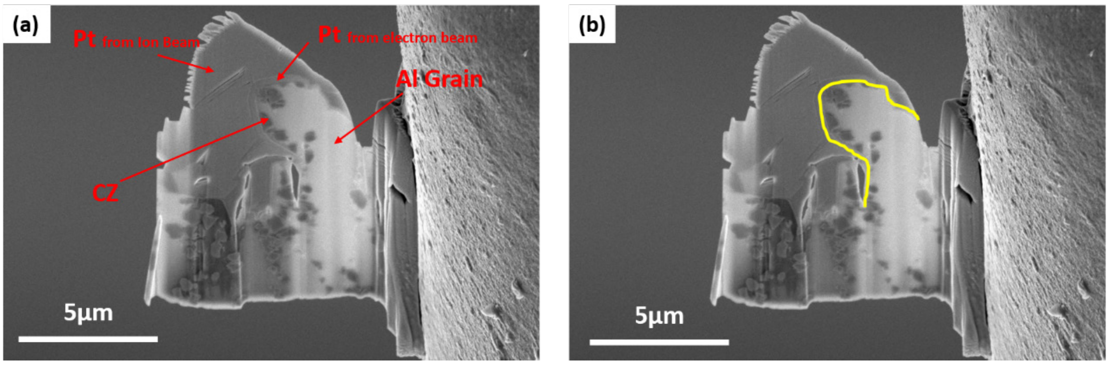

Figure 4. 17 TEM preparation of CZ-Al #1 sample after compression via FIB thinning with (a) different composition on the sample marked in red arrows, and (b) contour of pillar after compression.

Selected Area Electron Diffraction (SAED) is employed for zirconia phase identification. In the meantime, with Fourier Transformation, the SAED results could be combined with High Resolution TEM (HR-TEM). In this case, four different spots were selected, marked as Spot #1, Spot #2, Spot #3 and Spot #4. With proper Kikuchi line manipulation, clear images with light spot were obtained. With indexation, the phase of zirconia as well as the zoom axis are shown in **Figure 4. 18**. It could be inferred that zirconia at Spot #1, #2 and #4 were transformed to monoclinic phase, while no obvious transformation at Spot #3. Possible reasons for the case lie in the matrix constraint of Spot #3 is higher than others which are all near the surface of pillar, or the different orientation induced less stress on the CZ [24]. Furthermore, the martensite transformation at Spot #1,2,4 indicates a strain energy released. Based on the previous work [24], the stress conducted from Al matrix during compression triggered the martensite transformation, which induced volume expansion and strain stress, thus having CZ-Al reinforced, which is shown in **Table 4. 5**.

In fact, the ion milling during the preparation may decrease the matrix constraint on CZ single crystals (TEM specimen has a thickness around 100nm). More accurate conclusions will be conducted in CZ-Al pillar before compression via SAED. Anyway, the SAED results proved that the Al matrix constraint retained the martensite transformation ability of CZ single crystals, which offers a potential for SME in future.

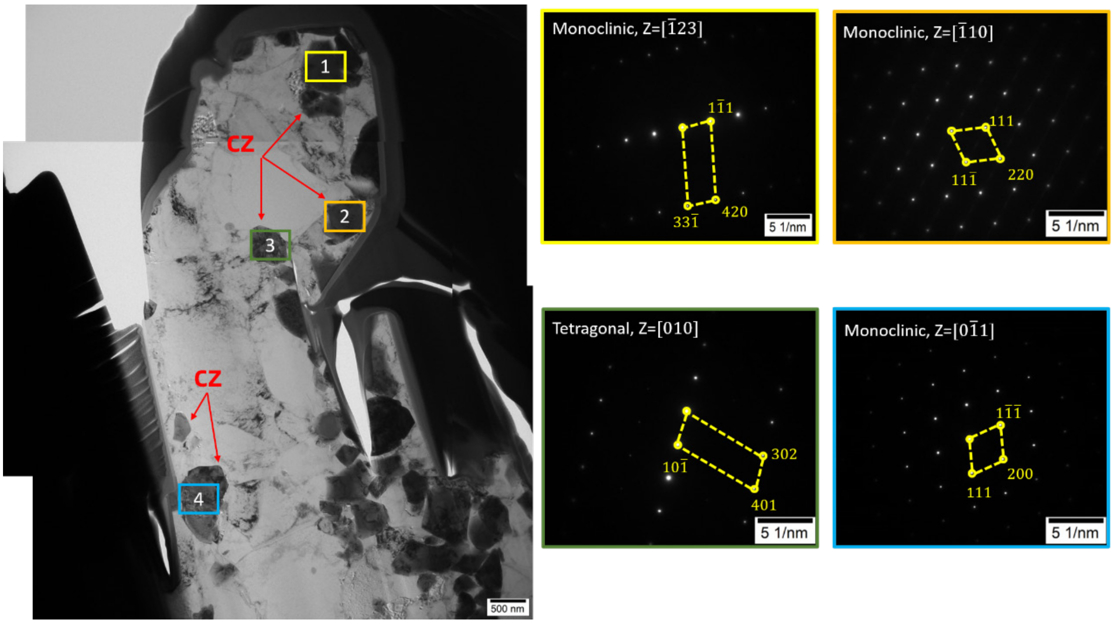

Figure 4. 18 TEM characterization of CZ-Al pillar #1 with 4 spots on CZ single crystals SAED image with yellow, orange, green and blue frame.

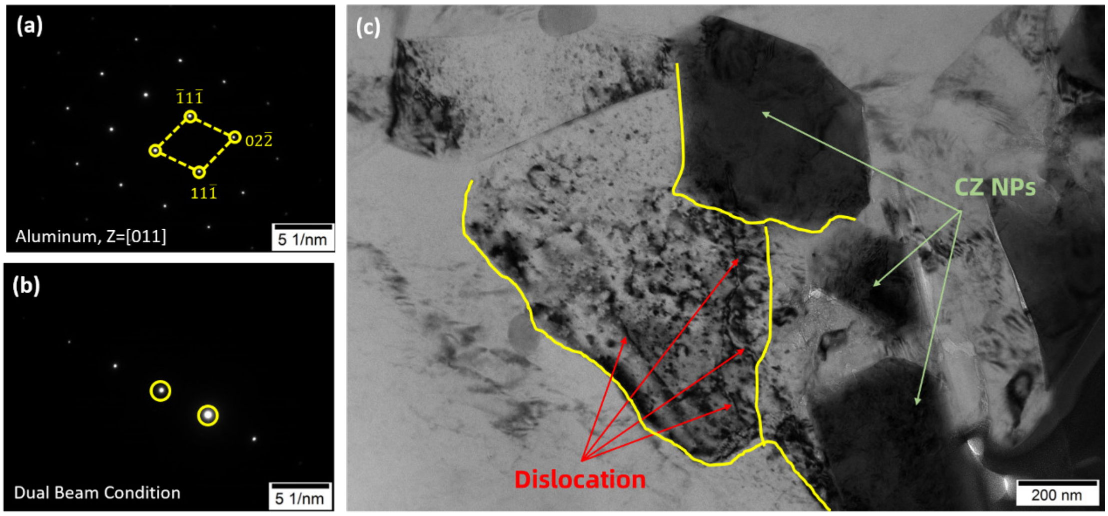

Figure 4. 19 TEM image of dislocation distributed near the Al/CZ interface under dual beam condition with Al zone axis = [011].

To estimate the matrix constraint, SAED on Al matrix with [011] zone axis was indexed. Under the condition of dual beam, a series of geometrically necessary dislocations (GND) near the Al/CZ interface micro-region were marked in **Figure 4. 19**, thus inducing obvious strain hardening of the Al matrix. Therefore, the enhancement in strength and hardness of the composite has been proved to come from the combined effect of the loading of the nanoparticles and the strain hardening of the Al matrix.

4.4 Conclusive Remarks

This chapter presented a systematic characterization method on morphology, phase composition, crystal orientation and mechanical test for bulk CZ-Al and CZ-Al micropillar at small volume. The conclusion lies on:

1. Revealing that CZ-Al has an average hardness 67.2% higher than Pure Al, and an average yield strength 159.3 MPa (486%) higher than Pure Al, with over 20% strain to fracture.
2. Explaining the mechanism of different state (martensite or tetragonal) of zirconia in several sample, i.e. pure zirconia, CZ bulk sample, CZ single crystal, CZ-Al bulk sample and micropillar, based on the energy term.
3. Stating the reinforcement of CZ single crystal in Al matrix, which accounts from stress-induced martensite transformation. It caused the volume expansion and shear stress, inducing dislocation accretion and enhance the strength of CZ-Al.
4. Stating the martensite transformation in pillar compression at microscale and understanding the fracture mechanism with small volume pillar under in-situ compression.

Chapter 5 Impact and Future Work

This chapter makes conclusion on the thesis with the foundation of hypothesis to be proven. It contains the basic horizon of Cerium doped Zirconia reinforced Aluminum Matrix Composites (CZ-Al) fabrication and characterization methodology. Future work, improvement of experimental design and opening problems are listed.

5.1 Summary and Implications

In the project, we propose that compositing or incorporating other functional materials as shape memory composites, may lead to some promising properties and behaviors as a bulk sample with shape memory effect. To prove the hypothesis, we have developed a new CZ-Al shape memory composite. A complete fabrication method was explored, including ball milling and hot-pressing densification.

A systematic characterization on CZ-Al revealed that laminated structure and basic mechanical properties. The study of stress-induced martensite transformation guides us to explore the reinforcing mechanism.

The CZ-Al micro-pillars demonstrated the mechanical behaviors comparable with the corresponding bulk sample, with the aim of exploring size effect and matrix constraint as well as strengthening mechanism.

The shape memory composites made at macro- and microscale offers a tremendous horizon for future materials development and in-depth mechanistic studies. Meanwhile, the reinforcing mechanism was revealed according to the structure-property relationship, which could also expand the application field like self-healing, energy damping, actuator and sensing.

5.1.1 Proven of hypothesis

In Chapter 1, we proposed that *with the fabrication of CZ-Al, 12 mol% CZ single crystal can be stabilized in tetragonal phase when compositing in Aluminum matrix composite*. Two parts will be carried out to prove the hypothesis, one in theoretical calculation, one in experimental characterization.

In previous work from Lai et al. [22], 14 mol% Cerium doped Zirconia single crystal is a critical content of dopant for monoclinic phase transforming to tetragonal phase.

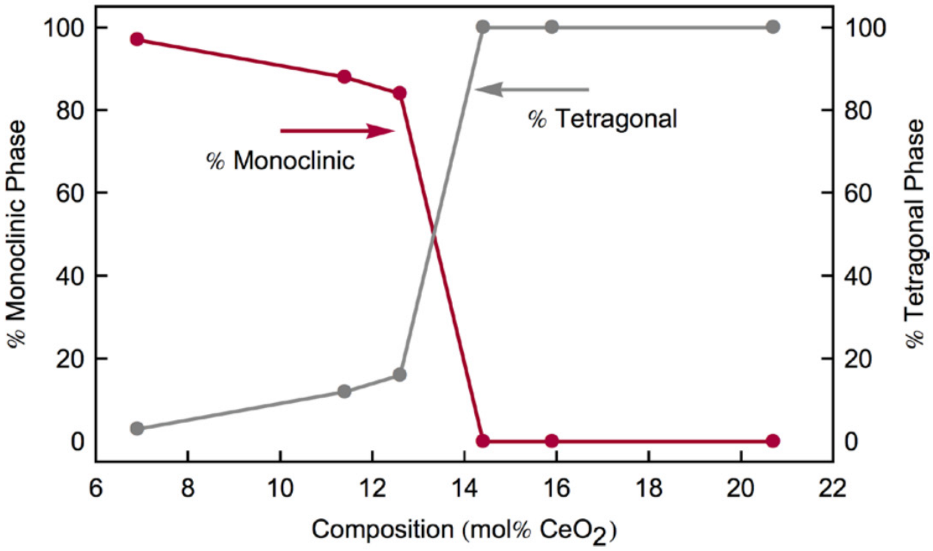

Figure 5. 1 Schematic illustration of different composition of CeO_2 related to the content of Monoclinic/Tetragonal phase in CeO_2-ZrO_2 system [22].

In our own shape memory composites system, 12 mol% CZ single crystal was incorporated in the Al matrix. Simply concerned about 12 mol% CZ single crystal, according to the dopant effect equation summarized in Chapter 2:

$$A_f = 1280.52 - 78.68C_{Ce}\ ℃ \qquad \text{Equation 13}$$

12 mol% CZ has a martensite transformation temperature (MTT) with: $A_s = 236.36℃, M_f = 28.57℃, A_f = 336.36℃$. With Al matrix constraint, the residual

stress during hot-pressing test will further increase strain energy term ΔU_e in the **Equation 3**, in this case, to make the transformation occur, transformation temperature has to be increased, which inhibits the reverse martensite transformation at room temperature, only when other factor changes, i.e. test temperature increases, will austenite form. From the perspective of energy term, the effect could be equal to the increasing composition of CeO_2, which leading to the stabilization of tetragonal phase of ZrO_2 at room temperature. The hypothesis is proven in theoretical calculation.

Experimental characterization was done via compression test at the microscale and macroscale. From XRD, EBSD, both bulk sample and micro-pillar before compression was fully retained in the tetragonal state, without reverse martensite transformation occur. Herein, based on the first hypothesis, we suppose another one to further utilize the SME in strengthening mechanism, *the stress on the CZ single crystals conducted from Al matrix deformation will induce phase transition, with which the volume is expanded and shear strain is induced to enhance the matrix and have the CZ detached.*

In fact, there might be small amount of monoclinic phase transferred into tetragonal phase during unloading. More works (e.g. synchrotron radiation X-ray diffraction) will be carried on.

5.1.2 Conclusive Implications

In this study, we prepared 12mol% cerium-doped zirconia single crystalline nanoparticles reinforced aluminum matrix composite (CZ-Al) via a powder metallurgy approach, in which the mass fraction of the particle reinforcement was 30 wt%. Electron microscopy revealed that the mechanical ball milling and subsequent high temperature densification process generated a laminated ultrafine-grained microstructure in the Al matrix, and the CZ nanoparticles were preferentially distributed on the interlayer interface of the Al matrix. The density of the CZ-Al composite was 3.22 g/cm^3 using the Archimedes method, approaching a relatively density of almost 100%. The Vickers hardness of the composite was found to be 85.1±0.2, approximately 67.2% higher than that of pure Al prepared by the same process. The compressive yield strength is 188.4±8.1 MPa, 486.0% higher than that of pure Al. Compressive fracture strain of CZ-Al and pure Al were both around 20%, while the tensile fracture strain of CZ-Al was ~150% higher than that of pure Al. Therefore, these preliminary results showed considerable strengthening-toughening effect of the CZ-Al composite.

12mol% cerium-doped zirconia single crystal (CZ) is stable in monoclinic phase at room temperature and stable in tetragonal phase at the temperature higher than austenite finish temperature of 336°C. However, it was shown by X-ray diffraction that zirconia in the prepared CZ-Al composite is in 100% tetragonal phase at room temperature, suggesting that Al matrix had a constraint on the reverse martensite transformation upon cooling from the high temperature densification. Since the martensite transformation of zirconia is accompanied by a volume change of 4-5% and a shear strain of 14-15%, such an observation indicated that there must be a large number of geometrically necessary dislocations (GNDs) and residuals stress (strain) around the CZ nanoparticles, thus inducing obvious strain hardening of the Al matrix near the interface micro-region. Therefore, the enhancement in strength and hardness of the composite compared to pure Al may come from the combined effect of the load-sharing of the nanoparticles and the strain hardening of the Al matrix.

The preparation of CZ-Al micropillars with a diameter of ~ 2 μm further presented that compressive yield strength was 521.21MPa, 710% higher than that of pure Al pillar. Transmission electron microscopic (TEM) analysis on post-compression CZ-Al pillars revealed that zirconia phase in most of CZ particles were transformed from tetragonal phase into monoclinic phase. The presence of abundant GNDs near the particle/matrix interface, and the dislocation density generally decreased away from the interface, proved the strengthening mechanism of CZ nanoparticles proposed above.

In summary, zirconia ceramic particles reinforced Al-based composites were prepared and their microstructure and mechanical behavior were characterized. It is shown that the composite material had an obvious mechanical property enhancement effect compared with the pure Al matrix fabricated by the same process. Further work will focus on further optimization of the fabrication process, as well as further detailed interpretation of the interface properties and deformation mechanism of the composite.

5.2 Future Work

Reviewing the whole project to date, we have focused more on stress-induced martensite transformation (SIMT), which has a deep learning in sample state at room temperature, while in some cases, limits our analysis of the whole process. Moreover, modeling of SMc will be carried out to estimate the stress on CZ applied by Al matrix during transformation, which may provide guidance to the suitable weight ratio of Al and CZ in the SMc. Considering the distribution of CZ in Al matrix, other fabrication methods will be designed for a controllable CZ-Al structure in future.

5.2.1 Thermo-induced Martensite Transformation

Otsuka *et al.* [88] reported that thermodynamic martensite transformation is controlled by several factors, where stress and temperature are normally the distinguished external factors, which divided the diagram (shown in **Figure 5. 2**) into different functional area. There is a critical stress for slip at different temperature owing to activation energy, and a critical stress to induce martensite transformation when temperature is higher than Ms. Shape Memory Effect and Superelasticity (or Pseudoelasticity) are differentiated by As (austenite start temperature), featured with SME below As and SE above As.

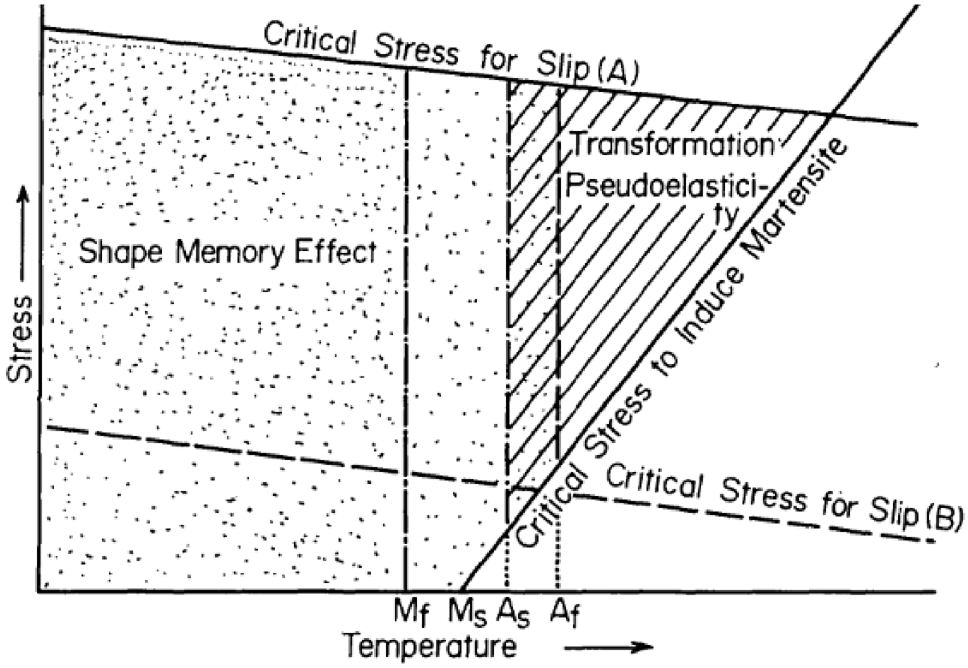

Figure 5. 2 Schematic diagram of thermodynamic martensite transformation controlled by stress and time, which divided the diagram into Shape Memory Effect and Superelasticity [88].

In our studies about the SIMT, CZ-Al bulk sample or pillar was compressed at room temperature, where shape memory effect dominates. More researches will be conducted at elevated temperatures, with the purpose of inducing the shape recovery of CZ single crystal as well as cyclic stress to obtain superelasticity.

5.2.2 Modeling for CZ-Al composites

Basic modeling has contributed to analysis of structure and composite distribution. As to CZ-Al system aforementioned, Al matrix always tends to deform first, then pass through a stress with certain crystal orientation. Supposing the post-compressed CZ-Al pillar or bulk sample is heated, the CZ single crystals will recover first, while brings about a residual stress induced by coefficient of thermal expansion (CTE) and have effect on Al matrix. The whole process could be treated as a cyclic relaxation system, with a transformation time lag. Whereas, it is still difficult to estimate the real stress on CZ conducted from Al matrix during transformation. Moreover, to guide the suitable weight ratio of Al and CZ in the SMc and figure out the critical transition temperature and stress under different condition, it is essential to establish a modeling procedure for CZ-Al system.

Finite element analysis (FEA) is outstanding among the numerical simulation due to the suitable size and easy for parameter setting [89]. Lots of works have explored different case in particle reinforced metal matrix composites (PMMC) about the stress distribution [89-91], which is similar to the case of CZ-Al.

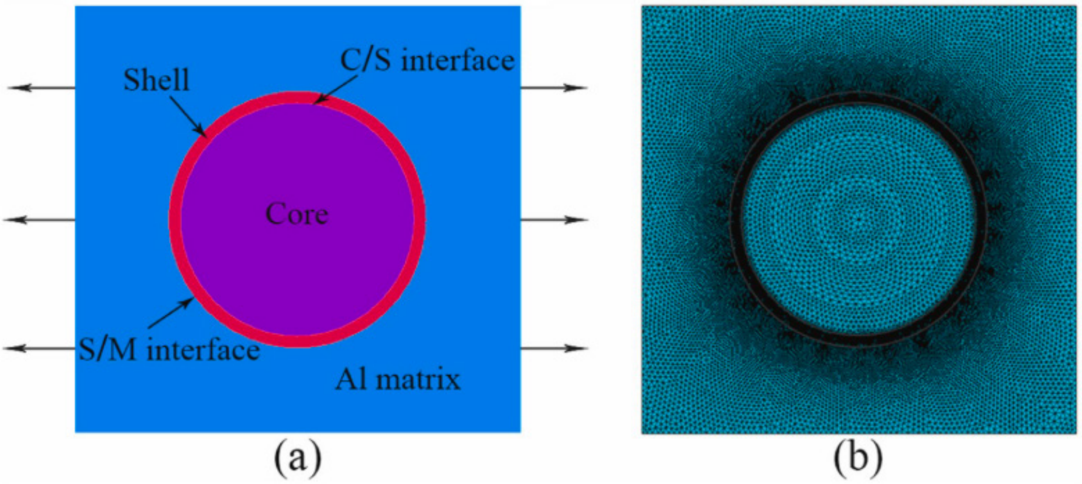

Figure 5. 3 Schematic illustration of core-shell structure modelling via FEA [89].

Based on the previous work, a simple system is shown to explain the approach and the goal of modeling in CZ-Al system (**Figure 5. 4**). With modelling method, the experimental design will move to a more reasonable manner.

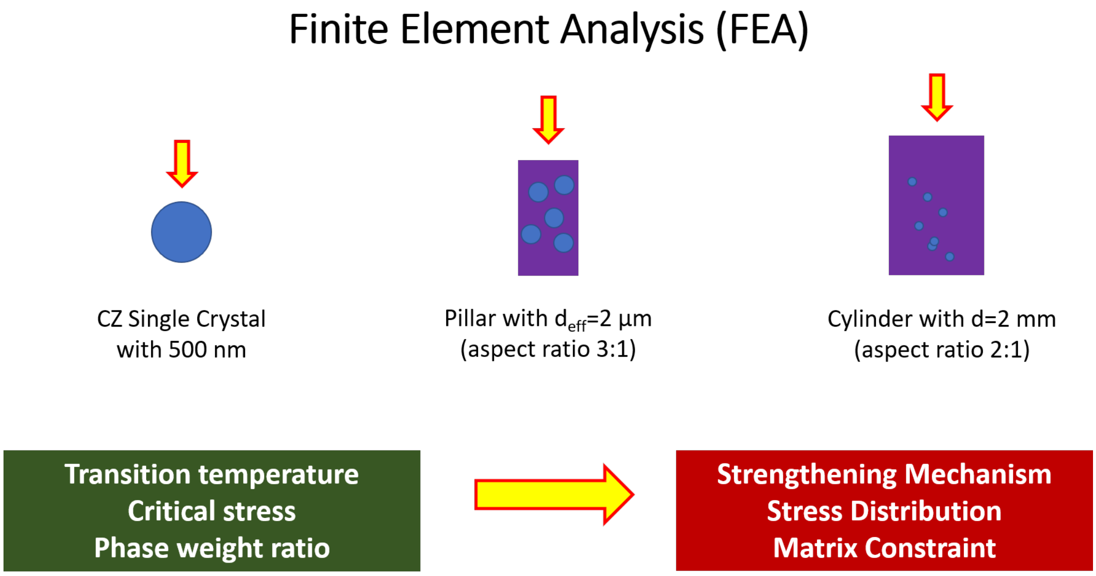

Figure 5. 4 Finite element method applied in modeling CZ-Al system and the input-output data.

5.2.3 Improvement of Fabrication Method

Concerned with CZ-Al, it is hard to maintain the ZrO_2/Al microstructure with good dispersion and distribution via ball milling and hot-pressing fabrication method. In case of the previous work, 12mol% cerium doped zirconia (CZ) particles are randomly decorated along the Al grain boundary, mainly because of the pre-set location.

In future, new fabrication method will be explored, to achieve the controllable processing. With good dispersive structure and CZ single crystals inside the Al grain if possible, mechanical properties and SME are expected to be enhanced.

Aghajanian *et al.* [92] reported a Al matrix composites with several fillers, i.e. particles, agglomerates, and fibres via pressureless infiltration method. A strong bond between metal and ceramic was formed due to the enhanced wetting provided, which exhibits favorable structural properties, i.e. high stiffness and low CTE. Based on the previous work, a simply Schematic illustration of CZ-Al fabrication method with infiltration is shown in **Figure 5. 5**. The CZ single crystals are set into a container to form a pre-form, followed by pouring in melted Al bulk sample and then hot pressing.

With a suitable parameter and protocol optimization, a controllable system could be obtained, as well as advanced structure-properties relationship.

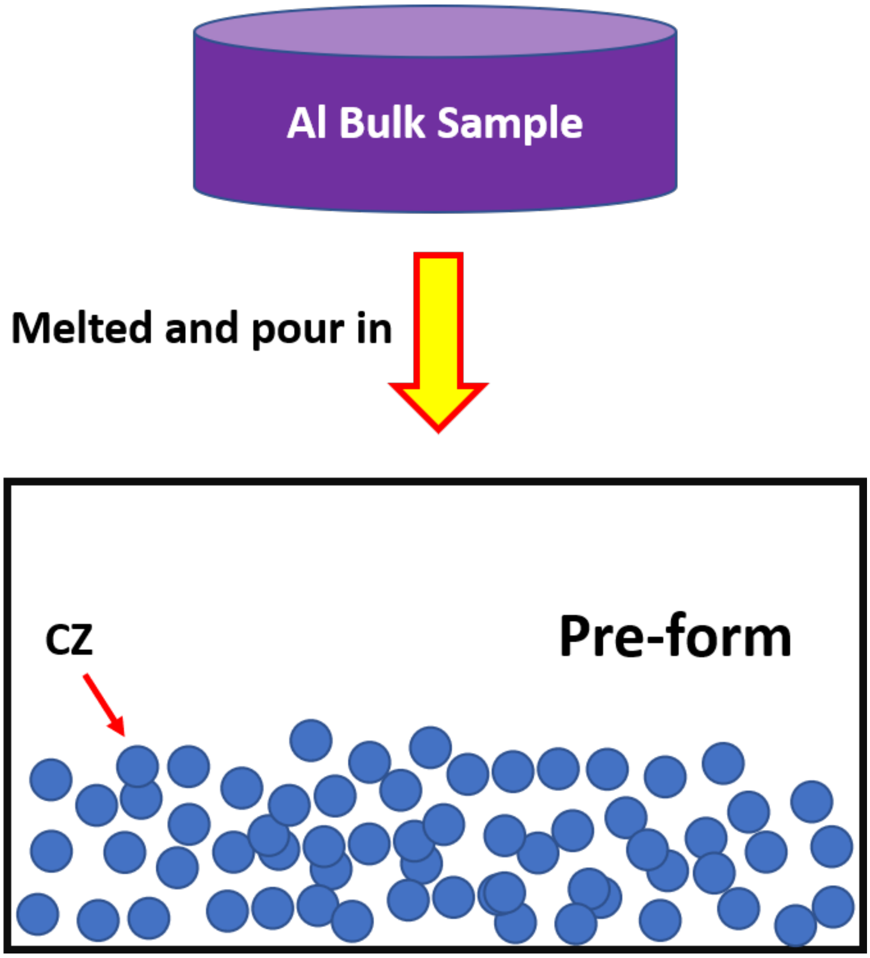

Figure 5. 5 Schematic illustration of CZ-Al fabrication method with infiltration.

REFERENCE

[1] SUN L, HUANG W M, DING Z, et al. Stimulus-responsive shape memory materials: A review [J]. Materials & Design, 2012, 33(577-640. https://doi.org/10.1016/j.matdes.2011.04.065.

[2] ROY D, CAMBRE J N, SUMERLIN B S. Future perspectives and recent advances in stimuli-responsive materials [J]. Progress in Polymer Science, 2010, 35(1-2): 278-301. https://doi.org/10.1016/j.progpolymsci.2009.10.008.

[3] JANI J M, LEARY M, SUBIC A, et al. A review of shape memory alloy research, applications and opportunities [J]. Materials & Design, 2014, 56(1078-113. https://doi.org/10.1016/j.matdes.2013.11.084.

[4] NESPOLI A, RIGAMONTI D, VILLA E, et al. Design, characterization and perspectives of shape memory alloy elements in miniature sensor proof of concept [J]. Sensors and Actuators a-Physical, 2014, 218(142-53. https://doi.org/10.1016/j.sna.2014.08.001.

[5] LENDLEIN A, KELCH S. Shape - memory polymers [J]. Angewandte Chemie International Edition, 2002, 41(12): 2034-57. https://doi.org/10.1002/1521-3773(20020617)41:123.0.CO;2-M.

[6] LIU C, QIN H, MATHER P T. Review of progress in shape-memory polymers [J]. Journal of Materials Chemistry, 2007, 17(16): 1543-58. https://doi.org/10.1039/b615954k.

[7] SWAIN M V. Shape memory behaviour in partially stabilized zirconia ceramics [J]. Nature, 1986, 322(6076): 234-6. https://doi.org/10.1038/322234a0.

[8] LOWENBERG C, BALK M, WISCHKE C, et al. Shape-Memory Hydrogels: Evolution of Structural Principles To Enable Shape Switching of Hydrophilic Polymer Networks [J]. Acc Chem Res, 2017, 50(4): 723-32. https://doi.org/10.1021/acs.accounts.6b00584.

[9] WEI Z G, SANDSTROM R, MIYAZAKI S. Shape memory materials and hybrid composites for smart systems - Part II Shape-memory hybrid composites [J]. Journal of Materials Science, 1998, 33(15): 3763-83. https://doi.org/10.1023/A:1004674630156.

[10] JAMES R D, HANE K F. Martensitic transformations and shape-memory

materials [J]. Acta Materialia, 2000, 48(1): 197-222. https://doi.org/10.1016/S1359-6454(99)00295-5.

[11] OTSUKA K, REN X. Physical metallurgy of Ti-Ni-based shape memory alloys [J]. Progress in Materials Science, 2005, 50(5): 511-678. https://doi.org/10.1016/j.pmatsci.2004.10.001.

[12] VAN HUMBEECK J. Shape memory alloys: a material and a technology [J]. Advanced engineering materials, 2001, 3(11): 837-50. https://doi.org/10.1002/1527-2648(200111)3:113.0.CO;2-0.

[13] ZENG X M, DU Z H, SCHUH C A, et al. Enhanced shape memory and superelasticity in small-volume ceramics: a perspective on the controlling factors [J]. Mrs Communications, 2017, 7(4): 747-54. https://doi.org/10.1557/mrc.2017.99.

[14] LUO X F, MATHER P T. Preparation and Characterization of Shape Memory Elastomeric Composites [J]. Macromolecules, 2009, 42(19): 7251-3. https://doi.org/10.1021/ma9015888.

[15] YOSHIDA H, MATSUI K, IKUHARA Y. Low-Temperature Superplasticity in Nanocrystalline Tetragonal Zirconia Polycrystal (TZP) [J]. Journal of the American Ceramic Society, 2012, 95(5): 1701-8. https://doi.org/10.1111/j.1551-2916.2012.05150.x.

[16] CRYSTAL I R, LAI A, SCHUH C A. Cyclic martensitic transformations and damage evolution in shape memory zirconia: Single crystals vs polycrystals [J]. Journal of the American Ceramic Society, 2020, https://doi.org/10.1111/jace.17117.

[17] SAN JUAN J, Nó M L, SCHUH C A. Superelasticity and Shape Memory in Micro- and Nanometer-scale Pillars [J]. Advanced Materials, 2008, 20(2): 272-8. https://doi.org/10.1002/adma.200701527.

[18] SAN JUAN J, NO M L, SCHUH C A. Nanoscale shape-memory alloys for ultrahigh mechanical damping [J]. Nat Nanotechnol, 2009, 4(7): 415-9. https://doi.org/10.1038/nnano.2009.142.

[19] YE J, MISHRA R K, PELTON A R, et al. Direct observation of the NiTi martensitic phase transformation in nanoscale volumes [J]. Acta Materialia, 2010, 58(2): 490-8. https://doi.org/10.1016/j.actamat.2009.09.027.

[20] ZHANG H S, KOMVOPOULOS K. Nanoscale pseudoelasticity of single-crystal Cu-Al-Ni shape-memory alloy induced by cyclic nanoindentation [J]. Journal of Materials Science, 2006, 41(15): 5021-4.

https://doi.org/10.1007/s10853-006-0124-6.

[21] YU Q, SHAN Z W, LI J, et al. Strong crystal size effect on deformation twinning [J]. Nature, 2010, 463(7279): 335-8. https://doi.org/10.1038/nature08692.

[22] LAI A, DU Z, GAN C L, et al. Shape memory and superelastic ceramics at small scales [J]. Science, 2013, 341(6153): 1505-8. https://doi.org/10.1126/science.1239745.

[23] DU Z H, ZENG X M, LIU Q, et al. Size effects and shape memory properties in ZrO2 ceramic micro- and nano-pillars [J]. Scripta Materialia, 2015, 101(40-3. https://doi.org/10.1016/j.scriptamat.2015.01.013.

[24] ZENG X M, LAI A, GAN C L, et al. Crystal orientation dependence of the stress-induced martensitic transformation in zirconia-based shape memory ceramics [J]. Acta Materialia, 2016, 116(124-35. https://doi.org/10.1016/j.actamat.2016.06.030.

[25] ZENG X M, DU Z H, TAMURA N, et al. In-situ studies on martensitic transformation and high-temperature shape memory in small volume zirconia [J]. Acta Materialia, 2017, 134(257-66. https://doi.org/10.1016/j.actamat.2017.06.006.

[26] DU Z H, ZENG X M, LIU Q, et al. Superelasticity in micro-scale shape memory ceramic particles [J]. Acta Materialia, 2017, 123(255-63. https://doi.org/10.1016/j.actamat.2016.10.047.

[27] ZHANG N, ZAEEM M A. Nanoscale self-healing mechanisms in shape memory ceramics [J]. Npj Computational Materials, 2019, 5(1): 54. https://doi.org/10.1038/s41524-019-0194-z.

[28] YANG H, LEOW W R, WANG T, et al. 3D Printed Photoresponsive Devices Based on Shape Memory Composites [J]. Adv Mater, 2017, 29(33): 1701627. https://doi.org/10.1002/adma.201701627.

[29] LU Z K, WENG G J. Martensitic transformation and stress-strain relations of shape-memory alloys [J]. Journal of the Mechanics and Physics of Solids, 1997, 45(11-12): 1905-&. https://doi.org/10.1016/S0022-5096(97)00022-7.

[30] LENG J S, LAN X, LIU Y J, et al. Shape-memory polymers and their composites: Stimulus methods and applications [J]. Progress in Materials Science, 2011, 56(7): 1077-135. https://doi.org/10.1016/j.pmatsci.2011.03.001.

[31] HUANG W M, DING Z, WANG C C, et al. Shape memory materials [J]. Materials Today, 2010, 13(7-8): 54-61. https://doi.org/10.1016/S1369-

7021(10)70128-0.

[32] KRULEVITCH P, LEE A P, RAMSEY P B, et al. Thin film shape memory alloy microactuators [J]. Journal of Microelectromechanical Systems, 1996, 5(4): 270-82. https://doi.org/10.1109/84.546407.

[33] JACQUES P J. Phase transformations in transformation induced plasticity (TRIP)-assisted multiphase steels [M]. Phase Transformations in Steels. Elsevier. 2012: 213-46.

[34] RüHLE M, EVANS A G. High toughness ceramics and ceramic composites [J]. Progress in Materials Science, 1989, 33(2): 85-167. https://doi.org/10.1016/0079-6425(89)90005-4.

[35] HEUER A H, RUHLE M, MARSHALL D B. On the Thermoelastic Martensitic Transformation in Tetragonal Zirconia [J]. Journal of the American Ceramic Society, 1990, 73(4): 1084-93. https://doi.org/10.1111/j.1151-2916.1990.tb05161.x.

[36] HANNINK R H J, KELLY P M, MUDDLE B C. Transformation toughening in zirconia-containing ceramics [J]. Journal of the American Ceramic Society, 2000, 83(3): 461-87. https://doi.org/10.1111/j.1151-2916.2000.tb01221.x.

[37] LAUNEY M E, RITCHIE R O. On the Fracture Toughness of Advanced Materials [J]. Advanced Materials, 2009, 21(20): 2103-10. https://doi.org/10.1002/adma.200803322.

[38] CHEN I W, MOREL P R. Implications of Transformation Plasticity in ZrO2 - Containing Ceramics: I, Shear and Dilatation Effects [J]. Journal of the American Ceramic Society, 1986, 69(3): 181-9. https://doi.org/10.1111/j.1151-2916.1986.tb07403.x.

[39] EVANS A G. Perspective on the Development of High-Toughness Ceramics [J]. Journal of the American Ceramic Society, 1990, 73(2): 187-206. https://doi.org/10.1111/j.1151-2916.1990.tb06493.x.

[40] KELLY P M, ROSE L R F. The martensitic transformation in ceramics - its role in transformation toughening [J]. Progress in Materials Science, 2002, 47(5): 463-557. https://doi.org/10.1016/S0079-6425(00)00005-0.

[41] REYES-MOREL P E, CHERNG J-S, CHEN I W. Transformation Plasticity of CeO2-Stabilized Tetragonal Zirconia Polycrystals: II, Pseudoelasticity and Shape Memory Effect [J]. Journal of the American Ceramic Society, 1988, 71(8): 648-57. https://doi.org/10.1111/j.1151-2916.1988.tb06383.x.

[42] 徐祖耀，金学军，张玉龙．一种形状记忆陶瓷及其制备方法：China, CN1453242A [P/OL]. 2003-. https://patents.google.com/patent/CN1453242A/zh.

[43] MICHLER J, WASMER K, MEIER S, et al. Plastic deformation of gallium arsenide micropillars under uniaxial compression at room temperature [J]. Applied Physics Letters, 2007, 90(4): 043123. https://doi.org/10.1063/1.2432277.

[44] ÖSTLUND F, RZEPIEJEWSKA‐MALYSKA K, LEIFER K, et al. Brittle‐to‐ductile transition in uniaxial compression of silicon pillars at room temperature [J]. Advanced Functional Materials, 2009, 19(15): 2439-44. https://doi.org/10.1002/adfm.200900418.

[45] SCHWIEDRZIK J, RAGHAVAN R, BURKI A, et al. In situ micropillar compression reveals superior strength and ductility but an absence of damage in lamellar bone [J]. Nat Mater, 2014, 13(7): 740-7. https://doi.org/10.1038/nmat3959.

[46] ZENG X M, DU Z H, SCHUH C A, et al. Microstructure, crystallization and shape memory behavior of titania and yttria co-doped zirconia [J]. Journal of the European Ceramic Society, 2016, 36(5): 1277-83. https://doi.org/10.1016/j.jeurceramsoc.2015.11.042.

[47] JETTER J, GU H L, ZHANG H L, et al. Tuning crystallographic compatibility to enhance shape memory in ceramics [J]. Physical Review Materials, 2019, 3(9): 093603. https://doi.org/10.1103/PhysRevMaterials.3.093603.

[48] PANG E L, MCCANDLER C A, SCHUH C A. Reduced cracking in polycrystalline ZrO2-CeO2 shape-memory ceramics by meeting the cofactor conditions [J]. Acta Materialia, 2019, 177(230-9. https://doi.org/10.1016/j.actamat.2019.07.028.

[49] RAUCH H A, CHEN Y, AN K, et al. In situ investigation of stress-induced martensitic transformation in granular shape memory ceramic packings [J]. Acta Materialia, 2019, 168(362-75. https://doi.org/10.1016/j.actamat.2019.02.028.

[50] BAI Y, HAN E-H, TAN R-B. Research on properties of aluminum matrix composites [J]. MATERIALS PROTECTION-WUHAN-, 2003, 36(9): 5-7. https://doi.org/CNKI:SUN:CLBH.0.2003-09-002.

[51] TORRALBA J M, DA COSTA C E, VELASCO F. P/M aluminum matrix composites: an overview [J]. Journal of Materials Processing Technology, 2003, 133(1-2): 203-6. https://doi.org/10.1016/S0924-0136(02)00234-0.

[52] LEE S H, SAITO Y, SAKAI T, et al. Microstructures and mechanical properties of 6061 aluminum alloy processed by accumulative roll-bonding [J]. Materials Science and Engineering a-Structural Materials Properties Microstructure and Processing, 2002, 325(1-2): 228-35. https://doi.org/10.1016/S0921-5093(01)01416-2.

[53] FURUYA Y, SASAKI A, TAYA M. Enhanced Mechanical Properties of TiNi Shape Memory Fiber/Al Matrix Composite [J]. Materials Transactions, JIM, 1993, 34(3): 224-7. https://doi.org/10.2320/matertrans1989.34.224.

[54] YAMADA Y, TAYA M, WATANABE R. Strengthening of Metal Matrix Composite by Shape Memory Effect [J]. Materials Transactions, JIM, 1993, 34(3): 254-60. https://doi.org/10.2320/matertrans1989.34.254.

[55] YANG D Z. Shape memory alloy and smart hybrid composites - advanced materials for the 21st Century [J]. Materials & Design, 2000, 21(6): 503-5. https://doi.org/10.1016/S0261-3069(00)00008-X.

[56] MIZUUCHI K, YAMAUCHI K, HAMADA K, et al. Processing of a TiPd-SMA fiber Ti matrix composite and its microstructure and mechanical properties [J]. Journal of the Japan Institute of Metals, 1997, 61(8): 727-35. https://doi.org/DOI 10.2320/jinstmet1952.61.8_727.

[57] PORTER G A, LIAW P K, TIEGS T N, et al. Fatigue and fracture behavior of nickel-titanium shape-memory alloy reinforced aluminum composites [J]. Materials Science and Engineering a-Structural Materials Properties Microstructure and Processing, 2001, 314(1-2): 186-93. https://doi.org/10.1016/S0921-5093(00)01915-8.

[58] SAN JUAN J, Nó M L, SCHUH C A. Thermo-Mechanical behavior at Nano-Scale and Size Effects in Shape Memory Alloys [J]. MRS Proceedings, 2011, 1297(19): 2461-9. https://doi.org/10.1557/opl.2011.597.

[59] SCOTT H G. Phase relationships in the zirconia-yttria system [J]. Journal of Materials Science, 1975, 10(9): 1527-35. https://doi.org/10.1007/bf01031853.

[60] SCOTT H G. Phase relationships in the yttria-rich part of the yttria-zirconia system [J]. Journal of Materials Science, 1977, 12(2): 311-6. https://doi.org/10.1007/bf00566272.

[61] PORTER D, HEUER A. Microstructural Development in MgO ‐ Partially Stabilized Zirconia (Mg ‐ PSZ) [J]. Journal of the American Ceramic Society, 1979, 62(5 ‐ 6): 298-305. https://doi.org/10.1111/j.1151-2916.1979.tb09484.x.

[62] TSUKUMA K, SHIMADA M. Strength, fracture toughness and Vickers

hardness of CeO 2-stabilized tetragonal ZrO 2 polycrystals (Ce-TZP) [J]. Journal of materials science, 1985, 20(4): 1178-84. https://doi.org/10.1007/bf01026311.

[63] YASHIMA M, MORIMOTO K, ISHIZAWA N, et al. Diffusionless Tetragonal-Cubic Transformation Temperature in Zirconia-Ceria Solid Solutions [J]. Journal of the American Ceramic Society, 1993, 76(11): 2865-8. https://doi.org/10.1111/j.1151-2916.1993.tb04028.x.

[64] CALDERON-MORENO J M, YOSHIMURA M. Characterization by Raman spectroscopy of solid solutions in the yttria-rich side of the zirconia-yttria system [J]. Solid State Ionics, 2002, 154(125-33. https://doi.org/10.1016/S0167-2738(02)00473-3.

[65] SURESH A, MAYO M J, PORTER W D. Thermodynamics of the tetragonal-to-monoclinic phase transformation in fine and nanocrystalline yttria-stabilized zirconia powders [J]. Journal of Materials Research, 2003, 18(12): 2912-21. https://doi.org/10.1557/Jmr.2003.0406.

[66] ZHANG N, ZAEEM M A. Competing mechanisms between dislocation and phase transformation in plastic deformation of single crystalline yttria-stabilized tetragonal zirconia nanopillars [J]. Acta Materialia, 2016, 120(337-47. https://doi.org/10.1016/j.actamat.2016.08.075.

[67] CHAWLA N, SHEN Y L. Mechanical behavior of particle reinforced metal matrix composites [J]. Advanced Engineering Materials, 2001, 3(6): 357-70. https://doi.org/10.1002/1527-2648(200106)3:6<357::Aid-Adem357>3.0.Co;2-I.

[68] BECHER P F, SWAIN M V. Grain-Size-Dependent Transformation Behavior in Polycrystalline Tetragonal Zirconia [J]. Journal of the American Ceramic Society, 1992, 75(3): 493-502. https://doi.org/10.1111/j.1151-2916.1992.tb07832.x.

[69] HORIKAWA H, ICHINOSE S, MORII K, et al. Orientation dependence of β 1 → β 1′ stress-induced martensitic transformation in a Cu-AI-Ni alloy [J]. Metallurgical Transactions A, 1988, 19(4): 915-23. https://doi.org/10.1007/bf02628376.

[70] YAN L, LIU Y. Wear Behavior of Austenitic NiTi Shape Memory Alloy [J]. Shape Memory and Superelasticity, 2015, 1(1): 58-68. https://doi.org/10.1007/s40830-015-0008-1.

[71] BANERJEE S, MUKHOPADHYAY P. Phase transformations: examples from titanium and zirconium alloys [M]. Elsevier, 2010.

[72] FABRIS S, PAXTON A T, FINNIS M W. A stabilization mechanism of zirconia based on oxygen vacancies only [J]. Acta Materialia, 2002, 50(20): 5171-8. https://doi.org/10.1016/S1359-6454(02)00385-3.

[73] LI P, CHEN I W, PENNER-HAHN J E. Effect of Dopants on Zirconia Stabilization-An X-ray Absorption Study: III, Charge-Compensating Dopants [J]. Journal of the American Ceramic Society, 1994, 77(5): 1289-95. https://doi.org/10.1111/j.1151-2916.1994.tb05404.x.

[74] TSOI K A, STALMANS R, SCHROOTEN J. Transformational behaviour of constrained shape memory alloys [J]. Acta Materialia, 2002, 50(14): 3535-44. https://doi.org/10.1016/S1359-6454(02)00145-3.

[75] CHEN X, SONG Y T, TAMURA N, et al. Determination of the stretch tensor for structural transformations [J]. Journal of the Mechanics and Physics of Solids, 2016, 93(34-43. https://doi.org/10.1016/j.jmps.2016.02.009.

[76] CHRASKA T, KING A H, BERNDT C C. On the size-dependent phase transformation in nanoparticulate zirconia [J]. Materials Science and Engineering a-Structural Materials Properties Microstructure and Processing, 2000, 286(1): 169-78. https://doi.org/10.1016/S0921-5093(00)00625-0.

[77] GARVIE R C. The Occurrence of Metastable Tetragonal Zirconia as a Crystallite Size Effect [J]. The Journal of Physical Chemistry, 1965, 69(4): 1238-43. https://doi.org/10.1021/j100888a024.

[78] YEH T H, KUSUMA G E, SURESH M B, et al. Effect of sintering process on the microstructures of Bi2O3-doped yttria stabilized zirconia [J]. Materials Research Bulletin, 2010, 45(3): 318-23. https://doi.org/10.1016/j.materresbull.2009.12.014.

[79] ROCHA C, NETO R L, GONçALVES V S, et al. An investigation of the use of stearic acid as a process control agent in high energy ball milling of Nb-Al and Ni-Al powder mixtures; proceedings of the Materials science forum, F, 2003 [C]. Transtec Publications; 1999.

[80] KLEINER S, BERTOCCO F, KHALID F A, et al. Decomposition of process control agent during mechanical milling and its influence on displacement reactions in the Al-TiO2 system [J]. Materials Chemistry and Physics, 2005, 89(2-3): 362-6. https://doi.org/10.1016/j.matchemphys.2004.09.014.

[81] ADACHI T, ARAKI W, HIGUCHI M. Mixture law including particle-size effect on fracture toughness of nano- and micro-spherical particle-filled composites [J]. Acta Mechanica, 2010, 214(1-2): 61-9. https://doi.org/10.1007/s00707-010-0314-9.

[82] ZHANG H, SCHUSTER B E, WEI Q, et al. The design of accurate micro-compression experiments [J]. Scripta Materialia, 2006, 54(2): 181-6. https://doi.org/10.1016/j.scriptamat.2005.06.043.

[83] MAYER C R, YANG L W, SINGH S S, et al. Anisotropy, size, and aspect ratio effects on micropillar compression of Al SiC nanolaminate composites [J]. Acta Materialia, 2016, 114(25-32. https://doi.org/10.1016/j.actamat.2016.05.018.

[84] FUJIMOTO F. Dynamical Theory of Electron Diffraction in Laue-Case, I. General Theory [J]. Journal of the Physical Society of Japan, 1959, 14(11): 1558-68. https://doi.org/10.1143/jpsj.14.1558.

[85] SRINIVASAN R, DE ANGELIS R J, ICE G, et al. Identification of tetragonal and cubic structures of zirconia using synchrotron x-radiation source [J]. Journal of materials research, 1991, 6(6): 1287-92. https://doi.org/10.1557/JMR.1991.1287.

[86] DELAFORCE P M, YEOMANS J A, FILKIN N C, et al. Effect of NiO on the phase stability and microstructure of yttria-stabilized zirconia [J]. Journal of the American Ceramic Society, 2007, 90(3): 918-24. https://doi.org/10.1111/j.1551-2916.2006.01464.x.

[87] FENG S W, GUO Q, LI Z, et al. Strengthening and toughening mechanisms in graphene-Al nanolaminated composite micro-pillars [J]. Acta Materialia, 2017, 125(98-108. https://doi.org/10.1016/j.actamat.2016.11.043.

[88] OTSUKA K, SHIMIZU K. Pseudoelasticity and shape memory effects in alloys [J]. International Metals Reviews, 2013, 31(1): 93-114. https://doi.org/10.1179/imtr.1986.31.1.93.

[89] DING H M, JIA H R, LI M M, et al. Study on stress distribution in microregion close to the shell of core-shell particle reinforced metal matrix composites [J]. Materials Science and Engineering a-Structural Materials Properties Microstructure and Processing, 2020, 784(139317. https://doi.org/10.1016/j.msea.2020.139317.

[90] HAQUE S, CHOY K L. Finite element modelling of the effect of a functionally graded protective coating for SiC monofilaments on Ti-based composite behaviour [J]. Materials Science and Engineering a-Structural Materials Properties Microstructure and Processing, 2000, 291(1-2): 97-109. https://doi.org/10.1016/S0921-5093(00)00980-1.

[91] AGHDAM M M, HOSSEINI S M A, MORSALI S R. Simulation of interface damage in metal matrix composites under off-axis loading using cohesive zone model [J]. Computational Materials Science, 2015, 108(42-7.

https://doi.org/10.1016/j.commatsci.2015.05.030.

[92] AGHAJANIAN M K, ROCAZELLA M A, BURKE J T, et al. The fabrication of metal matrix composites by a pressureless infiltration technique [J]. Journal of Materials Science, 1991, 26(2): 447-54. https://doi.org/10.1007/bf00576541.

APPENDIX

I. Whole Process of *in-situ* Compression

CZ-Al Pillar #1 *in-situ* Compression: ($Strain\ Rate = 5 \times 10^{-4}$)

$\boldsymbol{t = 0\ s}$ (Engineering strain=0)

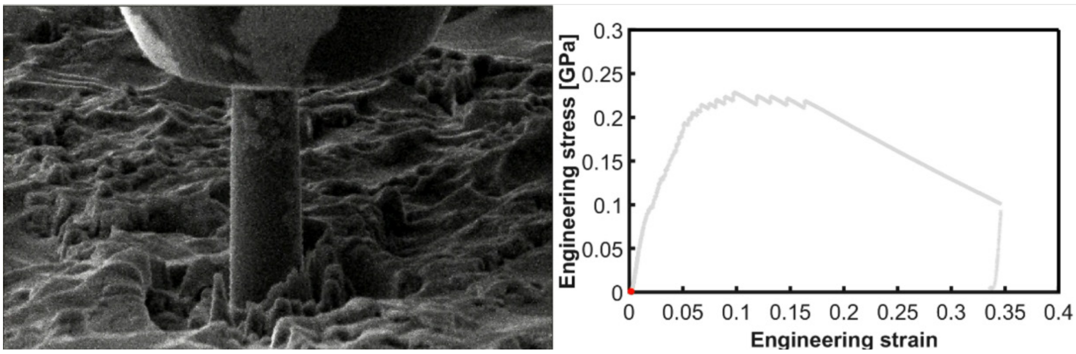

$\boldsymbol{t = 100\ s}$ (Engineering strain=0.05)

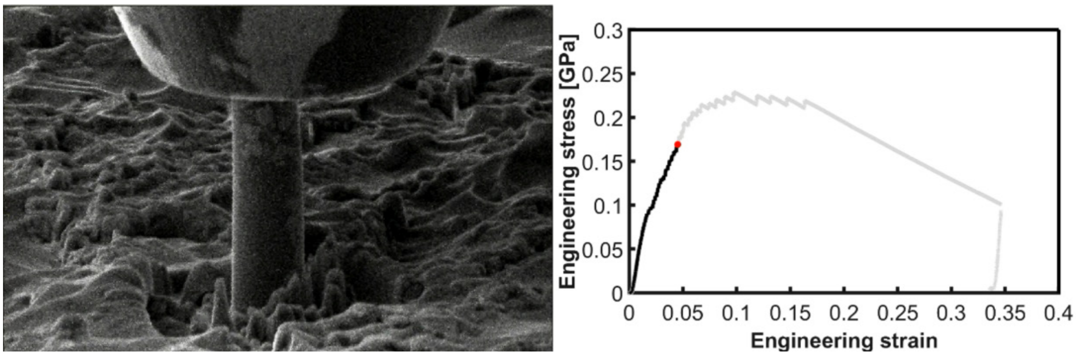

$\boldsymbol{t = 200\ s}$ (Engineering strain=0.10)

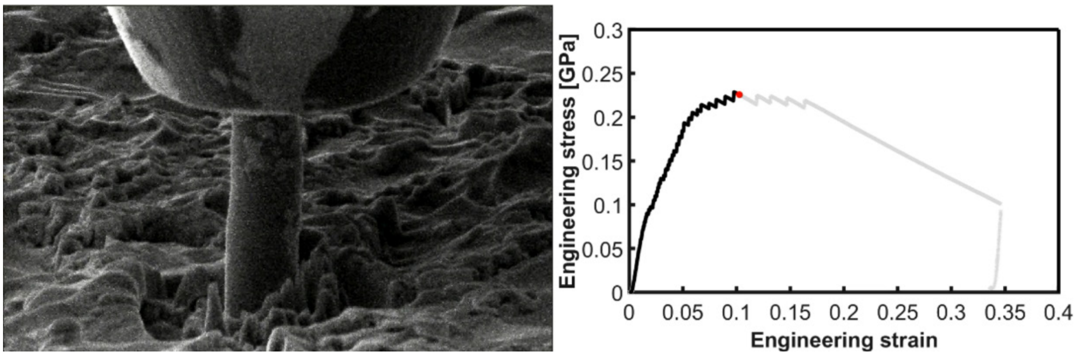

$\boldsymbol{t = 300\ s}$ (Engineering strain=0.15)

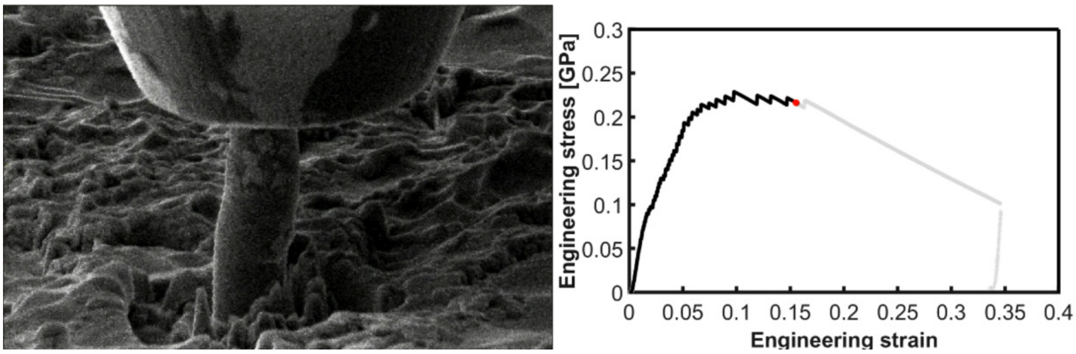

$\boldsymbol{t = 400\ s}$ (Engineering strain=0.20)

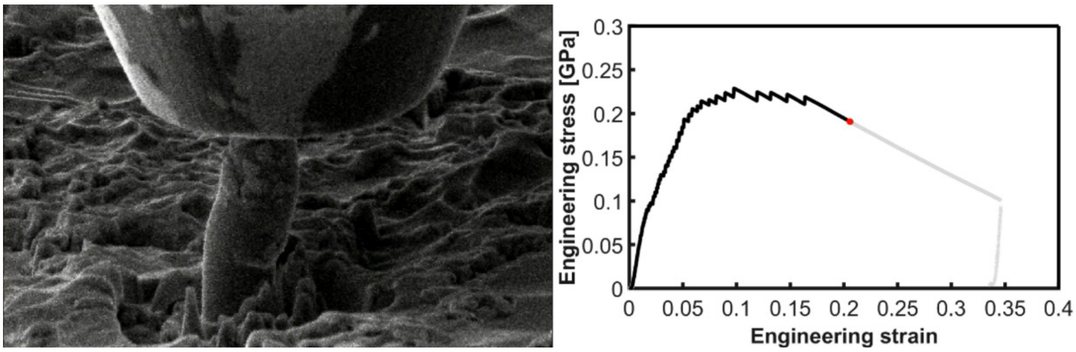

$\boldsymbol{t = 500\ s}$ (Engineering strain=0.25)

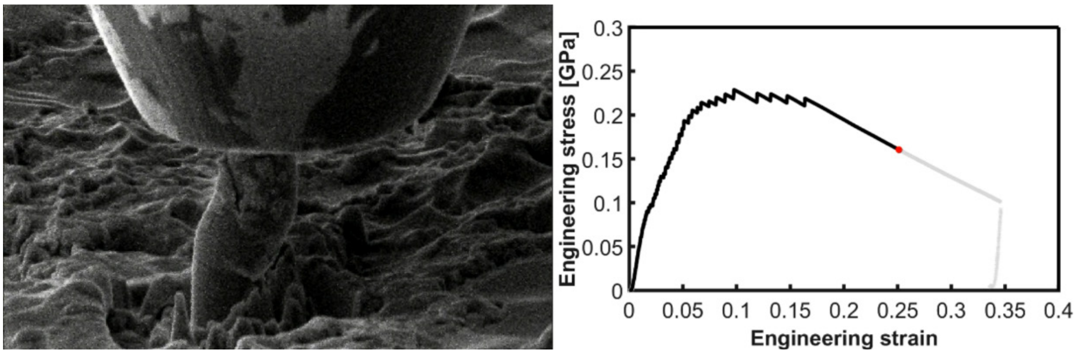

$\boldsymbol{t = 600\ s}$ (Engineering strain=0.30)

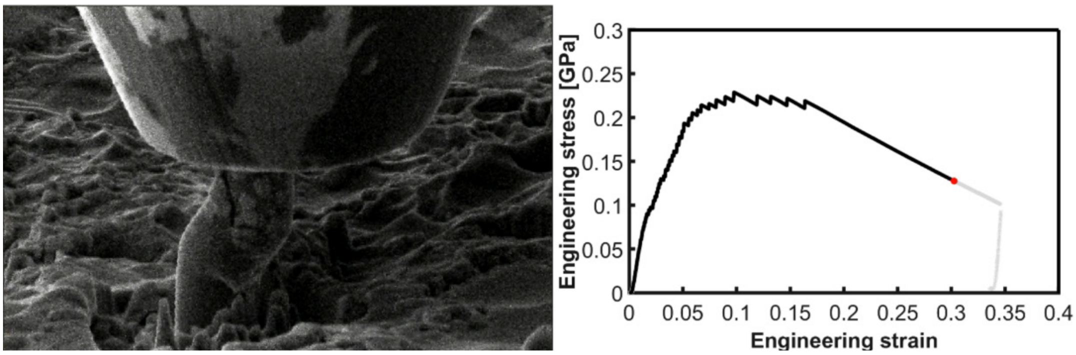

CZ-Al Pillar #2 *in-situ* Compression: $\boldsymbol{t = 0\ s}$ (Engineering strain=0)

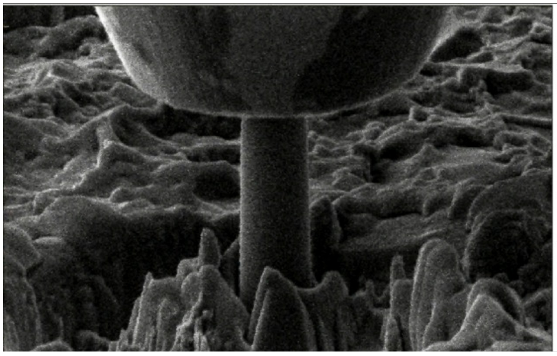

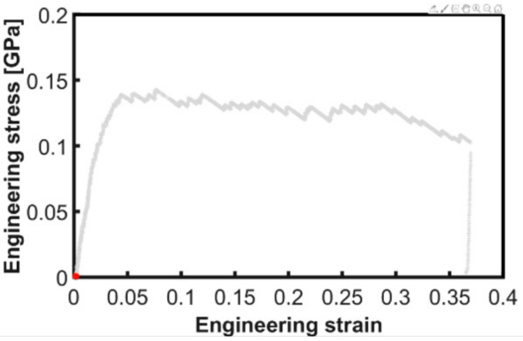

$\boldsymbol{t = 100\ s}$ (Engineering strain=0.05)

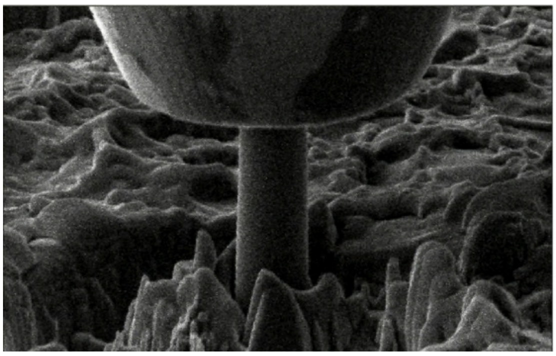

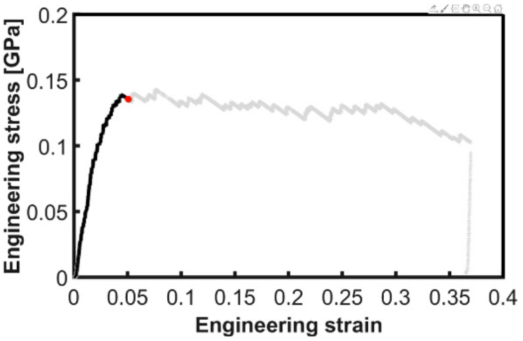

$\boldsymbol{t = 200\ s}$ (Engineering strain=0.10)

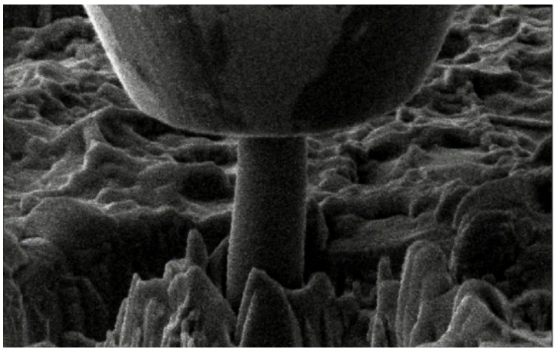

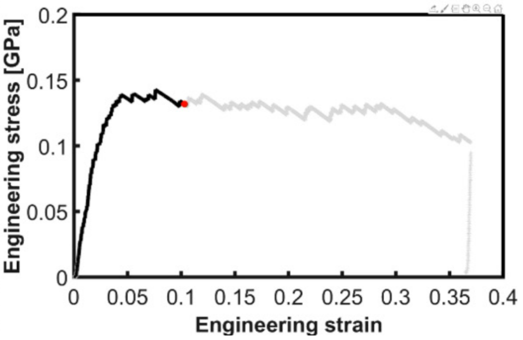

$\boldsymbol{t = 300\ s}$ (Engineering strain=0.15)

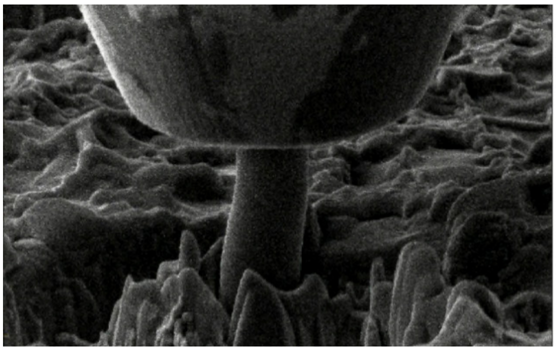

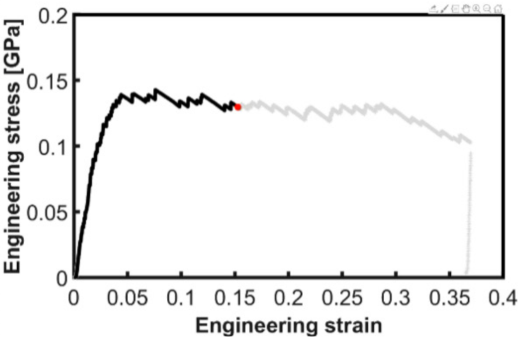

$\boldsymbol{t = 400\ s}$ (Engineering strain=0.20)

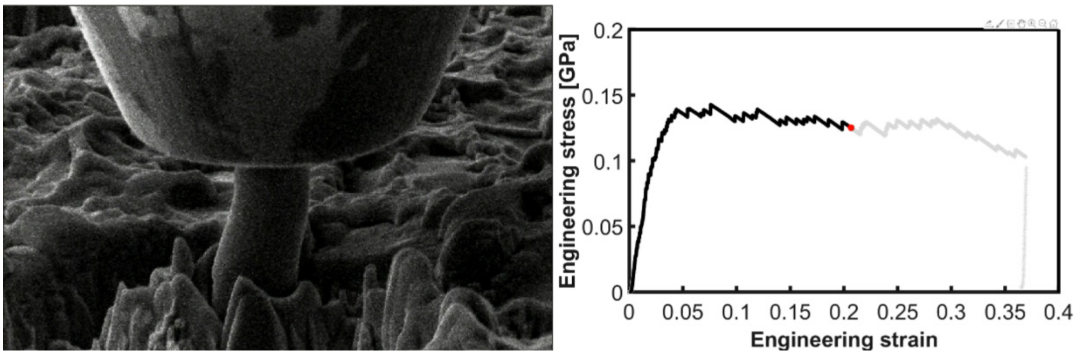

$\boldsymbol{t = 500\ s}$ (Engineering strain=0.25)

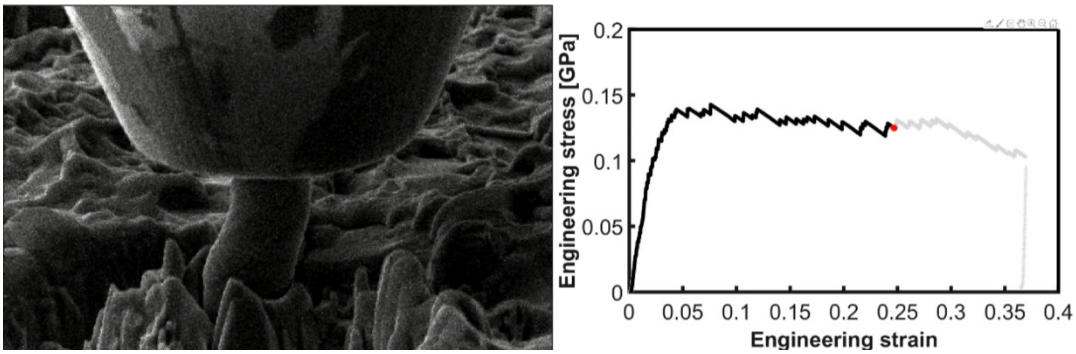

$\boldsymbol{t = 600\ s}$ (Engineering strain=0.30)

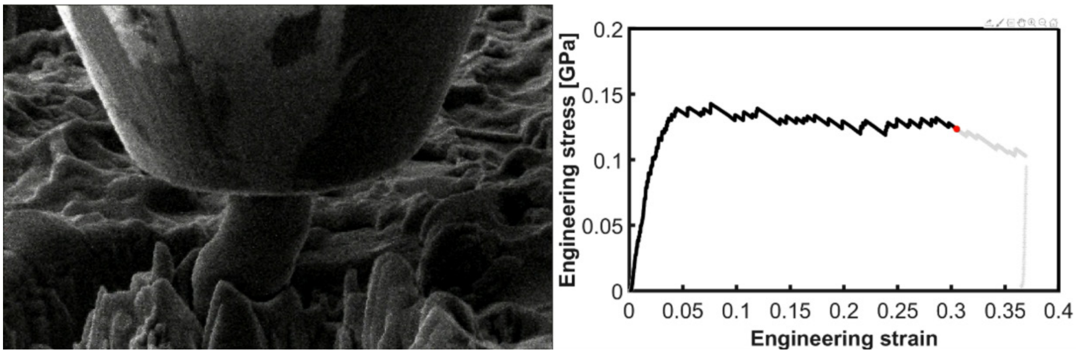

$\boldsymbol{t = 700\ s}$ (Engineering strain=0.35)

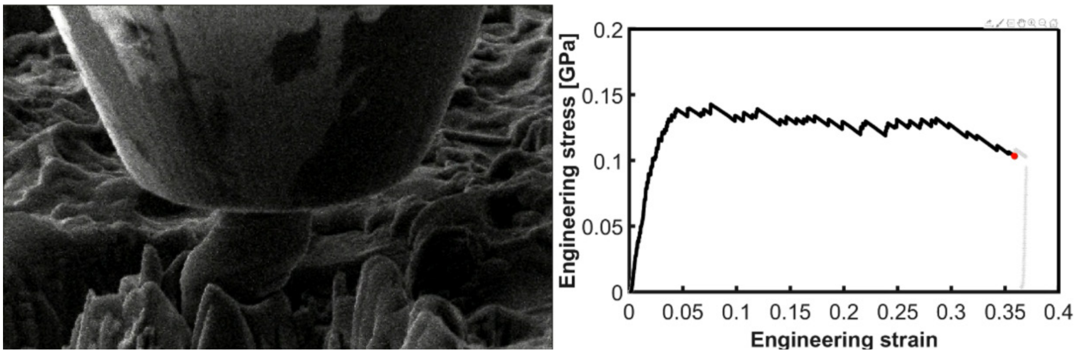

II. Achievements during the Study for Bachelor's Degree

[1]. Zada I, Zhang W, **Zheng W**, *et al*. The highly efficient photocatalytic and light harvesting property of Ag-TiO_2 with negative nano-holes structure inspired from cicada wings[J]. Scientific reports, 2017, 7(1): 1-9.

[2]. 张旺, 薛瑞阳, 朱本必, **郑王树**, 张志坚, & 张荻. 基于双螺旋二十四面体结构的 pH 敏感元件的制备方法: CN106908393A. (实审中)

[3]. **Zheng W**, Maciejewska B, Grobert N. Fabrication of Aligned Polymer Fibre via Solution Blow Spinning. (2019, To be submitted)

ACKNOWLEDGEMENT

It's my great honor to show my stintless appreciation to the people who has given me a hand and led me into a research gate. To some extent, it is also a farewell ceremony behind every period of memory.

Wang Zhang, who is my first mentor since 2017 in SJTU, has provided me with a blueprint for the whole world for scientific research, and offered me a chance to publish my first paper and apply my first patent. Two-year systematic and independent research has aroused my interests in natural inspired material. Subsequently, Prof. Jian Ye and Jing He have opened my mind in bio-medical nano structural materials at Med-X, where I learned deeply research method and several equipment. The real case that I figured out how to overcome the obstacle in the research and understand the importance of teamwork lies in 3-month summer research in University of Oxford under the guide of Prof. Nicole Grobert FRSC FYAE and Dr. Barbara M Maciejewska.

As far as the graduation design, where I have started my project in Ph. D., has been conducted with the help of Prof. Qiang Guo (SJTU) and Dr. Zehui Du (NTU). In the meantime, Yan Shi, Yu Liu, YuYang Liu, Siting Zheng, Ganting Yang has helped me a lot about the whole issues in the lab as well as the procedure to operate the equipment. Without their help, I will never fulfill such a huge work and promising result so far.

When I look back to the bitter-sweet time occasionally, four years have accompanied with four different lab experience, becoming an adventure, becoming my personal treasure, becoming a star hanging in the sky, blinking and shining forever.

It is always not too much to appreciate the people standing by, my parents and family members, Kaiyuan Lin, my girlfriend Yuxin Ye, my close friends Jiaheng Peng, Hengrui Zhang, Tianyu Shen, Linze Qian, Mengting Jin and the life itself. A long journey, from my familiar past and towards unknown future.